University of California
Santa Barbara

Mapping the Mesoscale: Revealing Local Heterogeneities with Dark-Field X-ray Microscopy

A dissertation submitted in partial satisfaction
of the requirements for the degree

Doctor of Philosophy
in
Mechanical Engineering

by

Jayden C. Plumb

Committee in charge:

Professor Samantha Daly, Co-Chair
Professor Stephen Wilson, Co-Chair
Zahir Islam, Ph.D., Argonne National Laboratory
Professor Irene Beyerlein
Professor Bolin Liao

September 2024

The Dissertation of Jayden C. Plumb is approved.

Zahir Islam

Irene Beyerlein

Bolin Liao

Stephen Wilson, Committee Co-Chair

Samantha Daly, Committee Co-Chair

August 2024

Mapping the Mesoscale:

Revealing Local Heterogeneities with Dark-Field X-ray Microscopy

by

Jayden C. Plumb

Acknowledgements

First and foremost, I would like to express my deepest gratitude to my advisors, Sam Daly and Stephen Wilson. Their guidance, support, and expertise have been invaluable throughout the six years of my graduate studies. Their belief in my potential and their guidance have been instrumental in shaping this work. I am profoundly grateful to my mentor, Zahir Islam, with whom I had the privilege of spending six months studying the experimental technique DFXM and conducting experiments at the Advanced Photon Source (APS). His mentorship and insights were crucial in advancing my research and understanding. I would also like to thank my other APS collaborators, Ishwor Poudyal, Peter Kenesei, Hemant Sharma, Zhan Zhang, Jessica McChesney, David Gagliano and Ulrich Welp. Their contributions and collaboration were essential to my learning and the success of my experiments. Special thanks to the members of our weekly "DFXM Therapy" sessions, Elliot Kisiel, Fellipe Carneiro, and Kaan Yay. Our discussions and problem-solving sessions were both enlightening and enjoyable. My heartfelt appreciation goes to Linus Kautszch, Steven Gomez, Neal Brodnik, Andrew Christison, Michelle Harr, and the rest of the Wilson and Daly lab groups. Your support and camaraderie made my research journey enriching and fulfilling.

The work presented herein was made possible by the National Science Foundation's (NSF) Materials Research Science and Engineering Center (MRSEC) at UC Santa Barbara (NSF DMR 1720256) through IRG-1. I acknowledge the use of shared facilities of the NSF MRSEC at UC Santa Barbara (Award No. DMR-1720256) and the Center for Scientific Computing, supported by the California Nano Systems Institute, the NSF MRSEC (Award No. DMR-1720256) and NSF (Award No. CNS-1725797). The experimental work detailed in this thesis used resources of the Advanced Photon Source, a U.S. Department of Energy (DOE) Office of Science User Facility at Argonne National Labo-

ratory and was additionally supported by the U.S. DOE Office of Science-Basic Energy Sciences Graduate Student Research (SCGSR) program, under Contract No. DE-AC02-06CH11357.

I owe a tremendous debt of gratitude to my fiancée, Shelby Matsumura, for her unwavering love, support, and encouragement throughout my studies. Her belief in me, especially during times when I struggled to believe in myself, has been a source of strength and motivation. I also extend my thanks to the rest of the Matsumura family for their kindness and support. To my family: my Mother Sonja, Father Jan, older brother Tyler and younger brother Bronson—thank you for your endless love and encouragement. Your support has been the foundation upon which I have built my academic journey. I am also immensely grateful to my best friend, Maxim Nebeker, for his steadfast friendship and support through my undergraduate and graduate studies. Finally, I want to thank my kickboxing coach, Joe Ramirez, and the rest of the Paragon Team. Training with you has not only been incredibly fun but has also built my self-confidence and resilience, both in fighting and in life.

Thank you all for your support, encouragement, and belief in me. This thesis would not have been possible without each and every one of you.

Curriculum Vitæ

Jayden C. Plumb

Education

2024	Ph.D. in Mechanical Engineering (Expected), University of California, Santa Barbara, CA.
2018	B.S. in Mechanical Engineering, University of Utah, Salt Lake City, UT.

Fellowships

Jun-Dec 2021	DOE Office of Science Graduate Student Research (SCGSR) Program
DOE Lab:	Argonne National Laboratory
SC Programs:	Advanced Scientific Computing Research, Basic Energy Sciences

Publications

[1] **Plumb, J.**, Capa Salinas, A., Kisiel, E., Carneiro, F., Pokharel, G., Islam, Z., Daly, S., & Wilson, S. D. (2024). Phase-separated charge order and twinning across length scales in CsV_3Sb_5. *Physical Review Materials*, *8*, 093601.

[2] Gomez Alvarado, S. J., Zoghlin, E., Jackson, A., Kautzsch, L., **Plumb, J.**, Aling, M., Capa Salinas, A. N., Pokharel, G., Pang, Y., Gomez, R. M., Daly, S., & Wilson, S. D. (2024). Advances in high-pressure laser floating zone growth: The Laser Optical Kristallmacher II (LOKII). *Review of Scientific Instruments*, *95*(3).

[3] **Plumb, J.**, Poudyal, I., Dally, R. L., Daly, S., Wilson, S. D., & Islam, Z. (2023). Dark field X-ray microscopy below liquid-helium temperature: The case of $NaMnO_2$. *Materials Characterization*, *204*, 113174.

[4] Kautzsch, L., Ortiz, B. R., Mallayya, K., **Plumb, J.**, Pokharel, G., Ruff, J. P. C., Islam, Z., Kim, E., Seshadri, R., & Wilson, S. D. (2023). Structural evolution of the kagome superconductors AV_3Sb_5 (A= K, Rb, and Cs) through charge density wave order. *Physical Review Materials*, *7*(2), 024806.

[5] Johnson, Q. C., Kenesei, P., Petruzza, S., **Plumb, J.**, Sharma, H., Park, J. S., Marsden, E., Matheson, K., Czabaj, M. W., & Spear, A. D. (2023). Mapping 3D grain and precipitate structure during in situ mechanical testing of open-cell metal foam using

micro-computed tomography and high-energy X-ray diffraction microscopy. *Materials Characterization*, *195*, 112477.

[6] **Plumb, J. C.**, Lind, J. F., Tucker, J. C., Kelley, R., & Spear, A. D. (2018). Three-dimensional grain mapping of open-cell metallic foam by integrating synthetic data with experimental data from high-energy X-ray diffraction microscopy. *Materials Characterization*, *144*, 448-460.

Abstract

Mapping the Mesoscale:

Revealing Local Heterogeneities with Dark-Field X-ray Microscopy

by

Jayden C. Plumb

This thesis investigates the role of local inhomogeneities and mesoscale features to understand material behavior not possible to realize with measurements on the average. It leverages a novel Dark Field X-ray Microscopy (DFXM) experimental technique to image mesoscale structures in a bulk-sensitive manner with hard X-rays at synchrotron facilities. DFXM utilizes an X-ray objective to magnify an individual diffraction peak and capture spatially resolved intensity distributions that highlight local variations from the nanometer to tens of micron length scales. However, challenges remain in the application of this technique to examine low-temperature phenomena and subtle periodic structures in quantum materials, which exhibit complex phases at cryogenic temperatures.

One such quantum material is $NaMnO_2$, which demonstrates frustrated antiferromagnetism (AFM) at low temperatures and a high reversible capacity suitable for use in rechargeable battery applications. Its magnetic and electronic properties are further complicated by a series of crystal defects (including twinning, stacking faults, polymorphism and Mn_3O_4 intergrowths), whose size and spatial distribution remain unresolved. Furthermore, magneto-elastic coupling has been hypothesized to result in the formation of nanoscale triclinic domains below the AFM transition at 45 K, but this effect has yet to be experimentally validated. DFXM is well suited to characterize the heterogeneous structure of $NaMnO_2$, provided that the challenges in performing the experiment at low temperature are overcome. DFXM studies performed on $NaMnO_2$ reveal linear micro-

structures that span hundreds and tens of μm in the longitudinal and transverse directions, respectively. Increased DFXM magnification exposes the linear domains are further broken up into a myriad of nanoscale structures, which are likely the root of enigmatic experimental data. A first-of-its-kind DFXM experiment performed below liquid-helium temperature displays significant microscale intensity variations through the AFM transition. Although the formation of triclinic domains were not directly observed, DFXM images reveal that temperature-dependent local actors are responsible for mimicking a bulk structural distortion in X-ray measurements of the average structure.

Another non-trivial electronic material is the recently discovered superconducting kagome, CsV_3Sb_5, which hosts a charge-density-wave (CDW) instability below 94 K. Three-dimensional in nature, the CDW phase in CsV_3Sb_5 is accompanied by in-plane structural distortions that form Star of David (SoD) or Tri-Hexagonal (TrH) patterns, but inconsistencies in the out-of-plane component have left the stacking order ambiguous. Peak splitting in conventional X-ray diffraction data indicates the formation of $2 \times 2 \times 2$ and $2 \times 2 \times 4$ supercell structures below T_{CDW}. The primary question addressed in this thesis is whether these two CDW types compete during formation, resulting in phase separation, or coexist within the same crystallographic domain, comprised of two Fourier components. CsV_3Sb_5 is further complicated by a reduction from six-fold hexagonal symmetry to two-fold orthorhombic symmetry following the CDW transition. Elucidating the origin of the CDW instability is a critical step toward understanding the novel phenomena in this complex material. Real-space DFXM images of CsV_3Sb_5, collected across multiple length scales, provide evidence for a rich microstructure at low temperatures. DFXM images of the $\left(\frac{1}{2}, \frac{1}{2}, \frac{1}{2}\right)$ and $\left(\frac{1}{2}, \frac{1}{2}, \frac{1}{4}\right)$ CDW peaks, collected over hundreds of μm, are presented for evaluation. Comparison of each CDW peak reveals a significant spatial separation in three-dimensions and supports a theory of two distinct crystal domains being responsible for the split CDW signal.

The experiments detailed in this thesis further demonstrate two novel implementations of the DFXM methodology, including in situ cryogenic temperature variation and full-field imaging of a bulk charge-density wave using hard X-rays and direct detection. Extending DFXM to low temperatures through the use of a low-vibration cryostat creates an avenue for experimental investigations of other complex physical phenomena. Additionally, DFXM imaging of charge-order Bragg peaks demonstrates the potential of this methodology to be extended to other weakly scattered structures (*e.g.* magnetic, elemental, *etc.*).

Contents

Chapter 1

Introduction and Material Background

1.1 Motivations

The principle purpose of this thesis is to answer the fundamental question: **why** do materials behave the way that they do. Understanding how the basic building blocks of matter interact with one another to give characteristic materials their appearance, response to stimuli, and energetic potential, is key to answering this question and a pivotal step towards understanding the world around us. In this way, the study of materials and their structures is an invaluable field of scientific research that touches all other scientific domains. Fundamentally, the research presented herein was performed in an attempt to answer this question, with a specific focus on solid materials that exhibit complex electronic and/or magnetic phenomena.

The study of electronic and magnetic crystalline solids and the foundational physics that drive their behavior often follows a characterization cycle that consists of 5 major steps. First is crystal synthesis, whereby a specific material compound is grown

or fabricated using highly specific thermodynamic processes. Following synthesis is the characterization of the material's atomic structure and subsequent determination of the material's relevant macroscale properties. Once the atomic structure is known and the material's bulk response has been recorded, the next step in the cycle is connecting these information sets to define the material's structure-property relationships. Understanding these relationships enables the final step in the cycle, which applies that knowledge to explore and discover novel materials or to design and optimize the material for specific applications. In either scenario, the end of the cycle leads back to the first step, which is to synthesize the next material iteration. While each step in this cycle bears significance in creating a complete picture of material behavior, the work presented here focuses on the structural characterization step.

Before structural characterization takes place, the crystal needs to exist, *i.e.*, be synthesized. The synthesis step includes the creation of so-called polycrystal and single-crystal material samples. While a given material compound generally has a singular atomic-cell configuration, called its unit-cell, that configuration is not confined to a single orientation in three-dimensional space. As a material is formed, groups of unit-cells align with each other along specific crystallographic orientations or directions, forming grains or regions of orientation coherence. Thus, a polycrystalline sample is one that is made up of many grains in contrast to a single-crystal sample. This thesis focuses on single-crystal samples to simplify the investigation of complex structures by eliminating the contributions to heterogeneity that arise from varied grain structures and grain boundaries.

Once a material sample is successfully fabricated, the nature of its basic atomic structure can be investigated and characterized. This characterization is typically performed at two relevant length scales, the atomic-scale and the macroscale. At the small end of the spectrum, materials are studied across the atomic-scale ($\sim nm$) to define the princi-

ple blocks (*i.e.*, atoms, unit-cells, dislocations, *etc.*) with which a material is built. These efforts seek to answer the fundamental question: of **what** is the material made. Once identified, these basic components are multiplied and combined to represent the material at a much larger scale - the macroscale. Here, macroscale refers to the length scale at which a single part or component of a device exists ($\sim mm$). Constructing a macroscale model of a material's structure is vital to connect that structure to the material's bulk (stemming from the nominal volume) properties and behavior. For many materials, the leap from atomic to macroscale structures is readily explained by a random assembly of atomic building blocks to create an average structure that represents the bulk material. When the average structure serves as a sufficient characterization, it can be related to the observed material properties to answer the question: **how** a material obtains its characteristic qualities. Further study of a material's structure-property relationships are performed and a step is taken towards answering the first question presented: **why**.

One might then ask: what happens when the average crystal structure is not enough to explain the observed material behavior. Connecting length scales becomes especially difficult when the material's crystal structure is highly complex. Structural complexity can lead to novel ground states, but often with the consequence of multiple coexisting phases and defect structures. As the number of potential building blocks needed to craft a material's structure increases, so too does the importance of investigating the meso—or intermediate—length scale ($\sim \mu m$). In this way, characterization of a material's mesoscale structure is akin to answering the question: **where** are the blocks placed when building the bulk structure. The pursuit of my graduate research is centered around answering this question by using synchrotron-source-diffraction experiments to investigate local heterogeneities in complex magnetic and electronic crystals. By selecting two material candidates, $NaMnO_2$ and CsV_3Sb_5, and experimentally characterizing their mesoscale structures and identifying regions **where** local deviations from the average

structure occur (namely, using Dark-Field X-ray Microscopy or DFXM), this research aims to contribute to the understanding of **why** these materials behave the way they do.

1.2 Functional Complex Oxide: $NaMnO_2$

The first material of interest in this work is $NaMnO_2$, a complex oxide of the form ABO_2, where A is an alkali metal and B is a transition metal. These oxides are popular compounds for cathode applications and particularly for their applications in energy storage and transfer technologies. Furthermore, the layered nature of $NaMnO_2$ facilitates reversible ionic diffusion, making it especially relevant to rechargeable battery applications. A competitive candidate amongst layered-complex oxides, $NaMnO_2$ additionally leverages the low cost of earth-abundant sodium, in contrast to the more expensive lithium-based alternatives. In addition to its favorable electronic properties, $NaMnO_2$'s triangular arrangement of magnetic Mn^{3+} ions are subject to geometric frustration. In this context, geometric frustration is described as the disruption of the regular crystal lattice due to competing magnetic interactions (*i.e.*, antiparallel correlations). This magnetic frustration is relieved through distortion of the crystal lattice, which results in the formation of quasi-one-dimensional antiferromagnetic spin-chains [1]. This magnetic state eventually evolves into three-dimensional long-range order below 45 K [2]. Frustrated magnetoelectric materials often host novel electronic, magnetic, or structural phases that lead to complex physical phenomena, such as spin liquid ground states [3] and cycloidal order [4, 5]. These properties make $NaMnO_2$ an interesting candidate for applications-driven studies and explorations of fundamental physics.

The fundamental level of characterization for $NaMnO_2$ starts by defining the basic structures inherent to the material. The geometric frustration inherent in $NaMnO_2$'s

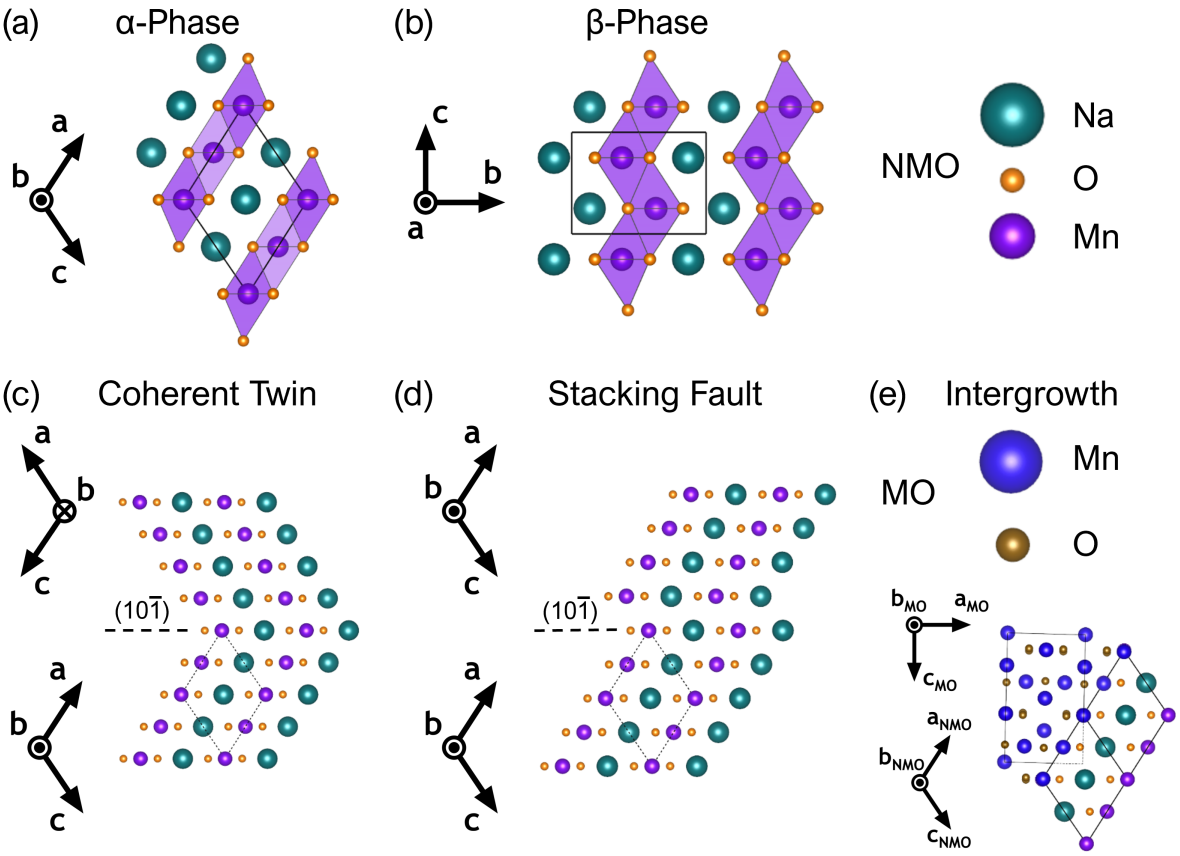

Figure 1.1: Crystal structure of the (a) α-phase and (b) β-phase of $NaMnO_2$. Examples of crystal structure defects in the α-phase, including a (c) coherent twin, (d) stacking fault, and (e) Mn_3O_4 intergrowth. The various unit cells are outlined using solid or dashed black lines and the real-space orientations are denoted to the left of each lattice structure.

triangular structure of the Mn^{3+} ions, couples with a low stacking-fault energy to result in a polymorphic crystal structure that hosts a series of defects. The first polymorph, or α-phase, of $NaMnO_2$ is composed of Na layers, separated by layers of MnO_6 octahedra (see Figure 1.1(a)). The α-phase unit-cell can be described as a distorted α-$NaFeO_2$-type structure that is monoclinic (C2/m) at room temperature [1]. The second polymorph, or β-phase, is characterized by the formation of successive stacking faults (every other unit cell) that interrupt the pristine layers of the α-phase. The periodic faults form a zig-zag pattern between the anion and cation layers and result in a structural transition

from a monoclinic to an orthorhombic unit-cell (see Figure 1.1(b)). Density Functional Theory (DFT) calculations predict the formation energies of the two phases are within 5 meV of each other [6], indicating that any sample of $NaMnO_2$ is likely to have some proportion of each polymorph within it. Additionally, a third polymorph that consists of quasi-periodic stacking fault structures has also been characterized [1], and represents an intermediate phase between the limiting α and β phases. The low energy barrier between polymorphs suggests that $NaMnO_2$'s energy landscape is sensitive to local minima and hints at its potential for exotic ground states.

The principal mechanism for $NaMnO_2$'s defect structure is the formation of coherent twins within the α-phase. Twinning is a crystal phenomena that is described by the formation of two crystallographic domains that are symmetrically constrained to one another with respect to their orientation. In the case of α-$NaMnO_2$, planar twins are formed by mirroring the crystal lattice across $(10\bar{1})$ type planes. Stacking faults in the α-phase can be described by the appearance of two successive twin planes and the population of the two defects are expected to be proportional to one another. In addition to the previously described defects, Dally *et al.* [2] observed the formation of a tetragonal Mn_3O_4 intergrowth phase that exhibits a weak ferromagnetism at low temperatures, further impacting the behavior of $NaMnO_2$. The complex array of defects present in $NaMnO_2$ (shown in Figure 1.1(c-e)) present a challenge in characterizing the crystal structure completely.

The fundamental magnetic structure of $NaMnO_2$ is driven by an antiferromagnetic (AFM) coupling of the Mn^{3+} ions. The AFM coupling of the lattice drives electron-exchange that favors anti-parallel magnetic dipoles between ionic neighbors. Individual interactions or couplings are denoted J_n and given in temperature units (K), representing the strength of the exchange as thermal energy. A triangular lattice of uneven magnetic interactions (*i.e.*, $J_1 \neq J_2$) creates a geometric frustration due to polar metastability in

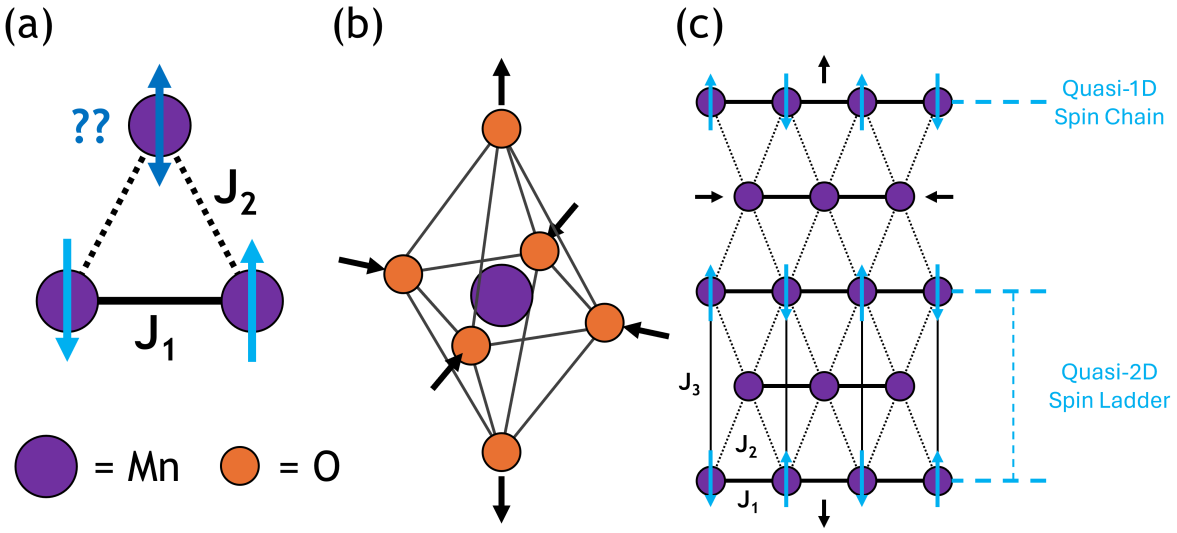

Figure 1.2: Schematic diagram of magnetic concepts relevant to $NaMnO_2$.(a) Geometric frustration in a triangular lattice of magnetic atoms, Mn^{3+} ions for $NaMnO_2$, that are antiferromagnetically correlated. (b) Jahn-Teller (JT) distortion that involves the lengthening of the long-axis and shortening of the equatorial axes of the MnO_6 octahedra. The JT diagram is a visual simplification of the complex distortion in $NaMnO_2$, that does not display any canting of the Mn-O bonds. (c) Projection of $NaMnO_2$'s triangular lattice in the *ab* plane that demonstrates the formation of the quasi-1D spin chains and quasi-2D spin ladders observed in $NaMnO_2$. Magnetic exchange couplings (J_1, J_2, and J_3) are labeled and weighted to represent their relative strengths and blue arrows designate the magnetic polarity of antiferromagnetism (AFM) correlated lattice sites in (a) and (c). Dimensions not drawn to scale.

the third unknown state (see Figure1.2(a)). In $NaMnO_2$, this frustration is lifted via a Jahn-Teller (JT) distortion of the MnO_6 octahedra. The JT distortion is known as a breathing mode distortion, described by an extension of one long-axis and contraction of two short-axes of the octahedra, or vice versa (see Figure 1.2(b)). The shift in atomic positions shortens the Mn-Mn distance responsible for J_1 to 2.86 Å and extends the Mn-Mn distance corresponding to J_2 to 3.17 Å. The difference in atomic distances result in $J_1 = 73$ K and $J_2 = 29$ K, determined experimentally in Refs. [7, 8].

The overwhelming strength of the J_1 interaction leads to the formation of quasi-1D spin chains in the α-phase of polycrystalline $NaMnO_2$. As the α-phase is cooled

below 200 K, quasi-2D AFM correlations are formed, while further cooling below the Néel Temperature, $T_N = 45$ K, establishes long-range 3D AFM order [7–10]. On the other hand, the displacement of every other MnO_6 octahedra in β-$NaMnO_2$ activates a third coupling, J_3, that results from a near-180° (166.8°) superexchange via Mn-O-Mn pathways. Thus, the magnetic ground state of $NaMnO_2$'s β-phase is instead characterized by quasi-2D AFM order that consists of two strong couplings, $J_1 = 70$ K and $J_3 = 57$ K, and one weak coupling, $J_2 = 13$ K [1]. The intermediate faulted regions, that exist between the α and β phase, unsurprisingly demonstrate a magnetic structure that resembles parts of each parent phase. This mixed phase forms magnetic "spin-ladders" along stacking faults, characterized by correlated spin-chain doublets (see Figure 1.2(c)).

In 2017, Dally *et al.* [11] demonstrated a floating zone synthesis methodology for growing large ($\sim mm$) single-crystals of α-$NaMnO_2$, which enabled more in-depth studies of its complex magnetic structure. Using solid-state nuclear magnetic resonance (ssNMR), growth parameters were refined to reduce the presence of faulted regions to $\approx 4\%$ and the proportion of β-phase regions to near-negligible ($< 1\%$) [11]. Subsequent neutron scattering experiments performed on a single-crystal of α-$NaMnO_2$ reveal a refined thermal evolution, composed of three major transition temperatures [2]. Paramagnetic at room temperature, the first magnetic transition in α-$NaMnO_2$ occurs below 200 K to form quasi-1D spin correlations. The next transition happens at 45 K where AFM order is established, but this ground state demonstrates a complex coexistence of magnetic domains that are incommensurate (short-range) and commensurate (long-range) within the crystal lattice. The final magnetic transition occurs at 22 K, where the full commensurate transition is completed. Notably, the commensurate transition does not achieve a truly long-range order due to structural heterogeneities [12].

Using the fundamental building blocks that have been defined, a picture of $NaMnO_2$'s average structure can be built and compared to bulk observations, specifically from ex-

perimental scattering techniques. In particular, Zorko *et al.* [13] performed synchrotron X-ray diffraction (XRD) measurements on α-$NaMnO_2$ to explore the connection of its magnetic transitions to the structural behavior of its atomic lattice. Earlier neutron scattering work by Giot *et al.* [9] indicated a bulk structural transition from a monoclinic to a lower-symmetry triclinic structure, occurs in the α-phase in conjunction with the AFM transition at 45 K. The higher resolution inherent to the synchrotron X-rays used by Zorko *et al.* [13] revealed an asymmetric peak broadening below the Néel temperature that was previously unobserved. While broadening in X-ray diffraction data is indicative of a structural change to the atomic lattice, the nature of this change is subtle and the lack of resolution has left the specifics of this magneto-structural coupling ambiguous. The structural effect has since been hypothesized to stem from either local lattice strains within the the nominal monoclinic phase, possibly driven by local structural heterogeneity, or a coexistence of local triclinic nano-crystalline domains that are distributed randomly throughout the monoclinic matrix. Discrimination between these two possible crystal structures has so far been difficult, as it involves a non-trivial connecting of the average crystal lattice structure (reciprocal-space scattering) to local nano-scale heterogeneities (real-space imaging). Experimental validation and visualization of the mechanisms that drive the magneto-elastic behavior, is an important step in understanding the structure-property relationships inherent to $NaMnO_2$.

The hierarchical nature of atomic structures implies that any potential nanoscale crystal domains, that form at low temperature, likely stem from structural heterogeneities that exist at room temperature in the as-grown state of the crystal. Room temperature characterization of the spatial distribution of defects and atomic domains then becomes a vital first step towards understanding the low temperature behavior, while also providing useful insights into the impact of heterogeneity of the material's macroscale electronic properties. Using an averaged structural model, many of the complex structures ex-

hibited by $NaMnO_2$ have been linked to its functional properties as a battery material. Abakumov *et al.* [1] postulates a variance in the electrochemical potential of $NaMnO_2$ based on the population of planar defects within the sample. The argument is made that the redox potential of $NaMnO_2$ can be tuned between that of the α-phase, 2.26 V, and the β-phase, 2.63 V, by controlling the density of planar defects created during crystal synthesis.

Similarly, a variance between the reversible capacity of the α- and β-phases has been observed. Experimentally, after 20 charge/discharge cycles, the reversible capacity of α-$NaMnO_2$ is $\approx$130 mAh/g [14], while the β-phase maintains a higher practical reversible capacity of 170 mAh/g [15]. As the concentration of planar defects increases, so does modulation between the polymorphic variants, demonstrating a significant impact on $NaMnO_2$'s electronic properties due to structural heterogeneities.

Additionally, defect structures in $NaMnO_2$ have been linked to the degradation of reversible capacity after electrochemical cycling of the α structure. Chen *et al.* [16] found that twin boundaries formed during material synthesis were hot spots for crack nucleation. Repeated charge/discharge cycles activated these hot spots, causing crack growth and eventually fragmentation that led to an irreversible degradation of $NaMnO_2$'s capacity. During discharge, Na deintercalation occurs quickest in the α-phase, followed by the β-phase, and slowest along twin boundaries [6]. This phenomena occurs due to twin-assisted Na diffusion, which creates local volumetric heterogeneities, especially along planar boundaries [16]. Xu *et al.* [17] found evidence of this structure-property relationship in a related sodium-based oxide, $NaNi_{0.4}Mn_{0.4}Co_{0.2}O_2$, cycled at high voltages ($\geq$ 3.5 V). The volumetric differences between twinned crystallites, build internal strains that result in crack propagation over multiple cycles. Voltage decay of this kind is a bulk phenomena with a high probability of depending on defect structures and local heterogeneities, highlighting the importance of understanding relevant mesoscale structures in

α-$NaMnO_2$. The connection between planar defects and macroscale electronic properties further motivates the characterization of the spatial distribution of phases and defects in $NaMnO_2$.

1.3 Superconducting Kagome: CsV_3Sb_5

The next material of interest belongs to a class of superconducting kagome materials of the form AV_3Sb_5, where A is substituted for an alkali metal (K, Rb, Cs) [18]. Discovered by Ortiz *et al.* [18] in 2019, this family of kagomes is characterized by a two-layer structure that consists of layers of quasi-2D planes of corner-sharing triangular networks of vanadium ions coordinated with graphite-like layers of antimony, separated by layers of 2D alkali metal planes (see Figure 1.3(a, b)). All three compounds in the material family host electronic structures characterized by a charge-density-wave (CDW) instability at low temperatures. CDWs are periodic modulations of electron density that commonly arise from Fermi surface nesting or strong electron-electron correlations. Furthermore, materials with electron-phonon coupling host CDWs that coincide with structural distortions of the host lattice. CDWs can significantly influence the electronic properties of their parent materials and lead to several unconventional phenomena within the AV_3Sb_5 family, including a giant anomalous Hall effect [19, 20], various hints of staged order [21–24], broken time-reversal symmetry [25–29], and unconventional superconductivity [30–32]. The most complicated evolution of electronic states within the CDW phase is reported to occur within the A=Cs member, CsV_3Sb_5, which also possesses the most complex parent CDW state [24].

Experimental investigations of this complex-electronic state revealed that KV_3Sb_5 and RbV_3Sb_5 exhibit a common CDW-coupled lattice structure. Below the CDW ordering temperature, their crystal structures are characterized by a $3\mathbf{q}$-type distortion of the

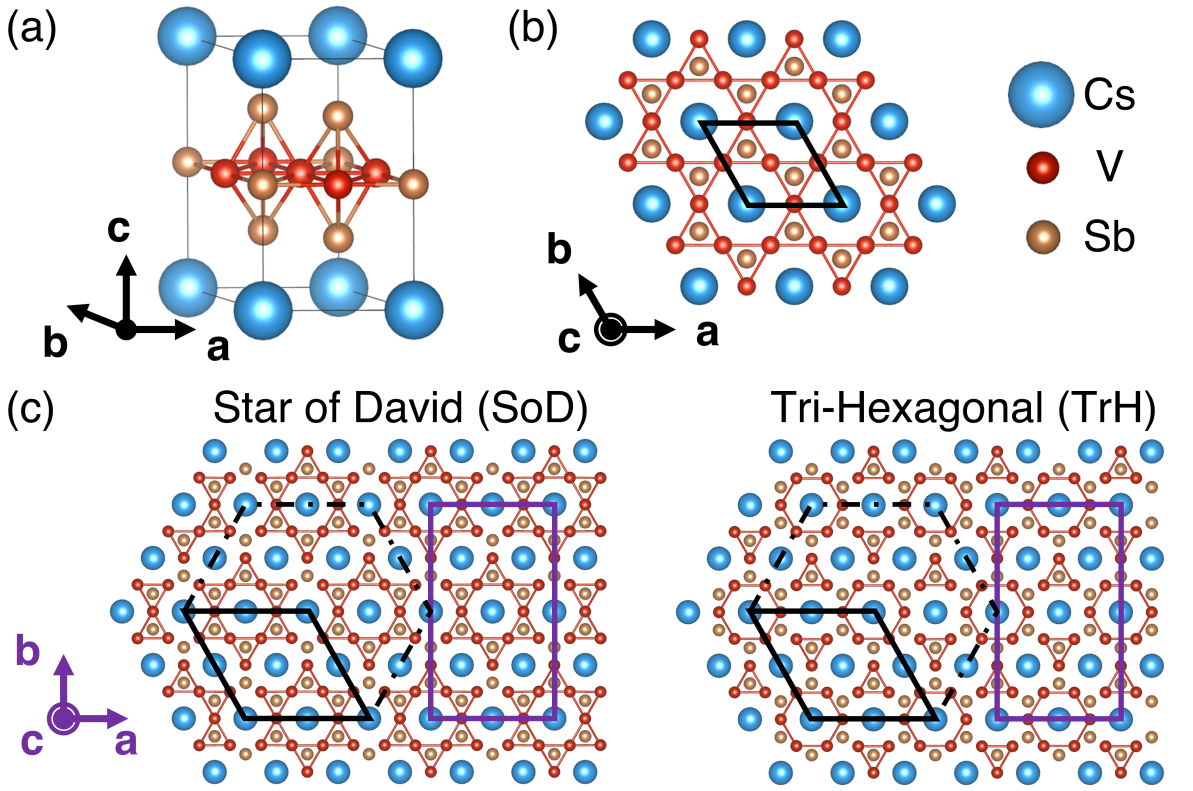

Figure 1.3: (a) View of the undistorted unit-cell of CsV_3Sb_5 at room temperature. (b) Crystal structure projection of the *ab* plane, with V-V bonds drawn to illustrate the kagome network of vanadium atoms. (c) Crystal structure of the two distortion modes, Star of David (SoD) and its inverse Tri-Hexagonal (TrH), which occur below 94 K [34]. Black lines indicate the nominal hexagonal structure of each state and purple lines indicate the orthorhombic structure formed below T_{CDW}.

kagome planes into Tri-Hexagonal (TrH) layers that stagger by half of a unit cell when stacked along the interplanar direction, resulting in a $2 \times 2 \times 2$ supercell [33, 34]. In contrast, CsV_3Sb_5, in its average structure, exhibits signs of both TrH and its inverse, Star of David (SoD)-type breathing modes within its kagome network [34–36]. Notably, the planar distortions are almost completely described by a radial shifting of the V-V bonds, confined to the *ab* plane. The stacking of these distortions along the *c*-axis creates an additional larger $2 \times 2 \times 4$ supercell in CsV_3Sb_5.

While both angle-resolved photoemission and X-ray diffraction studies report the presence of both SoD and TrH distortions in CsV_3Sb_5 [34–36], X-ray scattering reports

differ on the presence and thermal evolution of the c-axis modulation of the CDW state. Initial reports included observations of either a $2 \times 2 \times 2$ cell [37] or a larger $2 \times 2 \times 4$ superlattice [38]. Studies of the thermal evolution of CDW order later showed that both states manifest in the same crystal with either the $2 \times 2 \times 4$ state [39] or the $2 \times 2 \times 2$ state [40] stabilized via thermal quenching. This complexity and variance between samples and experiments suggests a shallow energy landscape with nearly degenerate patterns of CDW ordering [41].

A more recent investigation by Kautzsch *et al.* [34] reported the presence of metastability and a staging of multiple patterns of CDW ordering in CsV_3Sb_5 upon cooling below the transition temperature, $T_{\mathrm{CDW}} = 94$ K. Ordering along three different wave vectors, corresponding to three possible supercell structures, was observed with differing onset temperatures: (i) a $2 \times 2 \times 1$ structure forming just below the transition temperature, (ii) a $2 \times 2 \times 2$ structure forming below 90 K, (iii) and a $2 \times 2 \times 4$ structure that forms below 85 K (See Figure 1.4). Interestingly, the $2 \times 2 \times 1$ structure diminishes at the onset of the $2 \times 2 \times 4$ structure's nucleation, suggesting a competition between stacking orders with $1c$ and $4c$ components. However, the role of the $2 \times 2 \times 2$ structure in this exchange remains unclear. Diffraction signals corresponding to the $2 \times 2 \times 2$ and $2 \times 2 \times 4$ structures persist down to the superconducting temperature, $T_{\mathrm{c}} = 2.5$ K. Whether the diffraction pattern is the result of two distinct crystallographic domains or a single crystal domain with a complex periodic structure remains a critical question to understanding the physics that drive the CDW in CsV_3Sb_5. Preliminary X-ray investigations of a potential CDW phase separation have suggested that the CDW domains form on the scale of hundreds of μm [40]. These results are consistent with optical studies [29] and scanning tunneling microscopy (STM) [42] measurements, however, a limited penetration depth consigns these observations to the sample surface.

The structural supercell distortion brought on by CDW order causes a transition

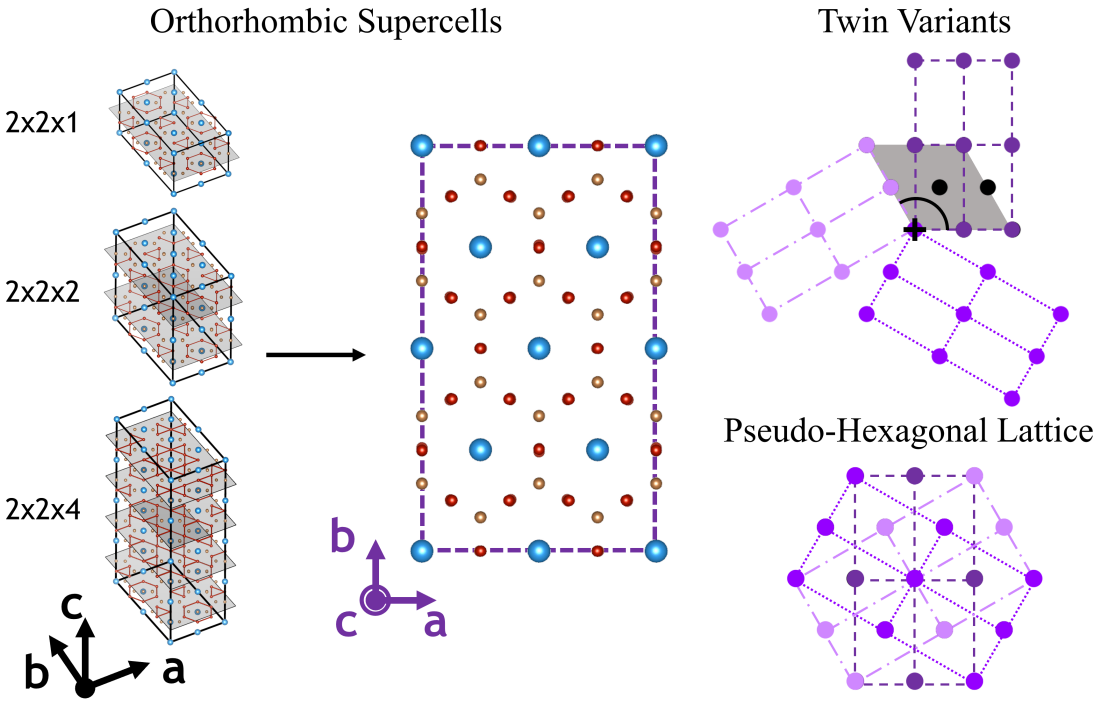

Figure 1.4: (left) Diagram showing the possible low temperature super-structures of CsV_3Sb_5, including the orthorhombic $2\times2\times1$, $2\times2\times2$, and $2\times2\times4$ cells respectively. A projection of the orthorhombic ab plane is also displayed. (top right) Schematic of real-space hexagonal lattice points (black) overlaid with the three orthorhombic twin variants (purples), aligned by their respective origins. (bottom right) Tri-twinned orthorhombic unit-cells, shifted to be aligned by their respective centers, displayed to demonstrate how local two-fold symmetry, can combine into a pseudo-hexagonal lattice with apparent six-fold symmetry across the average structure. The three twin variants are rotated by 120° about the c-plane normal and are displayed using varied shades of purple and line dash styles.

from the nominal hexagonal structure to an orthorhombic one. The rotational symmetry broken by the structural transition drives a rotational twinning along the stacking direction (about the c-axis). The structural twinning below T_{CDW} seen in optical birefringence measurements of CsV_3Sb_5 [29], is consistent with the existence of three orthorhombic twin domains rotated by 120° from one another. The diagram in Figure 1.4 illustrates how the rotational-twins, each with two-fold symmetry, can be combined to reproduce a pseudo-six-fold symmetry. This complicates the interpretation of conventional

X-ray scattering data, and motivates using a multi-length scale approach that combines momentum-resolved probes with spatial resolution below several hundred μm to study CsV_3Sb_5. This is relevant as understanding how these structural textures manifest and their intrinsic length scales remains vital to modeling the various symmetries reportedly broken below T_{CDW} in CsV_3Sb_5 [24].

1.4 Objectives

The primary objective of the research presented herein is to characterize the mesoscale structures of $NaMnO_2$ and CsV_3Sb_5 to explore potential magnetostructural coupling through an antiferromagnetic transition and possible phase separation driven by a charge-density-wave transition, respectively. By examining these materials across their intermediate length scales, this work aims to bridge the knowledge gap between their atomic-scale components and macroscopic behaviors. Characterization of this critical length scale is an essential step towards defining **where** phenomena occur within a material sample, leading to a deeper understanding of **why** a material exhibits exceptional properties, particularly those that emerge from their complex internal structures. These characterization efforts are led by the following hypotheses.

For $NaMnO_2$, it is hypothesized that Mn_3O_4 and β-phase intergrowths are uniquely distributed throughout the crystal's volume, which drive local structural changes that ultimately influence the material's bulk response. Additionally, it is proposed that twinning defects dominate the mesoscale structure, with twinned domains on the order of 100 μm. Resolving the spatial distribution of the myriad defect structures inherent to $NaMnO_2$ has significant implications for its electronic properties and viability as a cathode material. Another key hypothesis is that the observed magnetic transition at 45 K coincides with local nanoscale structural transitions from monoclinic to triclinic domains, suggest-

ing a complex interplay between magnetic and structural properties at low temperatures. Experimental observation of triclinic domain formation in nanoscale regions or evidence of local distortions due to ferrimagnetic ordering in Mn_3O_4 intergrowths would provide a valuable explanation for previous evidence of a bulk triclinic phase transformation in $NaMnO_2$.

In the case of CsV_3Sb_5, the hypotheses are focused on the low-temperature phase transition that forms a charge-density wave (CDW). It is suggested that the CDW transition results in the formation of two separate phases with 2c and 4c components, respectively. This phase separation is expected to be crucial for understanding the material's novel electronic phenomena. This thesis also investigates the hypothesis that the separated CDW phases inhabit large domains spanning hundreds of μm and that these domains spatially compete with one another during formation. Furthermore, it is proposed that structural distortions below the CDW transition, which result in an orthorhombic phase transformation, motivates the formation of three rotational twin variants. The connection of these variants to the formation of the CDW phases is also explored.

To test these hypotheses, advanced experimental techniques were employed on high-quality single crystal samples. The primary characterization method was Dark-Field X-ray Microscopy (DFXM), which is discussed thoroughly in the following chapter. The DFXM experiments performed on $NaMnO_2$ and CsV_3Sb_5 demonstrate two significantly novel implementations of the method, including an extension to low-temperature and full-field X-ray imaging of charge order peaks, respectively. This experimental work ultimately sought to identify local contributions to a supposed bulk magnetostructural transition in $NaMnO_2$ and determine the crystallographic source of fractional Fourier components within the CDW phase of CsV_3Sb_5.

1.5 Permissions and Attributions

1. The contents of this dissertation are the result of a collaboration, and have been published in Materials Characterization [43] and Physical Review Materials [44]. The content of these publications is reproduced here with the permission of UC Santa Barbara, Elsevier and the American Physical Society.

Chapter 2

Dark-Field X-ray Microscopy

2.1 Diffraction Background

Before giving a full description of Dark-Field X-ray Microscopy (DFXM), the concept of diffraction, or scattering, as an experimental technique for the study of crystalline solids is detailed here. Diffraction is a phenomena of electromagnetic radiation that results from light's wave-like behavior and its interaction with structures (obstacles or apertures) similar in scale to the wavelength of light. When this condition is imposed on a periodic arrangement of structures, each structure emits spherical waves that interfere with neighboring waves. A combination of constructive and destructive interference across wave fronts leads to the appearance of a periodic pattern of light. This concept was eventually applied to materials science by considering the periodic structure of the atomic lattice.

The theory behind the three-dimensional interference pattern produced by spherical waves from repeated atomic planes, was developed first by Sir William Lawrence Bragg in

1912. His work characterized elastic diffraction (*i.e.*, $k = k'$) using the following equation:

$$n\lambda = 2dsin(\theta) \tag{2.1}$$

where n is an integer describing the diffraction order (here, n=1), λ is the wavelength of light, d_{HKL} is the atomic spacing of the lattice planes with an associated normal vector (denoted by Miller indices H, K, and L) that is aligned with the momentum vector **Q**, and θ which describes the symmetric incident and diffracted angles of radiation. Measuring the intensity and angle of diffracted radiation from a given material provides unique information about the sample's orientation (θ), and atomic arrangement (d_{HKL}) based on the chosen length scale (wavelength). For a perfect crystal lattice, Bragg's Law predicts a Kronecker delta (δ_{ij}; $\delta = 1$ if $i = j$; $\delta = 0$ if $i \neq j$) when satisfied. In reality, diffraction experiments produce finite peaks with Gaussian or Lorentzian distributions because of subtle deviations in lattice parameter (strain) and/or orientation (mosaic). In this way, the width of a Bragg peak represents the relative disorder in or interruption of the otherwise perfect atomic lattice.

2.1.1 Reciprocal-Space and Fourier Transformations

Core to the applications of diffraction for the study of material structures is the concept of reciprocal-space and the mathematical transformation to and from that space, called a Fourier and an inverse-Fourier transform, respectively. Reciprocal space, also known as momentum space, is a mathematical construct used to describe the periodicity and symmetry of a crystal (*i.e.*, lattice structure) in terms of wave vectors rather than real-space coordinates. Each point in reciprocal space corresponds to a set of crystallographic planes in the real lattice, with the distance from the origin (1/Å) representing the inverse of the interplanar spacing (Å). The reciprocal lattice vectors are defined such

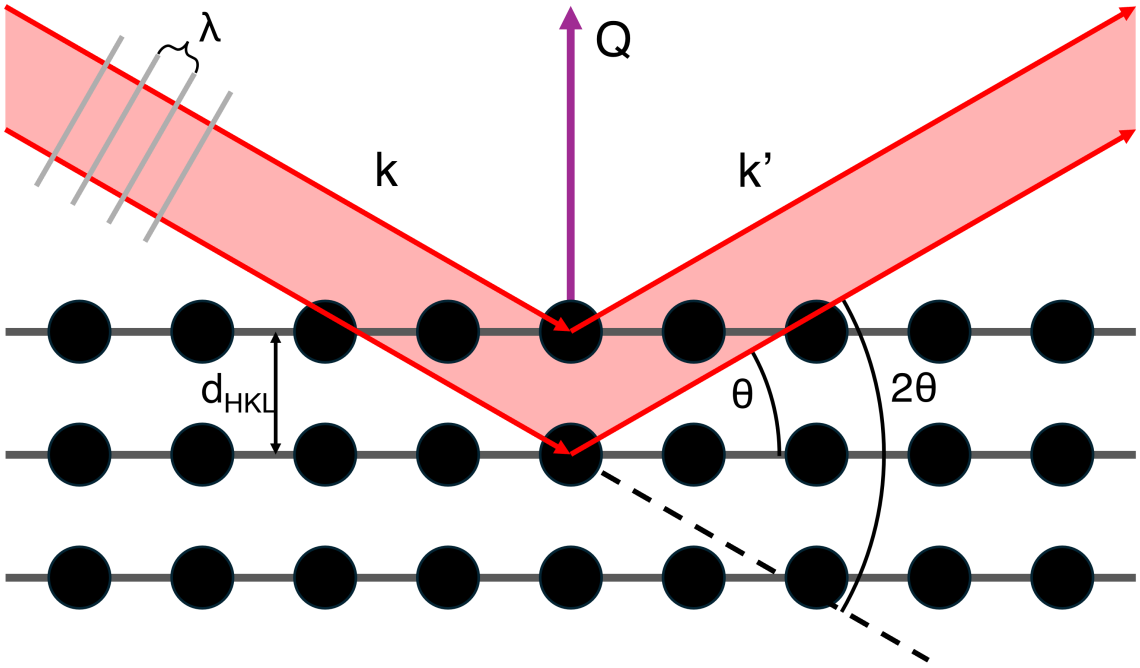

Figure 2.1: Schematic of Bragg's Law for elastic scattering that denotes the wavelength, λ, of the incident radiation, k, which impinges on atomic planes separated by a distance, d_{HKL}, before diffracting, k', at an angle, 2θ. This condition is satisfied when the reciprocal lattice vector, normal to the atomic (H, K, L) planes, coincides with the momentum vector, $\mathbf{Q}$, defined by the difference between the incident and exit radiation vectors.

that they are perpendicular to the crystal planes in real space, with their magnitudes being inversely proportional to their associated lattice parameters. Typically, reciprocal space values are denoted with the same letter as their corresponding real-space parameter with the addition of an asterisk. For example, the real-space lattice parameters a, b, and c, are associated with their reciprocal-space counterparts a^*, b^*, and c^*.

A Fourier transformation is then a mathematical operation that converts a function from its original domain (often time or space), into a wave-based (frequency) domain. Thus, Fourier transforms play a crucial role in understanding the results of X-ray diffraction by relating the real-space atomic structure of a crystal to its reciprocal space representation. The electron density distribution within a crystal can be described as

a function of repeating atomic sites in real space, while the Fourier transform of this distribution yields structure factors in reciprocal space, which represent the strength of the interference signal produced by diffraction. In practice, the measured peaks in a diffraction experiment are described by the reciprocal lattice of the material, inherently carrying information about the crystal structure's periodicity. By applying the inverse-Fourier transform to the measured peak intensities, one can reconstruct the real-space lattice of the crystal, averaged over the diffracting volume. The process of transforming reciprocal-space information back to real-space is foundational to using diffraction data to determine the fundamental structure of materials.

2.1.2 Radiations Types and Sources

While Bragg developed his theory using X-rays, diffraction can be similarly applied to other forms of radiation, namely electrons and neutrons. Scattering techniques leverage these three types of radiation to probe atomic structures, with each type of radiation spanning a different length scale and requiring a different source. Electrons have the highest energy (keV-MeV) and shortest wavelength ($\sim$pm), making them the most spatially sensitive. Techniques that employ electron diffraction to characterize crystal structures and materials, such as Transmission Electron Microscopy (TEM) and Electron Backscatter Diffraction (EBSD), have demonstrated extremely high spatial and angular resolution respectively. However, the strong probability for interaction between the probing electrons and the electron clouds surrounding the nuclei within the atomic lattice, causes swift energy loss and results in a shallow depth of penetration. While the penetration depth can be improved by using higher energy electrons, electron scattering techniques are largely limited to surface level information. In the case of TEM methodologies, a slice of material on the order of hundreds of nm must be excised from the bulk to enable

a transmitted signal to be measured. This process creates the potential for damage and surface effects to influence and cloud the results.

Often to achieve a material characterization that is a representative volume element of the macroscale behavior, more penetrative radiation is necessary. At the other end of the spectrum, thermal neutrons used for scattering experiments have the lowest energy (≤ 1 eV) and longest wavelength ($\sim$Å–nm). Neutrons, despite having a low energy, are the most penetrative because their neutral charge inhibits interactions with the electrons inhabiting the material structure. Interacting with the nuclei of a material also enables neutrons, unlike X-rays, to be used to probe structures composed of lighter elements. Despite their neutral charge, neutrons still demonstrate a magnetic polarization and are also often employed to probe magnetic structures. Their large penetration depth makes neutron scattering experiments non-destructive, but also requires single-crystal samples that are relatively large ($\sim$mm). Thus, neutron scattering techniques span the largest length scales, but this contributes to a reduction in spatial resolution through an averaging of the probed volume. Perhaps the most limiting factor in the use of neutron diffraction is the techniques dependence on a nuclear reactor as a source of neutrons.

X-ray diffraction techniques occupy the space between electrons and neutrons, using intermediate energies ($\sim$keV) and wavelengths (≤ 1 Å). Furthermore, X-ray scattering is commonly separated into soft and hard categories, representing lower and higher energy ends of the X-ray spectrum respectively. Soft X-rays, with energies typically in the range of 100 eV to 1 keV, are particularly suited for studying surface phenomena and thin films due to their limited penetration depth. On the other hand, hard X-rays, with energies above 5 keV, are essential for investigating bulk properties and deeply buried interfaces. This work focuses on the latter, which are an ideal source for the non-destructive investigation of bulk metallic compounds.

Conventional X-ray tubes, which produce X-rays by bombarding a metal target (typ-

ically copper or molybdenum) with high-energy electrons, provide an accessible and cost-effective option for many routine studies. These lab sources are sufficient for a wide range of applications, including phase identification, crystallography, and material characterization, but higher-grade intensity, flux and collimation can be achieved at synchrotron and X-ray Free-Electron lLsers (XFEL) sources. The X-ray work presented herein was collected using the synchrotron source at the Advanced Photon Source (APS) of Argonne National Lab. Synchrotron radiation sources generate high-quality X-rays through the acceleration of electrons around storage rings. At the APS, electrons moving near the speed of light pass through alternating magnetic fields within an undulator, which causes the electrons to oscillate and emit narrow bands of X-rays. The wavelength and energy of the X-rays can be tuned by changing the distance between undulating magnets. These higher energy X-rays penetrate more deeply into materials, making them ideal for high-resolution structural analysis in crystal systems.

2.1.3 X-ray Characterization

X-ray characterization is a cornerstone of materials science that typically begins with powder X-ray Diffraction (XRD). In powder XRD, a finely ground sample consisting of numerous randomly oriented crystallites is exposed to a monochromatic X-ray beam. The X-rays diffract according to Bragg's law and produce a diffraction pattern of concentric rings, consistent with the diffraction condition being satisfied for all crystal orientations. The radius of each ring is determined by the atomic spacing (d_{HKL}) and the ring width represents the range of lattice parameters within the sample. This pattern is characteristic of the material's crystal structure and allows for the determination of phase composition, lattice parameters, and crystallite size. The uniformity of the diffraction rings from a powder sample enable one-dimensional measurements to be performed ra-

dially, comparing independent intensity values to dependent diffraction angles (θ). By analyzing the positions and intensities of these diffraction peaks, researchers can identify the crystalline phases present and quantify their relative abundances.

Following the initial phase identification with powder XRD, single-crystal XRD is employed for a more detailed structural analysis. As the name suggests, this form of diffraction requires a high-quality single crystal sample of the material, which is mounted and aligned in a monochromatic X-ray beam. The crystal is then rotated, diffracting the X-rays to a series of discrete spots, with each spot (or peak) corresponding to a specific set of crystallographic planes. These diffraction spots are recorded on a detector, and the resulting data is used to reconstruct a three-dimensional electron density map of the crystal lattice. This map provides precise information on the atomic positions, bond lengths, and angles within the crystal structure. When combined with synchrotron source X-rays, single-crystal XRD is a particularly powerful tool for elucidating complex structures, enabling a comprehensive understanding of their crystallographic properties. Together, powder and single-crystal XRD data create a basis for the average atomic structure of the material, with analogous techniques available using neutrons and electrons. A multitude of other X-ray scattering techniques exist and relevant techniques will be detailed throughout the rest of text.

2.1.4 Microscopy and Imaging

Having explored the principles and applications of X-ray diffraction, the concepts of microscopy and imaging are now discussed. Microscopy can provide a complementary perspective by visualizing material structures with real-space contrast. Spatially resolved imaging techniques, such as X-ray microscopy and tomography, are indispensable for visualizing the arrangement and morphology of materials and their internal structures.

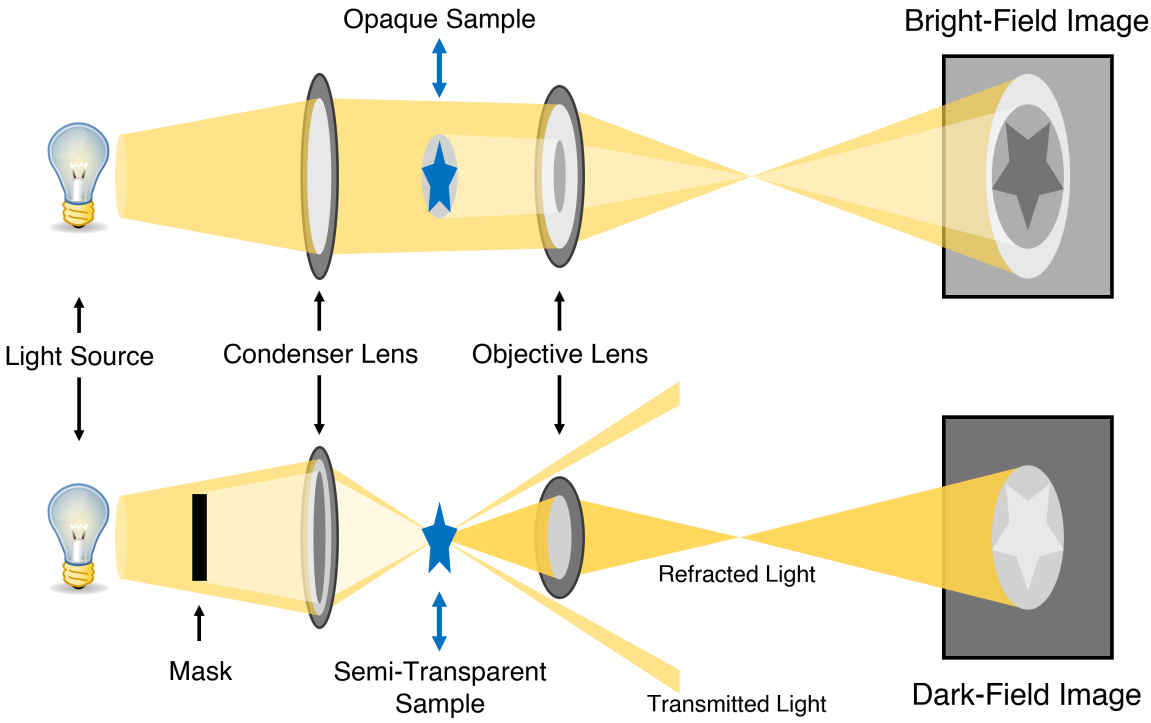

Figure 2.2: Diagram of two optical microscopy configurations; (top) bright-field mode and (bottom) dark-field mode. In bright-field measurements, the object casts a shadow that is magnified and collected on a detector at the image plane. Dark-field measurements require a more complex geometry that leverages the behavior of light through different media. The objects properties create a unique light source that is then similarly magnified and captured at the image plane.

Unlike scattering techniques that yield reciprocal-space data, microscopy captures the structure and composition of a sample directly, enabling immediate interpretation of its physical layout. Akin to optical microscopy, X-ray microscopy employs a refractive lens, or series of lenses, to magnify the signal before capturing it at the image plane. X-ray's refractive indices span a range that is close to but less than 1. This results in an opposite focusing and diverging behavior compared to visible light; a concave lens magnifies the incident column of X-ray illumination, while visible light is magnified with convex lenses. Consequently, specialized optics, such as X-ray zone plates or X-ray compound refractive lenses, are required to achieve effective imaging.

Within the realm of microscopy two illumination configurations exist, bright-field and

dark-field, with each mode used to enhance specific features of the sample (See Figure 2.2). While Figure 2.2 shows a schematic more common to an optical microscope, the same concept can be applied to X-rays through careful lens design. In bright-field microscopy, the image is formed by detecting X-rays that pass through the sample, resulting in a bright background with dark regions where the sample absorbs or scatters the X-rays; like casting an X-ray shadow. This technique is advantageous for observing the general structure and composition of the material, highlighting areas with varying density and composition. Conversely, dark-field microscopy detects X-rays scattered by the sample, producing images with a dark background and bright regions corresponding to illumination sources within the sample. This method is particularly effective for emphasizing fine structural details and detecting defects within the material. While bright-field imaging relies on contrast that originates from absorption effects, dark-field imaging depends on contrast from diffraction effects, with each methodology offering a different mechanism to produce complementary information.

By providing real-space contrast, X-ray imaging techniques offer direct visualization of the material's structure, complementing the atomic-scale reciprocal-space information obtained from scattering techniques. Combining these approaches allows researchers to achieve a holistic view of a material's structure and behavior, gaining insight into the underlying mechanisms that govern its properties.

2.2 Technique Description

The primary X-ray characterization tool employed in this work is a relatively new X-ray scattering technique, called Dark-Field X-ray Microscopy (DFXM). DFXM is a non-destructive technique, with the bulk sensitivity of hard X-rays, that provides a high-accuracy spatially resolved map of an ordered material's 'mesoscale' structure. Demon-

strated first at the European Synchrotron Radiation Facility (ESRF) in 2015 [45], DFXM can be described as an enhanced form of single-crystal XRD, whereby the diffracted illumination from a single Bragg peak is selected and used as the light source for a dark-field microscope. The first U.S. based DFXM experiment capabilities were demonstrated at the Advanced Photon Source of Argonne National Lab in 2018 [46]. DFXM images are created from illumination that originates from momentum (reciprocal) space but with the use of a lens, cast shadows based on contrast from real-space structures. The nature of this technique, which combines scattering and imaging into a single measurement, means the resulting maps possess spatial resolution and information about the local crystallographic orientation and strains. These features make DFXM an ideal technique for multi-scale investigations [47, 48]

The objective placed in the diffracted beam's path is commonly a compound refractive lens (CRL) well-suited for the relevant X-ray energies. The wavefront of the diffracted beam is focused by the objective to a point (at the back focal plane) before it is magnified, producing an image at regular intervals that is captured using an X-ray area detector (see Figure 2.3). This provides a full-field image due to diffraction contrasts from a plethora of heterogeneities (*e.g.*, twins, dislocations, phase boundaries, impurities, *etc.*) with an improved spatial resolution that depends on the magnification factor of the experimental setup. The image is formed at regular intervals with increasing magnification as the distance from the lens is increased. In practice, a resolution (transverse to the diffracted beam) on the order of 100 nm is expected, providing an exceptional resolution that typically requires the use of electron diffraction to achieve. The constant drive for higher resolution measurements couples to a proportional increase in effort towards mechanical alignment and experimental setup. A sample-to-detector distance ranging in meters and a CRL designed with a small numerical aperture (range of accepted incident angles) additionally enables a high angular resolution for DFXM, on the order of 0.001°. The

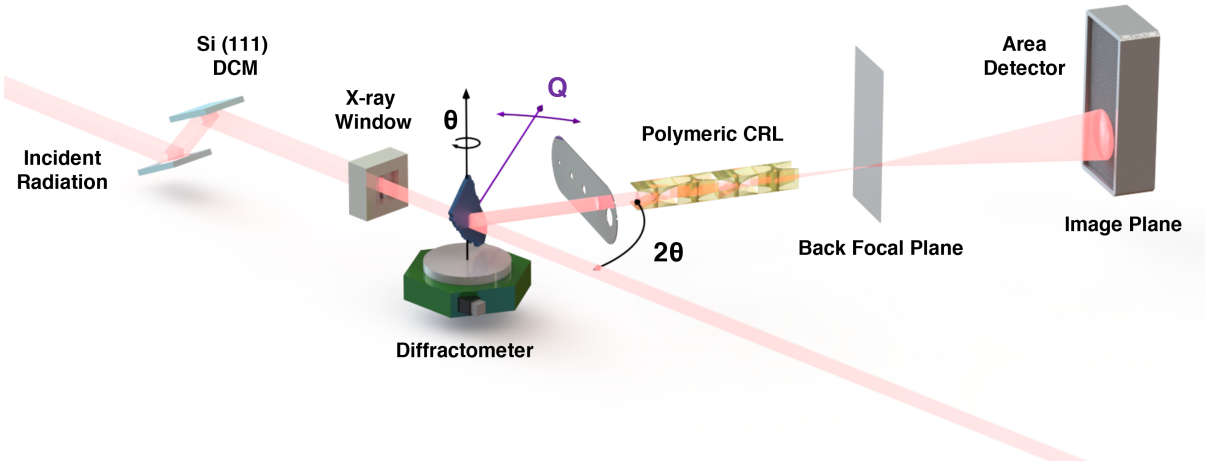

Figure 2.3: Schematic of a typical Dark-Field X-ray Microscopy (DFXM) experiment. Major components of the setup are labeled, including a monochromator, diffractometer, X-ray objective , and an area detector placed at the image plane. The X-ray path is visualized using a light red beam. The vertical rotation axis, about which the sample is rotated in θ for mosaic determination, is denoted in black, while the momentum transfer $\mathbf{Q}$ is denoted in purple. Dimensions are not drawn to scale.

caveat of this feature is that the orientation of the sample and Bragg peak of interest must be known *a priori*. However, once the peak is chosen, domains can be selected out amongst a highly varied pool (*i.e.*, a single grain out of hundreds in a polycrystal). A masking pinhole can also be placed just before the objective to filter out diverging light that would otherwise be scattered by the material surrounding the lens' effective aperture.

The use of an objective in this X-ray diffraction technique provides additional advantages over other characterizing techniques. A similar X-ray method, near-field High-Energy Diffraction Microscopy (HEDM), places an area detector close the sample ($\sim$5 mm) to collect diffraction signals with spatial heterogeneity. While this technique is powerful and can provide morphological information about the grain or crystal of interest, the short sample-to-detector distance limits the possibilities of in-situ testing. On

the other hand, a CRL used in DFXM has a working distance on the order of 100 mm, leaving ample space to employ a cryostat for temperature-dependent measurements, discussed below, and other sample environments (*e.g.*, load frame, magnetic field, *etc.*). The modular nature of DFXM provided by the design of the X-ray lenses (*i.e.*, the number of lenses, lens material and lens shape) further enables a "zooming" capability, which allows images to be collected across multiple length scales within the same experiment. This advantage can address the limits presented by the inverse relationship between field of view (FoV) and spatial resolution, making DFXM a truly multi-length-scale approach.

2.2.1 Experimental Considerations

As in other diffraction experiments, DFXM relies on a given material satisfying the Bragg condition in either a reflection or transmission geometry. The symmetric nature of the diffracting lattice planes enable the two geometric configurations theoretically, but practical considerations must me made for every experiment to determine a viable scattering geometry. In general practice, transmission geometry enables more diffraction peaks to be accessed but requires high-energy X-rays to successfully penetrate heavier materials. Reflection geometry overcomes the burden presented by X-ray absorption, but physically limits the angles of incidence depending on the sample's aspect ratio and size. Additionally, reflection geometry is more surface sensitive than transmission mode, which adds a level of complexity to sample preparation as the resulting data benefits greatly from a uniform surface roughness.

The attenuation length (also known as the absorption length) is the distance through a given media in which the X-ray intensity decreases by a factor of $1/e$. The attenuation length is inversely proportional to the density of the material and it scales logarithmically with increasing energy. When the sample thickness is approximately equal to the

attenuation length, the incident monochromatic X-rays will lose ≈37% of their intensity as they pass through the sample. This relationship is used to determine if the diffracted intensity is sufficient to enable transmission geometry, or if not, the probed depth of the diffracting X-rays in reflection geometry. Another important consideration is the angle of incidence of the radiation, as the total number of photons hitting the sample surface begins to spread across a larger area. Because of this, the attenuation length should be calculated for a range of angles that encompass the relative rotation required to measure the relevant Bragg peaks. For transmission and reflection geometries, samples should be on the order of the attenuation length at 70° and 20°, respectively. The level of X-ray absorption within the material also controls the probed or illuminated volume that contributes to the diffraction signal, indicating the depth of information that contributes to the resulting images. This can be leveraged to investigate surface level and/or bulk structures within the material, depending on the specific interest of each measurement.

An essential experimental consideration for DFXM, beyond transmission or reflection geometry, is the selection of optical components. For the X-ray objective, several options are available. One option is a zone plate, which is a circular diffraction grating composed of concentric rings that alternate between opaque and transparent materials. Zone plates focus X-rays through diffractive means, and they are highly chromatic, meaning their focal length is dependent on the wavelength of the X-rays used. While zone plates can provide exceptional magnification, they become less effective at higher energies (above 10 keV) due to the increasing thickness required to maintain appropriate aspect ratios, leading to fabrication challenges.

An alternative to using a zone plate, is the use of refractive lenses as objectives. A single refractive X-ray lens has too long a focal point for effective focusing. However, by combining multiple refractive lenses into a compound refractive lens (CRL), X-rays can be effectively focused on the meter-length scale necessary for synchrotron setups. The

CRLs discussed in this work are made from X-ray-transparent beryllium or a polymer called SU-8. These lenses can either be fabricated into paraboloids, which focus in two dimensions simultaneously, or composed of alternating one-dimensional lenses, which increase the total lens length but are easier to fabricate. CRLs are advantageous for higher energies compared to zone plates because their sizes are less limiting. CRLs also offer an advantage in being operable as transfocators, altering the number of lenses in the configuration to tune the focal length appropriately. Zone plates, on the other hand, require fabrication of a new plate to achieve the same effect.

In DFXM, the use of a condenser before the sample can also be beneficial to tune the spot size of the incident X-rays and increase the total flux of photons, enhancing imaging contrast. A CRL can be additionally employed as a condenser to focus the light before the sample, while another option is the use of a Kirkpatrick-Baez (KB) mirror. KB mirrors are reflective devices made of ceramic and coated with a heavy metal layer, precisely machined to maintain the critical angle of reflection for X-rays. They can achieve two-dimensional focusing either through a circular tube-like mirror or by using two one-dimensional focusing mirrors in series. The reflective nature of KB mirrors offers an advantage to CRLs by eliminating a source of light absorption due to refraction. However, as with zone plates, higher energy X-rays necessitate larger and heavier mirrors, eventually posing fabrication challenges.

Once the optical components for condensing and objective purposes are determined, it is crucial to characterize these components to ensure image quality and assess potential data inconsistencies. One method for characterizing lenses is Talbot interferometry. This method is based on the Talbot effect, which describes a phenomenon whereby illuminating a diffraction grating with planar waves of light results in an image of the grating (Talbot image) appearing at regular intervals of the Talbot length. The Talbot length, z_{T}, can

be calculated using the following equation:

$$z_{\mathrm{T}} = \frac{\lambda}{1 - \sqrt{1 - \frac{\lambda^2}{d^2}}} \tag{2.2}$$

where λ is the wavelength of the incident light and d is the periodic spacing of the diffraction grating [49]. By placing the lens before the grating, alterations to the exit wavefront and the subsequently formed Talbot image due to the lens can be analyzed, allowing a back-calculation for important optical characteristics, such as aberrations and focal length. See Refs. [46, 50, 51] for details of CRL 'zoom'-lens design and characterization using Talbot interferometry. The selection and characterization of optical components are vital considerations for optimizing DFXM setups, ensuring precise and effective imaging capabilities.

Another key experimental consideration for DFXM is the choice of detector, which generally falls into two main categories. The first is the conventional scintillator-based detector, which consists of a scintillator that converts X-ray photons into visible light, a 45° mirror that redirects the light vertically for a more compact setup, and an optical objective that increases magnification before the image is captured on a charge-coupled device (CCD) or complementary metal-oxide-semiconductor (CMOS) sensor. The second type is the direct X-ray detector, or single-photon counting detector, which uses a photoelectric material that directly detects X-rays, much like how a CCD or CMOS sensor detects visible light. Essentially, this configuration bypasses the intermediate step of converting X-rays into visible light, as seen in scintillator-based detectors.

These differences result in significant property variation between the two detector types [52]. In the conventional detector, the scintillation process comes at the cost of increased X-ray absorption, resulting in photon loss. However, this conversion allows for the use of an optical objective with a shorter focal length than an X-ray objective,

enabling higher magnification without significantly increasing the overall size of the system. On the downside, the scintillating decay time, which is the time it takes for the material to emit light after excitation, further impacts temporal resolution. Direct X-ray detectors, while potentially offering lower spatial resolution due to the absence of optical magnification, provide higher sensitivity, allowing for the detection of weaker signals and enabling higher count rates. These detectors also offer improved temporal resolution, as they eliminate delays associated with converting X-rays to visible light and reduce exposure times needed to capture sufficient signal intensity [52]. Enhanced temporal resolution is crucial for dynamic imaging applications, such as those using pump-probe techniques, where materials are imaged after being excited by a laser to observe the propagation of thermal or acoustic waves [53]. Improving temporal resolution, when combined with the use of highly coherent light, is essential for solving the phase problem and pushing resolution limits in diffraction and diffraction-based imaging techniques.

2.2.2 Scanning Methodologies

Once the experimental setup is complete, various scanning methodologies are employed to probe specific properties of the material of interest. The primary methodology used during these measurements is Rocking Curve Imaging (RCI). In this method, multiple images are collected at a single Bragg peak as the sample is rotated through various orientations (θ). As the sample rotates, the reciprocal lattice vectors (G) corresponding to the atomic (H, K, L) planes, which may be misoriented from each other across atomic domains, will satisfy the Bragg condition (*i.e.*, G = Q) at different sample orientations. By rocking the sample back and forth and collecting images at each orientation, the orientation spread of the atomic planes within the illuminated region are measured. In single-crystal samples, the orientation that corresponds to the highest measured intensity

indicates the largest proportion of atomic orientations (average orientation) within the illuminated volume, while areas with lower intensity represent finer structural features. This scanning methodology provides a comprehensive description of the material's orientation spread and dominant versus weak beam profiles. When combined with DFXM, it allows the spatial distribution of this information to be resolved in a local area of the sample, offering images representative of both average and local crystal structures.

Another important scanning method is the theta-two-theta scan. In this method, the sample is rocked in θ while simultaneously rotating the detector placed at the image plane about the same axis. This variation of the two-theta angle inherent to the Bragg condition in addition to rocking the sample at half of that angle, changes the magnitude of the probed momentum vector, Q, and corresponding reciprocal lattice vector, G, without altering their relative orientations in real or reciprocal space. This scanning method probes the spacing between atomic planes, directly related to the lattice parameter of the material. As the lattice parameter varies, due to strain, the intensity of the diffracted signal varies accordingly, indicating regions with varied lattice parameters. Thus, a theta-two-theta scan provides insights into the material's strain, which can be correlated to the material's average and local structures in a similar way as the mosaic spread.

Additionally, an area scanning methodology can be employed in DFXM. Similar to techniques like Scanning Transmission Electron Microscopy (STEM) and Scanning Tunneling Microscopy (STM), this method involves rastering the sample to different locations, changing the illuminated volume's position on the sample. Measurements are taken at various positions across the sample's area, which can be stitched together in post-processing to produce large area maps composed of images with smaller fields of view. In this work, area scanning is combined with RCI to produces spatially resolved maps of spectral parameters, including mosaic distribution, across multiple length scales. Employing these scan methodologies within the framework of DFXM leverages these ad-

vantages with exceptional spatial resolution, allowing the investigation of crucial material characteristics across the mesoscale.

2.3 DFXM Data Analysis

Once images have been collected from the Dark-Field X-ray Microscopy (DFXM) experiment, they undergo a series of preprocessing steps to enhance contrast before analysis. Preprocessing often involves image summation, where several images taken at the same sample position and under the same conditions are added together to increase the signal-to-noise ratio and improve peak statistics. Another critical aspect of preprocessing is the transformation of images to the material reference frame relative to the detector or camera reference frame. This ensures that the images accurately represent the sample's structure, based on the orientation determined before experiment. Additionally, images may be cropped to reduce their size and focus on particular regions of interest.

Preprocessing also includes a background subtraction to reduce statistical noise and enhance image contrast. Background subtractions performed here were based on the previous work of Garriga Ferrer *et al.* [54], and employed a combination of up to three major steps, including dark-detector subtraction, hot pixel removal, and a simple thresholding. Dark-detector subtraction involves subtracting images taken on the X-ray detector with no illumination (beam off or unsatisfied diffraction condition). If no dark-detector images are collected during experiment, several images from the ends or tails of a rocking curve image scan, where the Bragg condition is not satisfied, can be used to create a dark-detector image. This was be done using the mean or median of these zero-intensity images. Hot pixel removal is performed by first creating a 2D median-filtered version of the image. Hot pixels, identified as any intensity in the original image that is three times higher than the highest value of the median-filtered image, are then replaced with pixel

values from the median-filtered image. Finally, thresholding is applied, whereby pixels with intensity below a certain percentage of the maximum intensity (often 1-10%) are set to zero. Background subtraction is crucial not only for enhancing contrast but also for reducing computation time during subsequent analysis.

After noise removal is completed, images are analyzed by calculating key spectral parameters that are characteristic of the system's periodic structure. Integrating the intensity across DFXM images collected during Rocking Curve Imaging (RCI) scans and plotting the calculated intensity against θ produces a one-dimensional curve, similar to intensity curves from conventional X-ray Diffraction (XRD). Applying this concept on a pixel-by-pixel basis, assuming a 1:1 mapping of pixels to material points, results in a spatially resolved image of rocking curve information. Thus, DFXM analysis follows a procedure where the intensity of each pixel is plotted across θ values (slices) and fit with a Gaussian curve. The curve fitting parameters of interest are the maximum intensity or amplitude of the peak, the peak's center of mass (μ) or mosaic, the full width at half maximum (FWHM) of the curve, and the integrated area under the peak's curve. These parameters were subsequently mapped across every pixel in a representative image, producing visualizations that highlight data contrasts stemming from different material properties [55]. Examples of these images are displayed and discussed further in the following chapters.

Proper interpretation of the images requires an understanding of what each parameter represents physically in the material sample. The maximum intensity or amplitude of the peak represents a combination of factors, but is primarily determined by the structure factor of the specific HKL peak being investigated and the volumetric proportion of atomic planes that contribute to strong scattering. The center of the peak indicates the average orientation of the atomic planes within the illuminated volume, while the full width at half maximum (FWHM) reflects the relative disorder in the crystal lattice,

with a broader peak indicating increased disorder and a narrower peak indicating higher crystallinity. Integrating the area under the peak's curve is representative of the total scattering volume, including both strong and weak scattering conditions.

The resultant DFXM images provide detailed visualizations of the material's properties, highlighting contrasts due to different material characteristics. However, collecting these rich, multi-dimensional image stacks during a DFXM experiment often leads to the production of hundreds of gigabytes of data that can be challenging to assess. Given the large data sets produced during a DFXM experiment, efficient storage, processing, and analysis are essential. This necessitates effective preprocessing and background subtraction to limit the number of pixels for fitting and emphasizes the need for fast analysis methods, potentially incorporating parallel processing or machine learning. Processing and analyzing such large visual data sets is an ongoing research effort and presents an additional challenge to this research.

2.4 DFXM Applications

Although somewhat recently developed, Dark-Field X-ray Microscopy (DFXM) has already been used to study structure-property relationships in a variety of materials (Refs. [47, 48] and the references therein). Specific to complex defect structures, the technique has been used to identify individual dislocations and the strain fields around them [56–58], while another DFXM study of crystal defects in steel (twinning, stacking faults, precipitates, *etc.*), used the images to identify specific defect features [59]. DFXM measurements have been largely focused on polycrystalline metals, but its application to study complex phase transitions and condensed matter physics is rapidly growing.

Despite these promising results, the effective use of DFXM beyond room-temperature studies remains a challenge, particularly at the cryogenic temperatures frequently en-

countered in investigations of quantum materials. This is due to competing requirements of low vibrations and mechanical stability, versus the operational demands and physical connections of a cryostat mounted on an X-ray diffractometer. The previously mentioned materials, $NaMnO_2$ and CsV_3Sb_5, demonstrate some of their most interesting magnetic and electronic properties at low temperatures. The transition temperatures of interest mandate the ability to perform material studies well below the temperature of liquid nitrogen (75 K), nearer to the temperature of liquid helium (4 K). Cryostats are regularly employed to study materials at these temperatures but their combination with a synchrotron-source X-ray diffraction experiment is a non-trivial challenge.

Concurrent with the lack of low-temperature DFXM experiments is a limitation of its applications to inherently lower intensity diffraction peaks. For materials like CsV_3Sb_5 that exhibit complex diffraction patterns due to physical phenomena like charge-density waves (CDW), low-intensity Bragg peaks pose a significant challenge for DFXM imaging, which is complicated by the inherent absorption of the aforementioned optical components. Furthermore, achieving adequate X-ray contrast becomes increasingly difficult to maintain as the drive for higher spatial resolution is pursued. The same challenge exists for the possible extension of DFXM to other weakly scattered diffraction peaks, such as those produced during magnetic, anomalous, or resonant X-ray scattering measurements, to name a few.

This work demonstrates two major advancements of this technique's applications, including an extension to low-temperatures and a demonstration of a novel charge order investigation. These DFXM experiments included collecting magnified-real-space diffraction-contrast images using a standard rocking curve scan methodology, with the unique benefit of in-situ cooling and heating across a range of temperatures from 3.2 K to 300 K. The first demonstration of dark-field imaging CDW structures was achieved by van Landuyt *et al.* [60] in 1975. This pioneering work employed electron microscopy

to capture images of irrational satellite peaks in $NbTe_2$, however the methodology was not extended to X-rays for bulk measurements until now. The experiment performed on CsV_3Sb_5, detailed in Chapter 5 of this thesis, demonstrates the first example of leveraging DFXM's capabilities for direct observation of a charge-density wave using high-energy X-rays. This experimental work establishes an original approach to characterizing thermal phase transformations of crystal, electronic, and magnetic structures in complex crystalline materials.

Chapter 3

Applied Material Study: $NaMnO_2$

3.1 Room Temperature Survey

Prior to investigating the low temperature transition in $NaMnO_2$, its defect structure and complex crystal structure were measured at room temperature to establish a baseline picture of the material using Dark-Field X-ray Microscopy (DFXM). For this study, a large single-crystal sample of $NaMnO_2$ was grown using a floating zone technique [11]. The high angular resolution of DFXM requires knowledge of the sample orientation prior to the experiment. As determined via Laue diffraction, $NaMnO_2$ forms a facet during growth along the (1, 0, $\overline{1}$) lattice plane, which also serves as a cleavage plane during sample preparation, with the short b-axis extending parallel to the growth direction. The $NaMnO_2$ sample was cleaved along this plane and cut to a size of approximately 20 $mm \times 3\ mm \times 2\ mm$ for the initial room temperature survey.

Solid-state nuclear magnetic resonance (ssNMR) experiments were conducted previously on samples grown using this method to estimate the sample's population of stacking faults and β-phase content with reference to the primary α-phase. The sample used here derived its Na content from approximately 96% α-phase, 4% stacking fault regions and

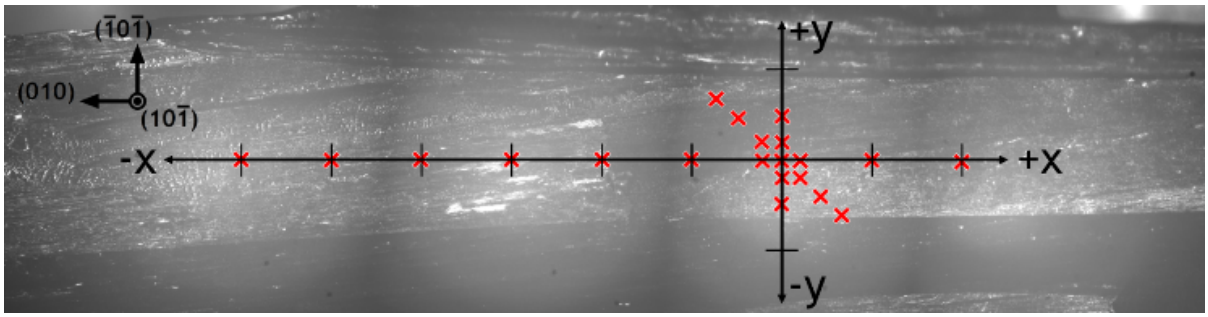

Figure 3.1: Series of images taken of the sample during a room-temperature survey that were stitched together using a grid/collection stitching plugin [61] and ImageJ [62]. An axis is overlaid to indicate the position at which Dark-Field X-ray Microscopy (DFXM) scans were conducted over the sample area, and notches are placed at mm increments. Red Xs indicate the locations where scans were conducted. The upper left axis indicates the orientation of the single crystal sample.

$< 1\%$ β-phase [11]. The relatively low β-phase content of the sample enabled the DFXM study to focus primarily on the effects of twinning and stacking faults within the majority α-phase. However, the additional presence of Mn_3O_4 intergrowths, albeit minute ($\sim 6\%$), may contribute to diffraction contrast, creating difficulty in uniquely identifying some defects.

The sample was glued to a sample mount using GE varnish with its $(2, 0, \overline{2})$ reciprocal lattice vector oriented in the horizontal scattering plane, consistent with a reflection geometry. It was then positioned and aligned with the X-ray beam center using a video microscope unit (VMU), configured with a $2\times$ objective and a 5-megapixel Flir CMOS camera, oriented with the optical axis aligned to the crystal surface normal. The optical microscope also enabled reference images to be collected through the various sample movements involved in the area scanning methodology. Figure 3.1 shows the stitched reference images, overlaid with red Xs to indicate the various probed locations across the sample surface. Employing an area scanning methodology, images were collected at positions across the sample, spanning several millimeters in the horizontal (b) direction and about one millimeter in the vertical direction. Additionally, a series of vertically

varied Rocking Curve Imaging (RCI) scans were performed after rotating the sample by 20°, resulting in the diagonal location spread presented in Figure 3.1.

The considerations for reflection and transmission geometry were discussed in section 2.2.1, which are based on the attenuation or absorption length of X-rays through the material. This length is largely dependent of the wavelength of X-rays used ($\lambda = 0.95$ Åfor 13 keV X-rays) and the material's density ($\rho \approx 4.22$ g/cm^3). The absorption length gives an estimate of the X-ray penetration depth, providing critical information about probed volume of the sample's internal structure during data analysis. Another important consideration in calculating the penetration depth is the grazing angle of the incident radiation, which geometrically increases the total distance traveled for every increment in depth penetrated. In reflection geometry, this angle is approximately 10° to 15° for the $(2, 0, \overline{2})$ Bragg peak. At 13 keV, the attenuation length is approximately 13 μm. In reflection geometry, the X-rays penetrate the sample and diffract out of the same surface, effectively doubling the path length of the diffracted X-rays. Therefore, the calculated penetration depth of 13 μm results in a probed depth of approximately 6.5 μm.

3.1.1 DFXM Setup at 6-ID-C

The room temperature survey DFXM experiment was carried out at 6-ID-C experimental station of the Advanced Photon Source (APS) at Argonne National Laboratory. The experimental setup was *ad hoc* and consisted of the following major components. A monochromatic X-ray beam, tuned using a Si (111) double-crystal monochromator (DCM) was passed through a pair of entrance slits forming a 300 $\mu m \times 300$ μm square beam to uniformly illuminate the sample. A beryllium-based compound refractive lens (CRL) consisting of a series of 2D parabolic lenses, in groups of 8, or 16, was used as a condenser, which focused the incident beam to a 50 μm spot size. The diffracted beam

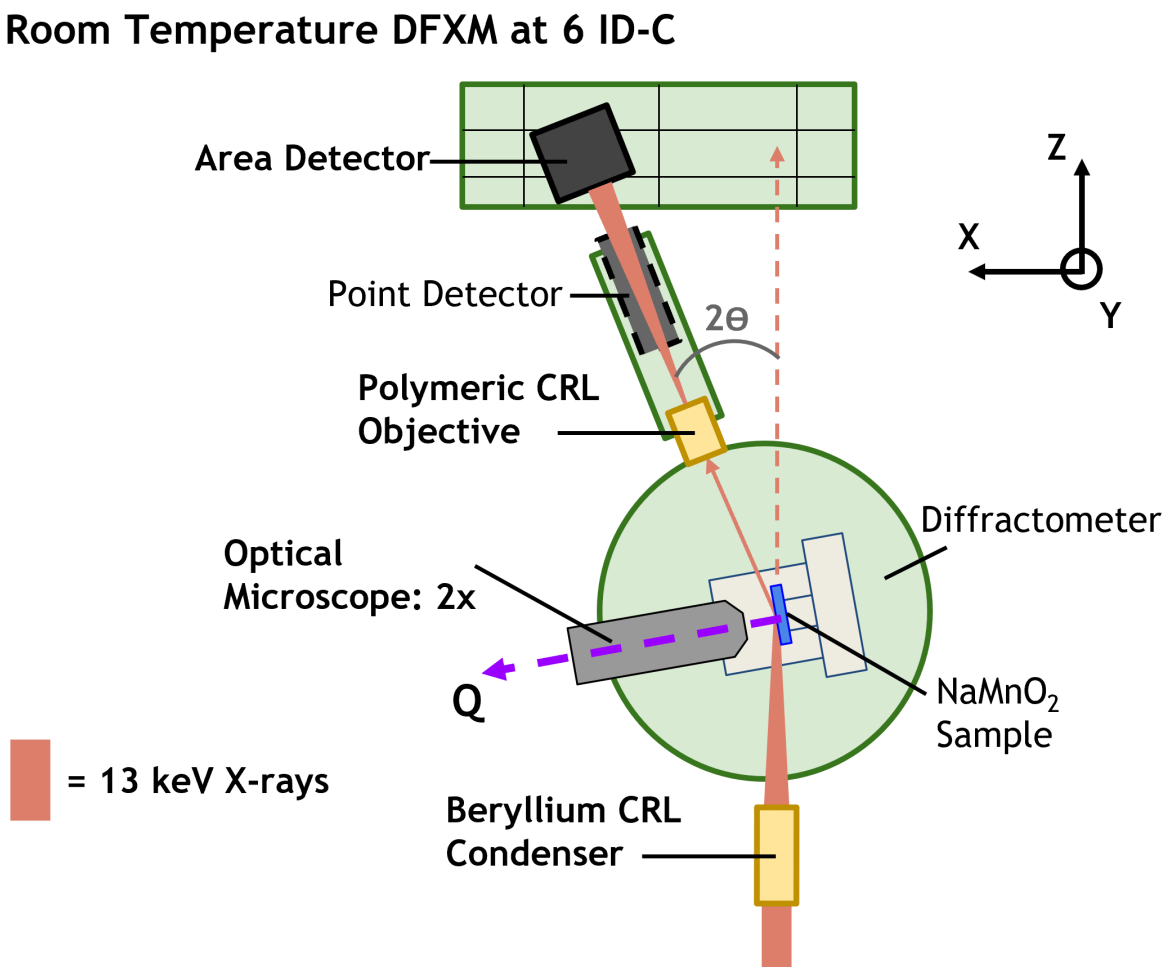

Figure 3.2: Schematic of the experimental setup used for Dark-Field X-ray Microscopy (DFXM) at room temperature to survey a large (mm) single-crystal sample of $NaMnO_2$. The diagram is drawn from a top-down perspective to demonstrate the horizontal diffraction geometry, which was performed in reflection mode.

was magnified using a polymer-based (SU-8) CRL, designed to have a short focal length (100 mm) at 13 keV[50, 63].

A single-photon-counting sodium iodide point detector was initially used to optimize the $(2, 0, \overline{2})$ Bragg peak ($2\theta = 30.5°$) and to characterize its profile, aided by sample manipulation stages. Once optimized, the point detector was moved out of the way and the diffracted beam was allowed to travel to the image plane, where it could be recorded using an area detector. The area detector used for this experiment consisted of

an anti-reflection coated LuAG:Ce scintillator (0.02 mm thick and 10 mm diameter) that converted the magnified X-ray beam to visible light, followed by a 45° reflective mirror, a high resolution 5x optical objective and Andor's Zyla 5.5-megapixel sCMOS camera, respectively. The Zyla detector was positioned at the image plane to capture data in the form of 16-bit, 2560x2160 pixel tiffs. The optical magnification combined with the X-ray magnification of the polymeric CRL, resulted in an 86x total magnification for the room temperature survey. The native pixel size of the sCMOS is 6.5 × 6.5 $\mu m2$, so the effective pixel size for the experiment was 76 nm.

3.1.2 Room-Temperature Results

DFXM images were collected by stepping θ through the $(2, 0, \overline{2})$ Bragg peak of $NaMnO_2$ in 0.002° increments to obtain the material's mosaic spread, using the RCI methodology discussed in section 2.2.2. RCI is carried out before microscopy to assess the full range of mosaic spread and to ensure that chosen region is a good representation of the entire sample. In Figure 3.3, a representative DFXM intensity image is presented (Figure 3.3(a)), along side an associated integrated intensity rocking curve (Figure 3.3(b)), and the derived mosaic and full width at half maximum (FWHM) images (Figure 3.3(c,d)) from room-temperature measurements. The intensity image was generated by mapping each pixel's maximum intensity over all frames collected at a given location. The images shown in Figure 3.3 were collected using the low temperature setup described in section 3.2.1, however they provide a larger field of view and posses the same character as the room temperature images collected for the survey.

Clear contrasts arising from slanted linear boundaries, mutually separated by a range of distances, are observed. The angled linear boundaries align with the b-direction or growth direction of $NaMnO_2$. These boundaries, visible in optical microscope images,

extend along the growth direction and correspond to microscale cracks that nucleate on the surface of the material. The boundaries exhibit a deficit in diffraction contrast and are consistently observed across the sample, creating domains averaging $\approx 20\ \mu m$ in width. These lines appear at an angle of approximately 30° and are highlighted by orange dashed lines in Figure 3.3(a). The severity of the angle is due to the geometric peak spreading on the sample surface caused by the low scattering angle of the incident beam. The horizontal scattering geometry results in the X-ray beam spreading horizontally to an elliptical spot size that spans 50 μm vertically, and 250 μm horizontally. Despite this surface spread, the diffracted signal exits at an equivalent angle and is projected onto the image plane, maintaining an equiaxed profile, albeit magnified. Consequently, the actual physical spot size must be calculated and it should be understood that the effective pixel size differs in the vertical and horizontal directions. When evaluating the triangular relationship of the adjusted dimensions, the angle of the linear boundaries becomes significantly shallower, aligning with the lines seen in optical microscope images. This confirms that the boundaries possibly result from microcracks or intergrowths that align with the growth direction. The width of these boundaries in the 10× optical microscope image, approximately 20 μm, supports this finding. Furthermore, non-uniform features are visible along the 'ridges' of linear domains. Considering the differences in resolution (horizontal and vertical), the effective length of these modulations are calculated to to be around 13 μm. The intensity variation along the long-axis of the domains is more subtle, indicating these domain boundaries likely come from low-angle mosaic variation or local defect structures.

A Bragg-peak line profile obtained by the point detector shows a total mosaic spread ∼0.1°. By integrating each image, a near-identical line profile was obtained. As the sample is rocked, crystal domains with varied reciprocal lattice vectors are rotated through the Bragg condition, causing different pixels to illuminate. As previously described in

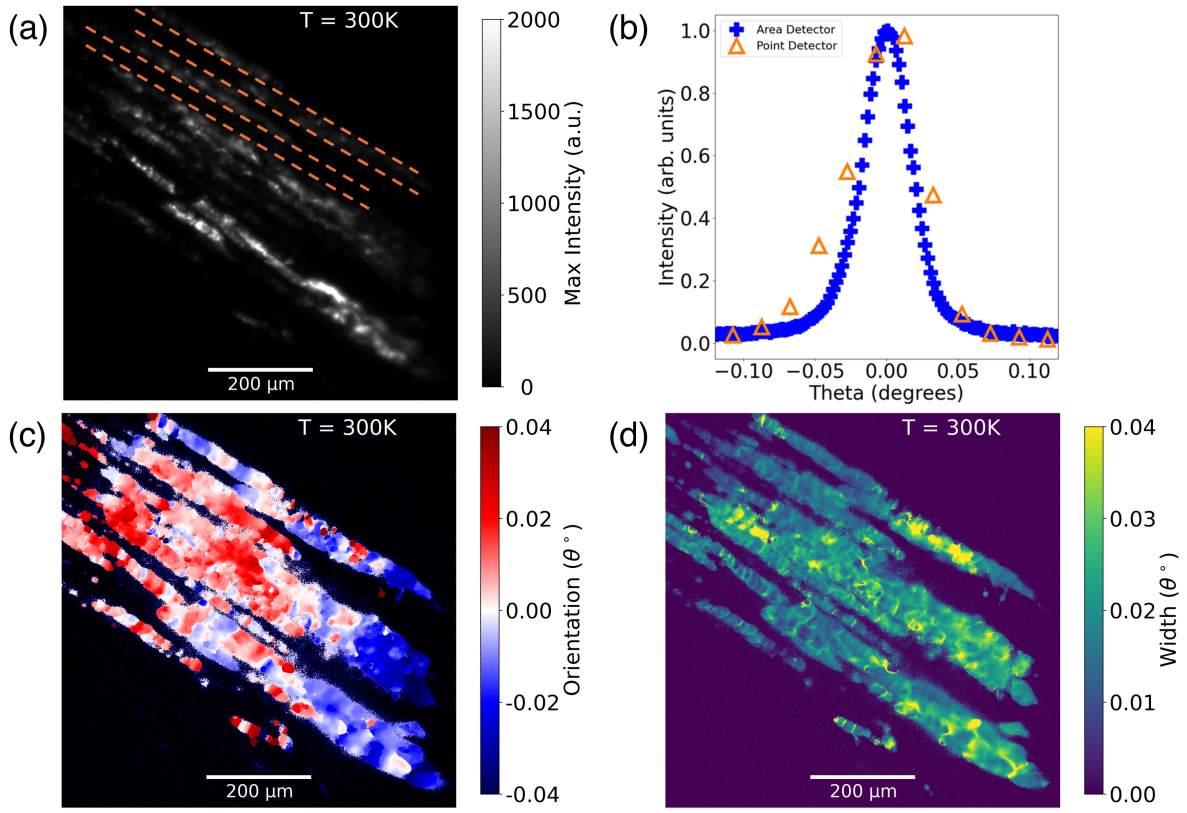

Figure 3.3: A typical intensity image (a), corresponding mosaic map (c) and width map (d) of $NaMnO_2$, captured at room temperature. Orange dotted lines in (a) guide the eye to defect boundaries. Intensity measurements through the rocking curve scans were collected with a point detector and by integrating the intensity over the images captured by the area detector (b).

section 2.3, the mosaic image is created by finding the center θ value of each pixel's intensity peak, labeling local regions based on their deviation from the principal crystallographic peak. The mosaic map in Figure 3.3(c) shows a gradient distribution of local orientation with an overall spread consistent with the Bragg-peak profile discussed above. These measurements, performed over spots shown in Figure 3.1, indicate that the sample does not have drastic changes in its mosaic distributions across its millimeter length scale.

Out of the 22 positions labeled in Figure 3.1, 14 produced patterns resembling the material structure, while the remaining positions did not satisfy the Bragg condition due

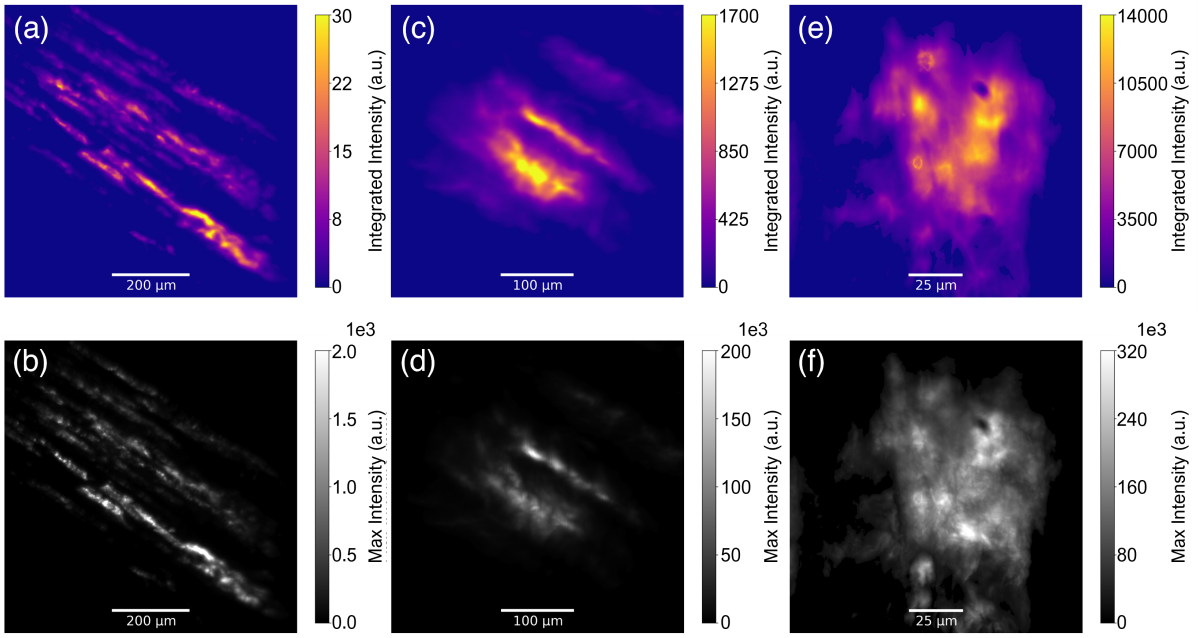

Figure 3.4: Dark-Field X-ray Microscopy (DFXM) images of integrated intensity (a,c,e) and maximum intensity (b,d,f) captured from $NaMnO_2$ across various length scales. The total magnification for the images increases from 38x (a,b), to 86x (c,d), and finally 400x (e,f), which highlights domain structures and heterogeneities across $NaMnO_2$'s mesoscale.

to interference from the exit slits or other objects obstructing the diffracted beam. The high angular resolution required for resolving images highlights one of the challenges of DFXM, demanding precise sample positioning and setup geometry, especially given the limited experiment time at synchrotron sources. Precise alignment of the lenses and identification of an optimal sample location to produce a strong diffraction peak remains a significant obstacle and an active research area. Overall, when a diffraction signal is received, similar linear features, intensities, FWHM, and mosaic spread is observed in the resulting images. This indicates that the measured single crystal is relatively uniform across its spatial dimensions.

Observations of $NaMnO_2$ across the various length scales probed using DFXM are also presented for evaluation in Figure 3.4. Here, the multi-length scale imaging was

achieved by employing different types of objectives through the various experimental configurations described in this chapter. Figure 3.4 shows images of integrated and maximum intensities through RCI scans of $NaMnO_2$ at room temperature, captured at three different magnifications: 38x, 86x, and 400x. These correspond to experiments detailed in the sections on the low-temperature experiment, room temperature survey, and split peak and Fridel pair studies, respectively. Each magnification resulted in optimal effective pixel sizes of 171 nm, 76.5 nm, and 16.25 nm, and expanded effective pixel sizes of 627 nm, 295.6 nm, and 65.8 nm, respectively.

As the magnification of the DFXM imaging is increased, the feature resolution becomes increasingly limited by the diffraction resolution limit of the technique. The theoretical diffraction limit is calculated using the F-number (f/#) of the lens, which is the ratio between its focal length and effective aperture, and the wavelength of incident light. In all of the DFXM setups presented here, the theoretical diffraction-limited resolution is around 100 nm. Practically, a resolution of 240 nm line pair has been demonstrated at 6-ID-C of the APS [50]. Reaching the theoretical diffraction limit is challenging due to lens imperfections, beam divergence and other experimental factors. Nonetheless, this technique allows us to observe $NaMnO_2$ across the mesoscale: visualizing linear domain structures within a field of view (FoV) on the order of hundreds of μm; refining the texture within these domains across tens of μm; and at 400x magnification, single domains with complex microstructures are revealed, demonstrating a myriad of domain boundaries and contrast features. Spanning these length scales, a comprehensive understanding of $NaMnO_2$'s local inhomogeneities is achieved for a bulk single crystal. Future experiments benefit from leveraging these observations to relate local heterogeneities to material properties and behavior, emphasizing the importance of where crystallographic variations occur.

3.2 Role of Local Heterogeneity through magnetic transition

After establishing a comprehensive understanding of the material structure through Dark-Field X-ray Microscopy (DFXM) imaging at room temperature, the focus was shifted to investigating the magnetic transitions and potential magnetostructural behavior of $NaMnO_2$ at low temperatures, specifically at 45 K and 22 K. The hypothesized triclinic nanodomains are reported to occur below the magnetic ordering temperature of 45 K, with an additional commensurate magnetic transition existing at 22 K [2, 12]. In this proof-of-principle work, efforts were primarily focused on the transition at 45 K, for which magneto-structural effects are likely to be less subtle. Given the minimal variation in room temperature results, it is expected that the results of the low-temperature experiment detailed below, performed on an arbitrary spot on the sample, are representative of properties of $NaMnO_2$ in general. The single crystal sample used for this experiment was cleaved from the center of the bulk sample surveyed at room temperature (see Section 3.1), with dimensions of approximately 6 $mm \times 2\ mm \times 0.1\ mm$. Working with a freshly cleaved sample ensured a clean and flat surface for measurement.

3.2.1 Low Temperature DFXM Setup at 6 ID-C

To enable low-temperature in-situ DFXM measurements, a custom-modified commercial low-vibration closed-cycle helium refrigerator (Montana Instruments, model s100) was employed at the 6-ID-C beamline of the Advanced Photon Source (APS) (see Figure 3.5). This cryostat provided several key features: (i) a set of optical view ports for a complementary VMU, mentioned above, focused on the sample's region of interest (ROI); (ii) 12.5 mm tall beryllium windows on either side to allow for the passage of X-rays

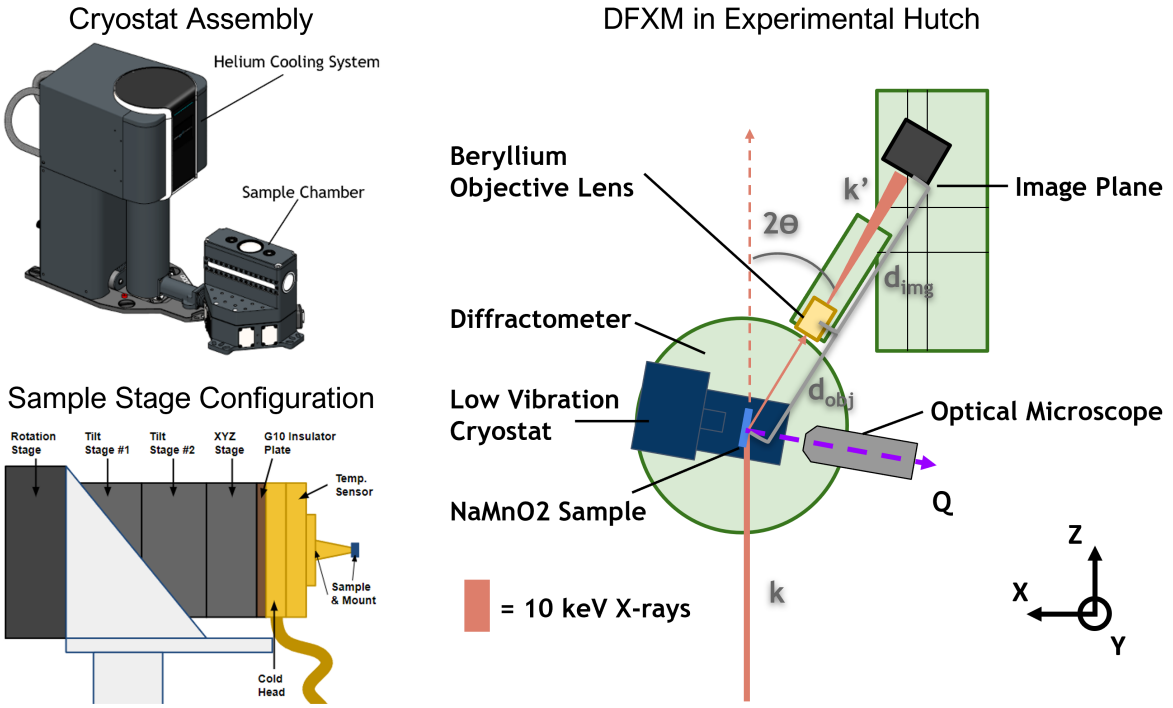

Figure 3.5: Schematic of the Dark-Field X-ray Microscopy (DFXM) set-up (right) with a low-vibration cryostat (upper left) equipped with a cryogenic sample tower (lower left). The sample is mounted to an integrated highly efficient, custom thermal link (shown in gold). Thermal mounting stages are attached to a cryogenic sample tower consisting of tip-tilt, translation, and rotation stages with nanoscale precision.

at angles of incidence up to 55° and scattering angles up to 110°; (iii) low-vibration (on the order of tens of nanometers) platform mounting; (iv) a base temperature of $<$ 3.5 K; and (v) a sample chamber sufficiently large to house a series of nano-positioning stages and goniometer. The cryostat was mounted on top of a diffractometer, using a vibration-damped optical breadboard, which is capable of sample translations in three independent directions and a rotation around the vertical axis ('rock', denoted here as θ) with an orthogonal circle segment ('roll', denoted here as χ), providing a horizontal scattering geometry (see Figure 3.5). The rotational resolution of the diffractometer is 0.0001° with a sample translation resolution, aided by optical encoders, of approximately 100 nm.

For the low temperature experiment, the Be compound refractive lens (CRL) previously used as a condensing lens, was operated as an objective. The CRL produced a large field of view (FoV) and consisted of 24 individual lenses, combined to achieve a focal length of 320 mm (10 keV) and a sample to objective distance (d_{obj}) of 368.5 mm. The lens parameters result in an X-ray magnification of 7.6× at the image plane (d_{img}), 2.8 m away from the sample. The CRL had an effective aperture of 300 μm, which again results in a theoretical diffraction limited resolution of $\approx$ 100 nm.

This experiment used 10 keV X-rays, with a resulting penetration depth of about 6 μm. In reflection geometry, this implies probing approximately 3 μm into the sample. After cooling the sample to the base temperature of the low-vibration cryostat (3.2 K), below both magnetic transitions of interest, the original position on the sample was relocated using the optical VMU with a 10x objective. Room temperature reference images were compared to images taken after cooling and through independent motor translations of the optical microscope, which were then replicated by motor translations of the sample, the illumination spot was repositioned accurately. A shallow depth-of-field (10 μm) combined with the high-resolution (345 nm per pixel) of the optical microscope, a similar scale as the DFXM images, provides confidence that sample position was maintained during temperature-dependent measurements. While no condensing apparatus was used in this experiment, a 500 × 300 μm^2 box beam was controlled with a two-dimensional X-ray window (horizontal and vertical slit pairs), before impinging on the sample inside the crysostat.

DFXM images of maximum intensity across Rocking Curve Imaging (RCI) scans taken at room and base temperature were assessed for feature resolution. Vertical line scans or intensity cuts through the images were used to evaluate the width of the feature boundaries. The width of a given boundary was determined by taking the derivative of the line profile and subsequently fitting its peak with a Gaussian curve. The width

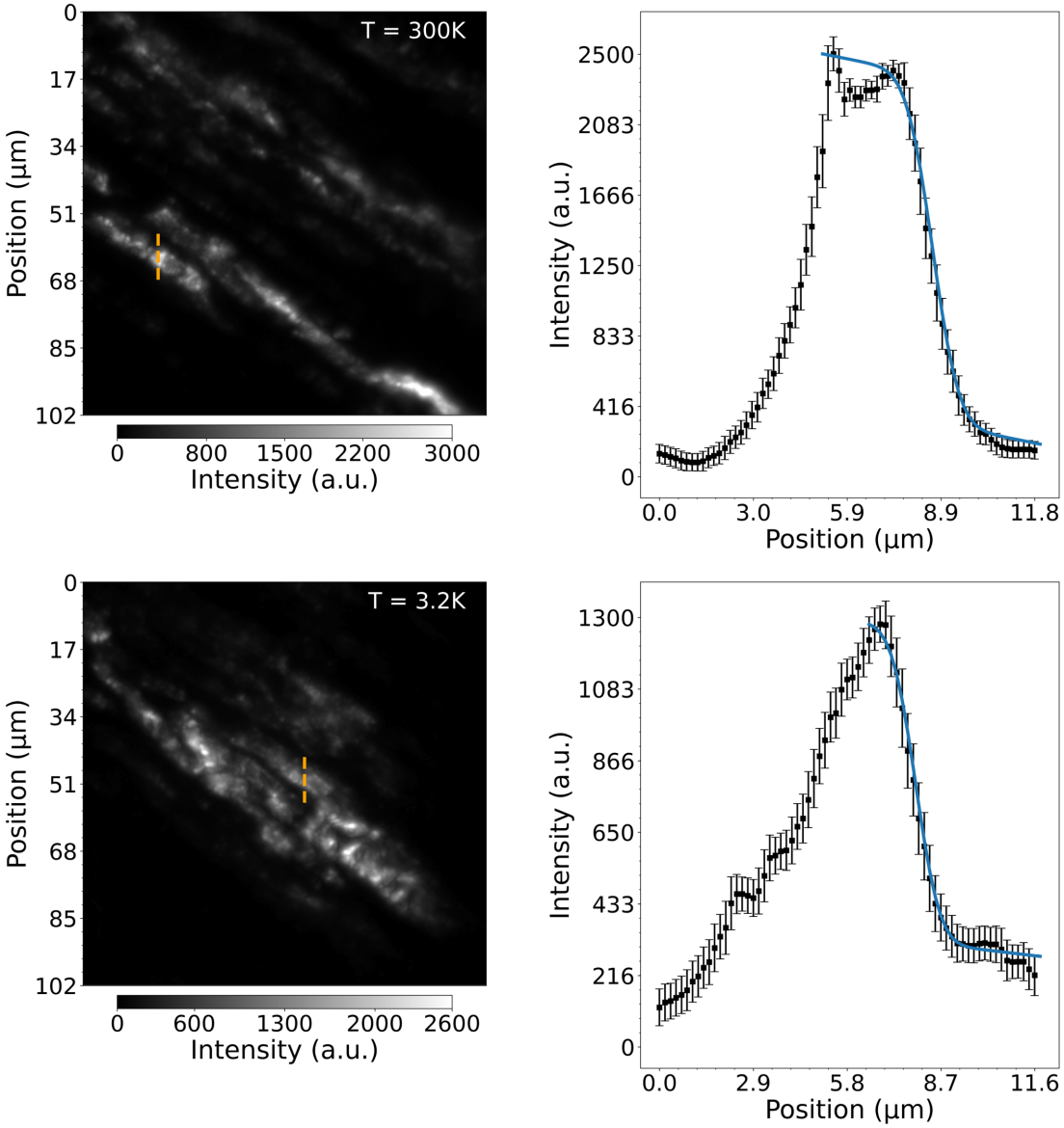

Figure 3.6: Diffraction contrast images (left) taken at room temperature (top) and base temperature (bottom) using the Be compound refractive lens (CRL) objective. Orange dotted lines indicate where the line profiles (right) were taken for each image. Gaussian fits to the peaks of the line profile derivatives, which were used to calculate boundary size, are overlaid on the intensity curves. In this case, images across the full range of temperatures displayed a boundary resolution of $\sim$1 μm or $\sim$6 pixels.

(FWHM) of the fit curve gives a good estimate of the contrast boundary size. As shown in Figure 3.6, the results indicate that cooling did not affect the resolution of the technique,

and the optical configuration of this experiment enables micron-scale feature resolution at all intermediate temperatures (3.2-300 K). The emphasized features had calculated widths of 1.6 μm and 1.5 μm for the 300 K and 3.2 K images respectively.

3.2.2 Low-Temperature Results

After conducting a baseline RCI scan of $NaMnO_2$ at room temperature, the sample was cooled to the base temperature of 3.2 K. A series of RCI scans were then carried out at various temperatures from 3.2 K through low-temperature transitions to detect any local changes in strain and/or orientation due to a purported structural transition at 45 K. The two-theta values corresponding to maximum peak intensity of each scan were recorded and related back to d-spacing of the $(2, 0, \overline{2})$ peak through Bragg's Law. Evaluation of the d-spacing allowed the lattice parameters of the material to be estimated across the temperature range, as plotted in Figure 3.7. No significant change in the two-theta position was observed until above 120 K. After which, the increase in lattice parameter is likely due to the coefficient of thermal expansion, increasing linearly as the sample is warmed back up to room temperature. The lack of a significant shift or discontinuity in the two-theta position at 45 K, indicates that the structural transition is subtle (as expected) and not clearly observable through bulk averaged measurements, underscoring the importance of techniques like DFXM for resolving local changes.

The raw RCI scan images were also analyzed to generate mosaic and FWHM images of the sample at the various temperatures. Mosaic and FWHM images collected before (9 K), between (38 K), and after (52 K) the two transition temperatures, are displayed in Figure 3.8. There is a notable (-θ) shift in the orientation of several regions as the sample is heated from 9 K to 52 K, indicating that the transition impacts the mosaic spread of the material at a local level, possibly causing an average broadening of the $(2, 0, \overline{2})$ peak. At

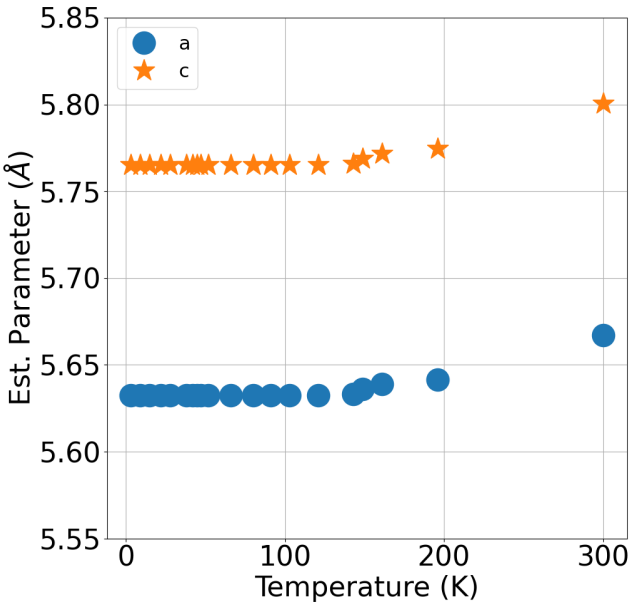

Figure 3.7: Estimate of $NaMnO_2$'s lattice parameters, a and c, with respect to sample temperature. These values are based on the 2θ angle of the diffracted beam for each Rocking Curve Imaging (RCI) scan.

base temperature, unlike the observations at room temperature, a separation of mosaic boundaries can be detected. The majority of the scanned area displays a relatively negative tilt, indicated by a blue coloring, interspersed with smaller, equiaxed regions of positive tilt, indicated by a red coloring in the mosaic images. Additionally, a nominal positively tilted (red) linear domain can be observed. The red domain begins near the top of the scanned area and follows the slanted linear boundaries, with junctions that cross vertically through the domains towards the bottom of the image. This red domain is highly reminiscent of a stacking fault structure, which appears to distort the primary phase through subtle rotation of the lattice.

Examining the FWHM images at base temperature, relatively sharp ($\sim 0.02^\circ$ width) domains are seen, consistent with the high crystallinity of the sample. Several peak broadened boundaries are also observed, separating the smaller orthogonal domains and

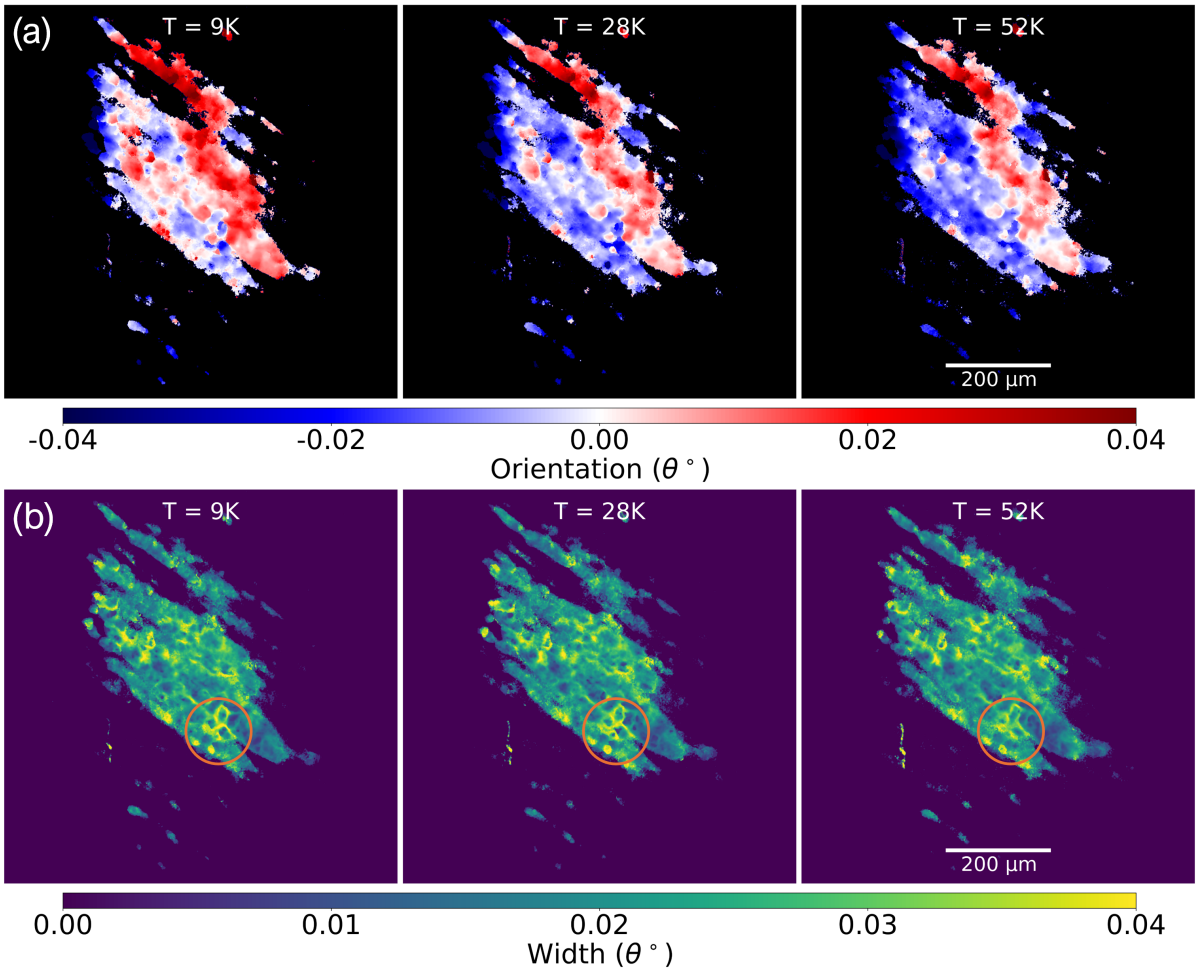

Figure 3.8: Evolution of (a) mosaic images and (b) width images through sample heating from 9 K to 52 K, generated from DFXM images taken during rocking curve scans. An orange circle has been drawn in the same location of each full-width-at-half–maximum (FWHM) image to highlight local changes to the microstructure through the transition temperatures.

surrounding the globular mosaic domains. Interestingly, the FWHM values do not show a drastic increase between linear domains, suggesting these boundaries are not disordered but rather represent physical cracks (*i.e.*, lack of material) through the illuminated volume. Although the circular loops of increased width resemble dislocation loops that are linear defects, their length scale is more consistent with dislocation pileup or other planar defects. In Figure 3.8, an area highlighted by an orange circle displays three of

these loops, which can be seen coalescing at a single point. The corresponding regions on the mosaic map show a drastic flipping of mosaic character (sudden shift from red to blue and vice versa) across the boundary lines. Other domain boundaries in the FWHM maps do not consistently correspond to these same features, indicating a complex texture in the material.

Interestingly, most of the qualitative changes in heterogeneity occur after the 22 K transition, while heating the sample through the 45 K transition has less of an effect on the observed parameters. Notably, the highlighted area of increased activity is located on the boundary between the nominal mosaic domains, suggesting that any formation of triclinic nano-domains are likely to occur near faulted regions or rotational boundaries of the material sample. The observed local changes do not appear to affect the average mosaic and FWHM of the DFXM images, which is in agreement with previous X-ray Diffraction (XRD) results.

To make these observations more quantitative, temperature-dependent measurements focused on this transition, were taken by holding θ fixed at the peak value and capturing images at a constant rate as the sample was slowly heated from 10 K to 52 K. The total intensity of the images was calculated and plotted against temperature in Figure 3.9. A logistic curve fit to the data is overlaid and shows a significant jump (20% increase) in the intensity of the total $(2, 0, \overline{2})$ peak, centered on 44 K, spanning over a temperature range of $\approx$10 K. It is intriguing that while certain regions are significantly affected through the transition, the rest of the FoV remained quiescent. The regions outlined by boxes undergo an overall 55% and 25% increase through the transition for the first and second ROIs respectively.

The magnified images show subtle changes in various features as the sample is heated through the transition, but it remains difficult to say whether these changes are direct observations of nanoscale triclinic domains undergoing a transition to the primary mon-

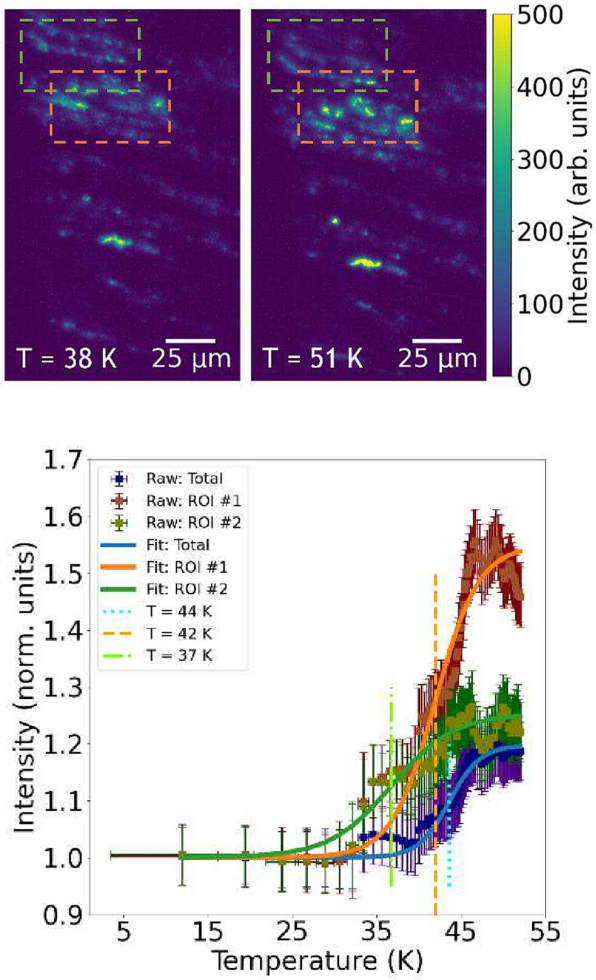

Figure 3.9: Dark-Field X-ray Microscopy (DFXM) images taken while holding the sample orientation constant and at the maximum intensity for two temperatures, one before (a) and one after (b) the transition temperature of 45 K. Orange and green dashed boxes indicate regions of interest (ROIs) that were selected for comparison. Intensity values are plotted in (c) against temperature for the primary $(2, 0, \overline{2})$ peak, computed for the total image and for the ROIs displayed in blue, orange and green respectively. The data includes error bars for both temperature and intensity fluctuations. The transition resulted in a 20%, 55% and 25% increase in the overall and regional intensities, and inflection points at 44, 42 and 37 K respectively.

oclinic phase. These effects may also be an example of a magnetoelastic coupling, which results in structural strain or rotation due to the magnetic transition. Additionally, the Mn_3O_4 intergrowth, mentioned above, exhibits a ferrimagnetic transition at 43 K [64], resulting in a weak ferromagnetism at low temperatures. When coupled to the α-$NaMnO_2$

structure, the transition occurs closer to 41 K [2]. It is suspected that the intergrowth forms in stacking fault regions or along planar defect boundaries. Thus, the transition from a paramagnetic to ferrimagnetic ground state could result in magnetostriction of the $NaMnO_2$ lattice, causing certain regions to 'fall off' the primary Bragg-peak. While previous studies of this transition have measured powders, the spatially resolved images collected using DFXM on a single crystal sample give the first visual indication of local heterogeneities playing a significant role in the magneto-structural transitions at low temperatures.

3.3 Peak Splitting and Friedel Pair Study

The coherent twins that form in $NaMnO_2$ are symmetrically related and essentially swap their crystallographic a and c directions. This twinning occurs about the (2, 0, $\overline{1}$) plane, making the difference in lattice parameters between a and c unobservable in the magnitude of the $(2, 0, \overline{2})$ reciprocal lattice vector. Consequently, the signal variation between twin variants is not resolvable in the Dark-Field X-ray Microscopy (DFXM) images of this peak. To investigate variation and spatial distribution of twin domains, a DFXM experiment on $NaMnO_2$'s split peaks was conducted. This was achieved by imaging the $(2, 0, 0)$ and $(0, 0, \overline{2})$ Bragg peaks, which split in reciprocal space because of the differing lattice parameters. Because twinning in $NaMnO_2$ flips the relative direction of these HKL peaks, the reciprocal space position where the $(2, 0, 0)$ peak is expected, a slightly offset $(0, 0, \overline{2})$ peak from the twin variant will also appear when regions with both twin orientations are illuminated simultaneously.

This DFXM study aimed to investigate the peak splitting locally and combine it with a study of Friedel Pairs for each peak. Friedel's law states that for every Bragg peak in reciprocal space, there is an equal Bragg peak in the opposite direction due to the basic

symmetry of the periodic lattice. This condition is satisfied only if there are no energy absorption effects (*i.e.*, elastic scattering) during diffraction and will theoretically result in the two peaks demonstrating the same intensity. A set of Friedel Pairs were imaged using DFXM to see if this phenomenon could be demonstrated spatially with this experimental methodology. The same sample studied in the low-temperature investigation discussed in section 3.2 was evaluated during this study.

3.3.1 DFXM Setup at 33-ID-D

This DFXM experiment was performed at the 33-ID-D experimental station of the Advanced Photon Source (APS), with a considerably different configuration than that of 6-ID-C, although the fundamental aspects of the technique were maintained. The DFXM setup at 33-ID-D nominally followed the setup outlined in Choi *et al.* [65], utilizing a DCM to tune the incident X-ray energy to 10 keV. A pair of one-dimensional KB mirrors were used for beam focusing in the horizontal and vertical directions, resulting in an incident spot size of approximately $20 \times 20\ \mu m$. Illumination from the focused X-ray beam diffracts in reflection mode from the $NaMnO_2$ sample, which was mounted on a hexapod stage used for translation and rotation manipulation. The hexapod stage is a motorized device with six independently moving legs that can reproduce precise translations in X, Y and Z directions, and two rotations (θ and ϕ) about the X and Y axes respectively (see Figure 3.10). Imposing a ϕ rotation of 180° facilitated the imaging of Friedel Pairs without the detector being moved significantly.

Once the X-rays are scattered they pass through a zone plate, made of Au deposited on SiN, which acts as an objective. The working distance of the zone plate was approximately $50\ mm$. A Si Pilatus-II 100K X-ray detector is initially employed in the diffracted beam's path to locate and optimize the peak of interest. Once the center and extent of the Bragg

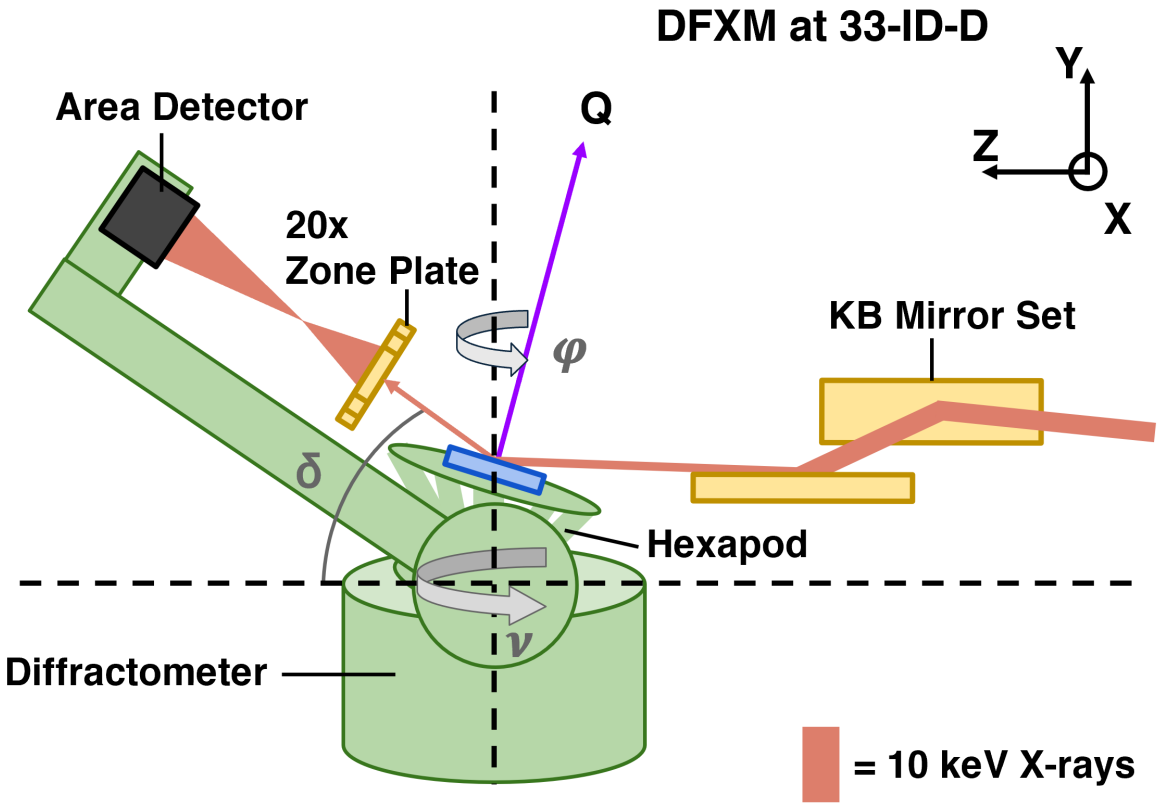

Figure 3.10: Schematic of the Dark-Field X-ray Microscopy (DFXM) setup at the 33-ID-D experimental station. DFXM experiments conducted using this setup were performed in reflection geometry with a nominally vertical scattering plane. The diffractometer and sample stage configuration enabled two axes of rotation for the sample and detector independently (2S2D). Rotation about the x and y axes for the sample are denoted θ and ϕ respectively, while the same rotations for the detector are denoted δ and ν respectively.

peak is found, the magnified diffraction signal can be captured on an area detector placed at the image plane. Magnified images were collected using a Andor's Neo area detector, which is designed similarly to the previously described Zyla detector (see Section 3.1.1), including a scintillator followed by a reflective mirror that passes light through an optical objective before being collected by a CMOS. In contrast to the Zyla detector, the Neo contains 2 exchangeable optical objectives with 2× and 20× magnification factor options. The Neo detector's native pixel size of 6.5 μm coupled to the combined magnification of

400×, resulted in an effective pixel size of 16.25 nanometers across the 2048 × 2048 pixel field-of-view (FoV).

The DFXM setup at 33-ID-D operated in a nominally vertical scattering geometry with the area detector mounted directly to the δ arm of the diffractometer. The diffractometer provided the same rotational capabilities as the sample to the detector, with rotation about the x-axis denoted δ and rotation about the y-axis denoted ϕ. The combination of 2-axes of rotation for the sample and 2-axes of rotation for the detector (2S2D) enabled the complex scattering geometry necessary for imaging the $(2, 0, 0)$ and $(0, 0, \overline{2})$ Bragg peaks from each twin variant. The vertical scattering geometry also implies that peak spreading for this experiment occurs mostly in the orthogonal direction of the spreading in the experiments performed at 6-ID-C, resulting in an effective vertical pixel size of 65.8 nm across the image horizontal.

3.3.2 Split Peak Results

Using the 2× optical objective, the centroids for the first set of split peaks were located, belonging to the $(2, 0, 0)$ Bragg peak of one twin variant, and the $(0, 0, \overline{2})$ Bragg peak of the second, denoted from this point on as $(2, 0, 0)_{t1}$ and $(0, 0, \overline{2})_{t2}$, respectively. The $(2, 0, 0)_{t1}$ peak was found at $\delta = 13.85°$ and $\nu = 24.04°$, while the $(0, 0, \overline{2})_{t2}$ peak was found at $\delta = 12.65°$ and $\nu = 23.89°$. The total Bragg angle that resulted from the combination of δ and ν rotations was determined by applying two corresponding rotation matrices, about X and Y respectively, to a unit vector along the horizontal, or Z direction (see Figure 3.10). The angle between the starting and final vectors was then calculated, using the dot product, to be 26.86° for the $(0, 0, \overline{2})_{t2}$ peak and 27.54° for the $(2, 0, 0)_{t1}$ peak.

The 20× optical objective was used to image each of these peaks and the resulting

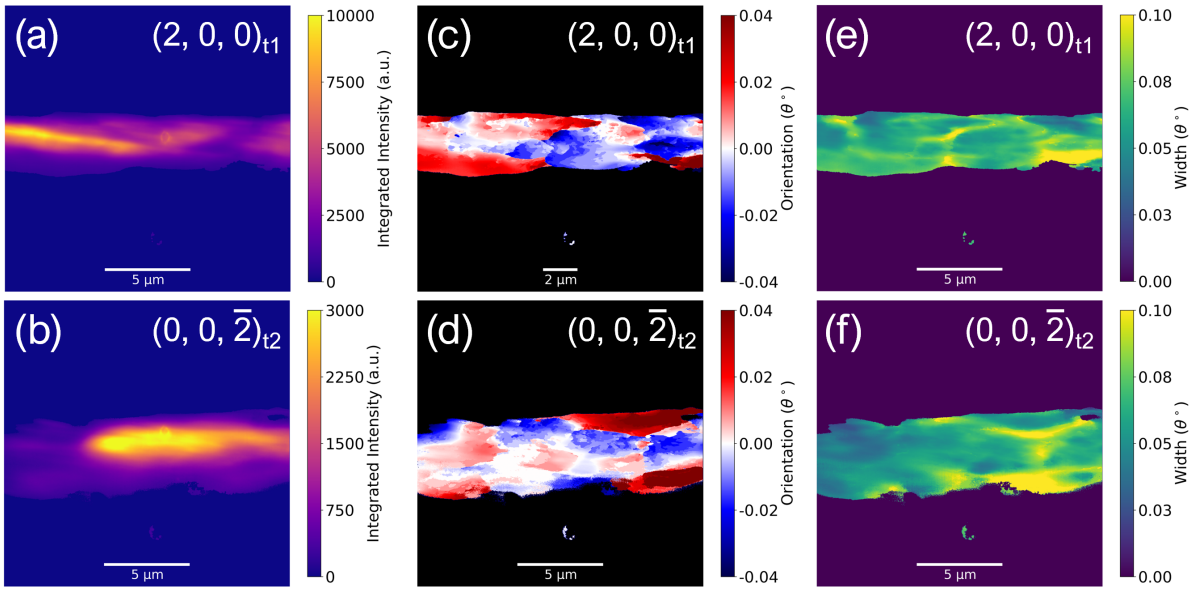

Figure 3.11: Series of Dark-Field X-ray Microscopy (DFXM) images of twinned Bragg peaks that are split in Q space due to a slight difference in a and c lattice parameter in α-$NaMnO_2$'s monoclinic structure. Images of integrated intensity (a,b), mosaic (c,d) and full width at half maximum (FWHM) (e,f) are shown for comparison between the diffraction signal of the primary and secondary twin domains, denoted t1 and t2 respectively. Signatures from all three image-types qualitatively show coordination between the two twin domains and reflect the complexity of their interface.

DFXM images are displayed in Figure 3.11. The non-zero intensity from both peaks, observed across the scanned area, is the first indication that both twin variants are present within the illuminated volume, which spans 20 μm horizontally, 120 μm vertically, and 3 μm into the sample. Examining the spatially resolved images of integrated intensity (Figure 3.11(a,b)), the centroids of the diffracting X-rays complement each other; bright regions of one peak correspond to dim regions of the other, and vice versa. This provides evidence that the same portion of the sample is being imaged, with the resulting image contrast originating from structural changes present in the selected twin domain.

Images of mosaic (Figure 3.11(c,d)) and FWHM (Figure 3.11(e,f)) of each twin peak are also shown. Local mosaic domains exhibiting similar morphology, but opposite character, are revealed. Where one twin domain exhibits a negative tilting, the other exhibits

a positive one, demonstrating the orientation inversion of the twinned crystallites. Subregions with mixed character in the mosaic images of both peaks can also be observed. Displayed as white regions accompanied by lighter shades of red and blue, these mixed areas likely correspond to the boundary between the twinned domains. Similar results are seen in the FWHM values, as brighter regions in one peak corresponded to dimmer regions in the other, with some areas presenting similarly for both peaks. These results suggest a complex interaction between the twin variants, with each crystal domain hosting shared and distinct defect structures across their spatial distributions.

Although more analysis is needed to fully correlate the two twin variants, this initial result presents a promising potential for investigating complex materials that exhibit splitting in their diffraction pattern, using DFXM. It provides a clear example of DFXM's ability to discriminate between diffraction signals that stem from the same crystallographic domain and signals that originate from spatially segregated domains.

3.3.3 Friedel Pair Results

To image the set of split Friedel Pairs, the sample was rotated 180° (from $\phi \approx 10°$ to $\phi \approx -170°$. The symmetric pair of Bragg peaks were $(\overline{2}, 0, 0)_{t1}$ and $(0, 0, 2)_{t2}$, corresponding to each twin variant respectively. The rotation of the sample allowed the Friedel Pairs to be imaged without changing the detector's position significantly. The $(\overline{2}, 0, 0)_{t1}$ and $(0, 0, 2)_{t2}$ peaks were found at $\delta = 15.095°$ and $\nu = 23.26°$ and $\delta = 14°$ and $\nu = 23.14°$, resulting in total Bragg angles of 27.48 ° and 26.85°, respectively. The good agreement between the Bragg angles of Friedel Pairs supports the accuracy of the sample's defined orientation matrix during the experiment.

However, compared to the puzzle-piece like coordination of the split peaks, the images of the Friedel Pairs are significantly different from one another. Integrated intensity

curves and images of maximum intensity over the Rocking Curve Imaging (RCI) scans of the symmetric peaks are shown in Figure 3.12. It's important to note that during the experiment, rocking θ using the hexapod, did not yield the expected variation in the diffraction peak, while rocking through small variations in ϕ did. Therefore, RCI scans of the $(2,0,0)_{t1}$, $(0,0,\overline{2})_{t2}$, $(\overline{2},0,0)_{t1}$, and $(0,0,2)_{t2}$ peaks were all conducted by rocking phi. Without fiducial markings, it is challenging to determine if the same portion of the sample is being illuminated after rotation. Given that the hexapod's rotation might not be perfectly normal, some minor translational shifts likely occurred, resulting in the X-ray spot illuminating a different region of the sample volume. This is further evidenced by the spatial disparity between the maximum intensity images of each Friedel Pair. The significant difference in amplitude of the integrated intensity curves are therefore assumed to stem from a positional shift rather than being indicative of any inelastic scattering components. Although the absolute intensities between each Friedel Pair is disparate, their FWHMs were of the same order ($\sim$0.06). Comparison of the intensity ratio between the split peaks from either set of Friedel Pairs demonstrated better agreement. The ratio of the brighter of the split peaks was 5.22, while the intensity ratio of set of peaks was 4.16. Further work is needed to fully understand these results.

These results illustrate the difficulty in aligning the rotational axes of the various mechanical stages employed in this technique. As efforts continue to push the resolution of DFXM measurements towards the diffraction limit, special care must be taken in the configuration of the various manipulation stages. This obstacle is particularly relevant for efforts to combining DFXM with Diffraction Contrast Tomography (DCT). DCT involves recording a diffraction peak across several rotational steps about the momentum vector Q, allowing for a three-dimensional reconstruction of the diffracted volume, similar to X-ray Computed Tomography (XCT). The reconstruction provides information about grain morphology and subgrain distributions. A DCT methodology could theoretical be

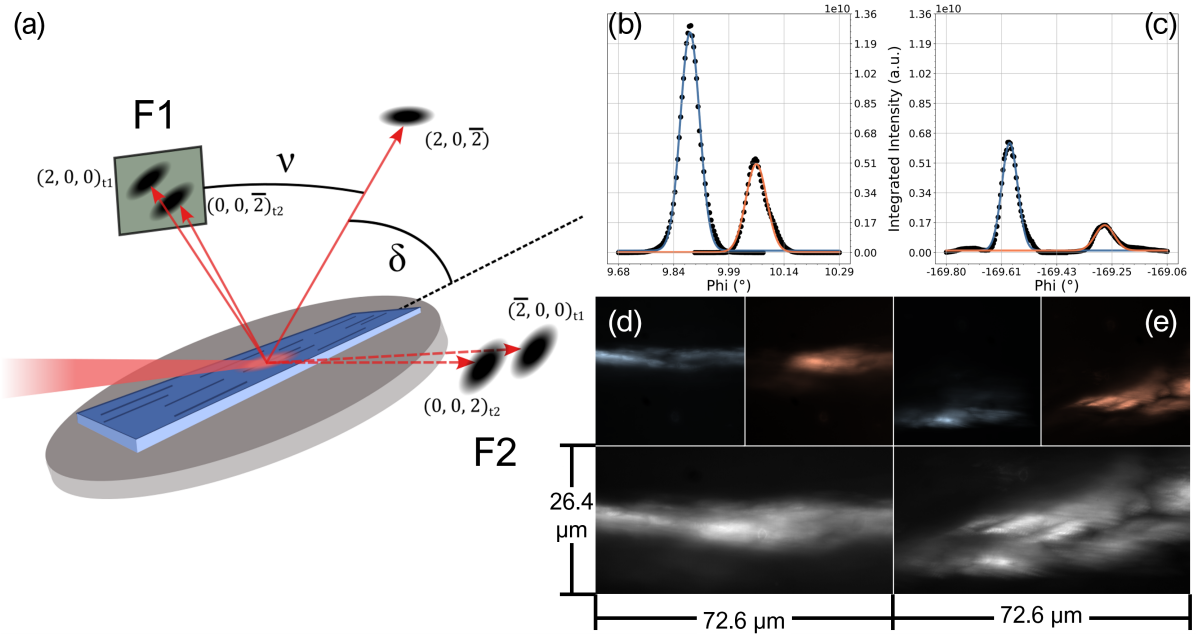

Figure 3.12: (a) Schematic of the Dark-Field X-ray Microscopy (DFXM) scattering geometry that enabled imaging of twinned split peaks and their symmetric counterparts (Friedel Pairs), using the two-axis rotation capabilities of the detector arm configuration and a 180° rotation of the sample. Leveraging this geometry, images of four distinct Bragg peaks were collected at nearly the same detector location. Intensity curves through rocking scans are presented for each set of Friedel Pairs, F1 (b) and F2 (c), for comparison. DFXM images of the component split peaks and their resultant superposition are also shown for F1 (d) and F2 (e).

enhanced with an objective to increase the technique's spatial resolution, however many challenges still remain for the feasibility of this kind of study.

3.4 Residual Strain Investigation

Using the same Dark-Field X-ray Microscopy (DFXM) setup at 33-ID-D, a theta-two-theta scan was also performed on the $(2, 0, \overline{2})$ Bragg peak to assess the impact of strain on $NaMnO_2$. This methodology, previously described in an earlier section, was applied to the same thin sample of $NaMnO_2$ cut from the original bulk crystal. θ varied Rocking Curve Imaging (RCI) scans were collected across various Bragg angles, while rotationally

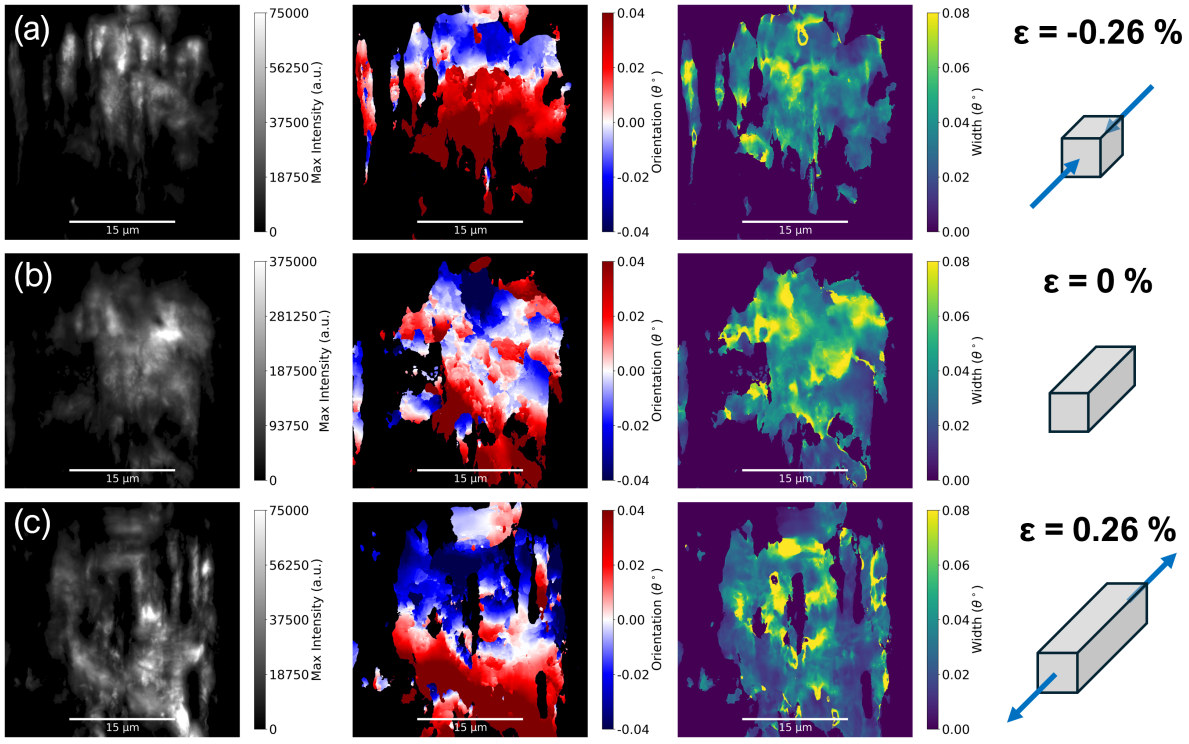

Figure 3.13: Strain evolution of $NaMnO_2$'s microstructure shown via Dark-Field X-ray Microscopy (DFXM) images for a compressive state (a), an unstrained state (b) and a tensioned state (c). Each strain state displays from left to right, a maximum intensity image, mosaic image and full-width-at-half-maximum (FWHM) image for qualitative comparison. DFXM images were collected at the same sample location but with varied diffraction angles, 2θ, and corresponding axial strains, ϵ.

stepping the central θ value at half the step size of nominal Bragg angle. In this way, the effective magnitude and rotation of Q was varied through DFXM imaging, producing a large data set that spans two-dimensions through reciprocal space. The evaluated length of Q can be related back to the axial d-spacing using Bragg's Law, providing an estimate of the strain in the Q- direction. Although many differing strain-valued images were collected, the relative strain values of $\pm 0.26\%$ (associated with tensile and compressive strains, respectively) are presented in Figure 3.13.

Notably, the overall intensity of the DFXM images drop by roughly a factor of five at both the compressive and tensile ends of this strain regime. Additionally, the centroid of

illumination appears to shift along the b-direction (vertically), although this observation remains qualitative and requires further work to determine whether this behavior is indicative of bulk material response.

In DFXM, the projection of the diffraction signal onto the detector results in a reduction in dimensionality—from the three-dimensional volume producing the diffraction signal to the two-dimensional image plane. This geometric limitation causes a loss of depth resolution along the projection vector. Unfortunately, this loss of resolving power is coupled to the advantage of using penetrative high-energy X-rays; when the energy is increased to achieve a deeper probe into the material sample, more of the diffraction signal is combined along the projection vector, which ultimately limits the feature resolution of the technique. This makes it challenging to determine how the differences in character between regions with varied strains may be connected through the out-of-plane direction, which corresponds to the twin plane layers for the $(2, 0, \overline{2})$ Bragg peak of $NaMnO_2$.

In the nominally zero-strain state (the d-spacing that produces the brightest integrated intensity), mosaic regions shows a gradual transition between tilting directions (red to white to blue). In contrast, images of the compressed and tensioned strain states display steeper boundaries between mosaic regions. Each strain state also displays characteristically similar FWHM patterns that are spatially different from one another. The physical meaning of these observations are currently unclear and require further investigation. Overall, these initial results illustrate the complexity and challenges associated with analyzing the effects of strain in this material and highlight areas for further study.

Chapter 4

Follow-Up Defect Study: $NaMnO_2$

4.1 Far-Field HEDM with X-ray CT

The thorough Dark-Field X-ray Microscopy (DFXM) studies of $NaMnO_2$ revealed significant local heterogeneity within the defect-heavy material. There remains a challenge in determining exactly which defects contribute to the DFXM contrast observed in the various images. The combination of rich information provided by DFXM—reciprocal space data from X-ray diffraction and real-space data from the objective lens—creates ambiguity in the collected images, making it difficult to pinpoint the sources of various features. Particularly, the investigation into the low temperature transitions (22 K and 45 K) and the potential formation of triclinic nano-domains in $NaMnO_2$ observed nanoscale changes to the crystal structure. However, it remains unclear whether these are actual transformations to triclinic domains or if they result from the magnetic transition of Mn_3O_4 intergrowths that cause local strain.

To better understand the data from the DFXM measurements, a combination of microscale X-ray Computed Tomography (CT) and far-field High-Energy Diffraction Microscopy (HEDM) were performed to further elucidate $NaMnO_2$'s structure. X-ray CT

involves illuminating a semi-transparent material sample with X-rays and capturing the transmitted beam in a bright-field configuration with an X-ray area detector. The collected images show contrast from the varying absorption of X-rays through the material. Essentially, a picture of the X-ray shadow (radiography) cast by the sample is taken. Images are captured in this way as the sample is rotated 360° about a vertical axis perpendicular to the incident X-ray beam. These images are used to create a three-dimensional reconstruction of the scanned volume with a resolution on the order of μm.

HEDM uses monochromatic X-rays to illuminate a sample in the same transmission geometry. The diffraction pattern is then collected on an area detector. The sample is rotated 180° (making use of Friedel's Law) about an orthogonal axis, while images are collected at the various sample orientations. This technique has two modes that depend on the distance at which the area detector is placed: "near-field" and "far-field". The "far-field" modality was employed to study $NaMnO_2$ by placing a larger area detector on the order of meters away from the sample and capturing the resulting Bragg peaks across a series of HKL rings. In placing the detector at this distance, the diffracted intensities specific angles become more spatially resolvable. The material-dependent physics of diffraction enables the relative centroids, average orientations and average elastic strains of the illuminated crystal domains to be calculated from the diffraction pattern. In contrast, the "near-field" mode utilizes a smaller area detector placed millimeters from the sample to measure individual diffraction peaks with a higher spatial resolution. In this configuration, diffraction information can be leveraged to measure low-angle domain boundaries and characterize grain morphology.

Combining X-ray CT and far-field HEDM produces a real-space reconstruction of the sample's microstructure, with coordinated information about the crystallographic domains distributed therein. These experiments are often used to investigate the spatial distribution of many different grains within a polycrystalline material. In this case,

the measurements investigated the spatial distribution of β-$NaMnO_2$ and Mn_3O_4 intergrowths within a single-crystal of α-$NaMnO_2$. The collected data also contains information about the average orientation and average residual strain of the various domain structures, which is relevant for characterizing their formation mechanisms.

4.2 Experimental Setup at 1 ID-E

The combined X-ray CT and far-field HEDM experiment on $NaMnO_2$ was conducted at the 1-ID-E beamline of the Advanced Photon Source. The sample was encapsulated in a beryllium hat, back-filled with helium, to prevent degradation in air while allowing transmission of the X-rays. This experiment was performed on the same single-crystal sample (thinner of the two) of $NaMnO_2$ as the low temperature and Friedel Pair studies. Monochromatic X-rays of 71.676 keV ($\lambda = 0.173$ Å) with an energy resolution of $\pm$ 2.5 eV were selected by a bent double-Laue monochromator [66]. The incident beam shape was controlled with $\sim \mu m$ precision using a high-quality polished tantalum based slit assembly placed in the beam's path.

The X-ray CT scans were performed using an X-ray box beam approximately 2.1 mm wide $\times$ 1 mm tall. The sample was rotated about the vertical (Y) axis in 0.25° steps and translated vertically to collected a series of scans across the sample's volume. The vertical raster was organized to include a 0.1 mm overlap between layers to simplify their eventual stitching together to recreate the total illuminated volume. Tomographic images were captured with an in-house developed detector composed of a 25 μm thick LuAG:Ce single crystal scintillator, a 45° mirror, a Mitutoyo 5X optical, infinity corrected, long-working distance microscope objective, and a PointGrey Grasshopper3 CMOS camera with 5.86um pixel size and a 1920x1200 pixel field of view (FoV). The resulting effective pixel size is 1.172 μm, which is also used as the voxel resolution for the resulting three-

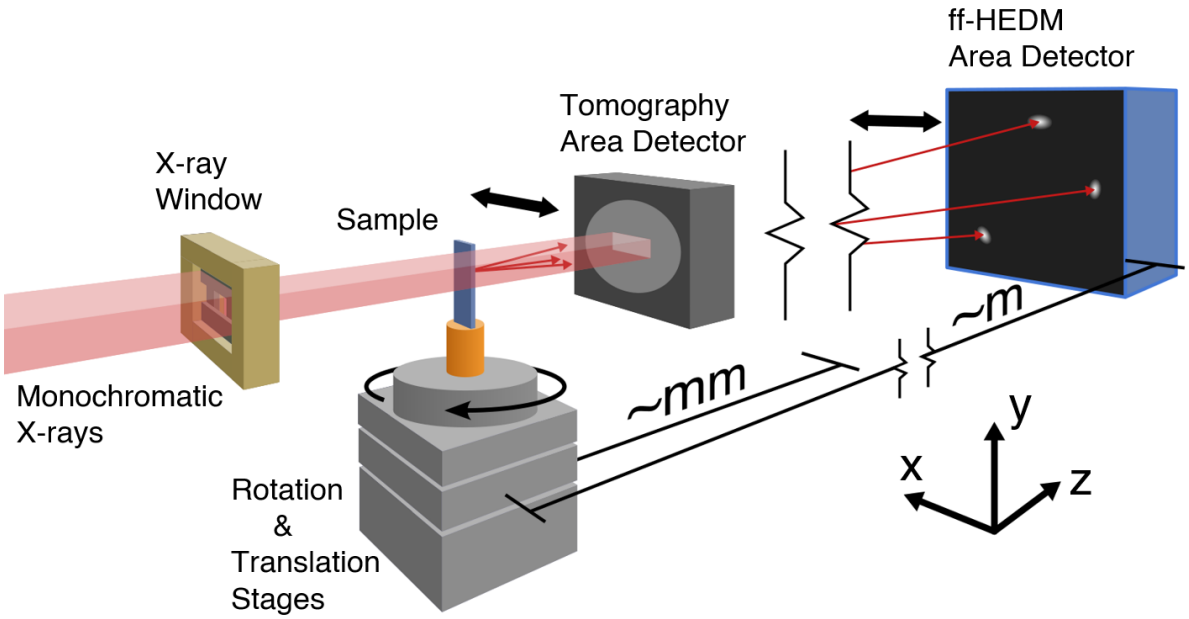

Figure 4.1: Schematic of the combined X-ray Computed Tomography (XCT) and far-field High-Energy Diffraction Microscopy (HEDM) experimental setup employed to measure defects in $NaMnO_2$. Primary components of the setup are labeled and the X-ray path is displayed with red hues. The transmission geometry of the setup includes the absorption profile (box beam) captured by the tomography detector and the diffraction peaks (red arrows) captured by the area detector. Arrows are also drawn to indicate the lateral movement of each detector, which enables in-situ mode switching between XCT and HEDM measurements.

dimensional reconstructions. More detailed information on X-ray CT methodologies and tomographic reconstruction is available in Refs. [67, 68].

Far-field HEDM measurements were performed in tandem using a high dynamic range Pilatus3 X 2M CdTe counting detector with 172 μm pixel size. The Pilatus detector had 20-bit full dynamic range, which was critical to capturing Bragg peak intensity from the weaker β phase (less than 1% by volume) or Mn_3O_4 intergrowths, while not saturating from the intensity of peaks from the primary α-phase. The measurements used a X-ray box beam that was 2.1 mm wide $\times$ 0.1 mm tall, with no overlap necessary. The rotational step size of 0.25° for a total 360° rotation was also used for the far-field measurements and the sample-to-detector distance was 738 mm. Before each set of far-field HEDM

scans, a calibration sample of CeO_2 mounted on top of the beryllium hat was moved into the incident beam and measured to enable a precise sample-to-detector distance to be calculated during post-processing.

4.3 X-ray CT Results

The X-ray CT results, presented in Figure 4.2, provide a detailed reconstruction of a 3D volume of the $NaMnO_2$ sample. Slices of the tomographic volume can be taken in arbitrary directions to assess the material's microstructure. It is important to note that the reconstruction process entails an intensity scale inversion, such that dark regions of the absorption images turn into bright regions in the final tomographic images. Similar to classic X-ray images of skeletal structures, the bones which absorb more X-rays than the surrounding tissue are visualized as white shapes on a black background. The primary feature of interest in the presented images is a fine highlighted structure that extends throughout the material's volume. Although cracks and fractures from the cleaving and mechanical cutting of the sample are visible, deeper into the material brighter lines also appear (see Figure 4.2). Due to the intensity inversion of the reconstruction, the increased brightness of these regions indicate an increased X-ray absorption.

High-energy X-rays easily penetrate elements with relatively low atomic numbers, such as the sodium and oxygen present in $NaMnO_2$. Therefore, manganese is primarily responsible for any absorption contrast observed in the resulting tomographic images. This suggests that the brighter lines indicate areas with an increased manganese density compared to the nominal material matrix. Despite being faint and partially obscured by tomographic reconstruction artifacts, these lines can be seen to form diagonal, cross-hatched patterns across the ab plane of the material. Examining a section cut along the cleavage plane, or $(1, 0\overline{1})$ plane, of the material (see Figure 4.2), these bright lines become

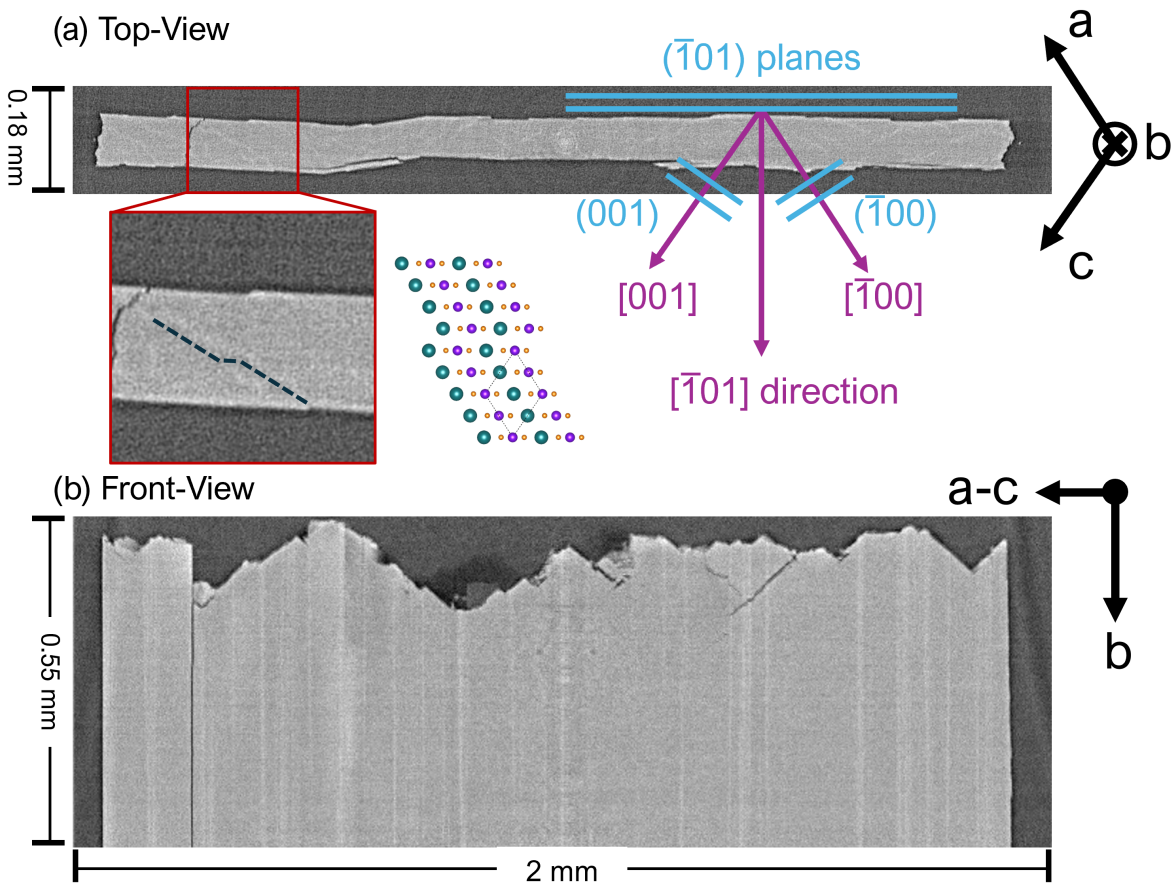

Figure 4.2: Image slices from the tomographic reconstruction of the $NaMnO_2$ sample displaying absorption contrast across the *ac* plane (a) and along the b direction (b). The known orientation of the single-crystal sample is denoted in black for each view, while the relevant crystallographic planes and directions are denoted in blue and purple respectively. Additionally, a digitally magnified region of the top view is outlined in red and overlaid with a dashed line to guide the reader's eye to subtle stacking-fault-like features.

more visible and can be seen extending vertically along the *b*-direction throughout the entire sample. Although faint, the diagonal lines in the *ab* plane are clearly angular and appear to form along the $(1, 00)$ and $(0, 0, \bar{1})$ planes. Additionally, the staggering of these angular boundaries is reminiscent of a stacking-fault structure, which corresponds well with the observed mosaic domain from the low-temperature DFXM measurements.

Calculating the X-ray absorption coefficient per unit length of each potential structure, μ_{struct}, provides a possible explanation for the increased absorption of the fine

structure within the tomographic images. The relative absorption coefficient for each compound is calculated by multiplying the mass attenuation coefficient by the density.

$$\mu_{struct} = \left(\frac{\mu}{\rho}\right)_{compound} \times \rho_{struct} \tag{4.1}$$

The mass attenuation coefficient for a given compound can be determined using a rule of mixtures:

$$\left(\frac{\mu}{\rho}\right)_{compound} = \sum_i w_i \left(\frac{\mu}{\rho}\right)_i \tag{4.2}$$

where w_i is the fraction of the total weight for a given element, i, in the compound, and $\left(\frac{\mu}{\rho}\right)_i$ is the elemental attenuation coefficient. Attenuation coefficients for sodium, manganese and oxygen were estimated for 71.676 keV from tabulated data [69] to be 0.2032 cm^2/g, 0.7953 cm^2/g and 0.1793 cm^2/g, respectively. Weight ratios were calculated by dividing each elemental molar mass by the total molar mass of the compound and input into equation 4.2 to calculate the mass attenuation coefficient for $NaMnO_2$ and Mn_3O_4 as 0.4922 cm^2/g and 0.6230 cm^2/g, respectively. The density of the structures in question, namely α-$NaMnO_2$, β-$NaMnO_2$ and Mn_3O_4, were calculated to be 4.222 g/cm^3, 4.211 g/cm^3 and 4.986 g/cm^3, respectively. The density was calculated using the following equation:

$$\rho_{struct} = \frac{Z \times M}{N_A \times V_{cell}} \tag{4.3}$$

where Z is the coordination number, M is the molar mass, N_A is Avogadro's Number and V_{cell} is the volume of the unit cell. Plugging the calculated values into equation 4.1 results in the following absorption coefficients: (i) 2.078 cm^{-1} for α-$NaMnO_2$, (ii) 2.073 cm^{-1} for β-$NaMnO_2$ and (iii) 3.106 cm^{-1} for Mn_3O_4. These preliminary calculations indicate that Mn_3O_4 is likely responsible for the fine structure seen in the tomographic images. The Mn_3O_4 intergrowth grows along the a or c direction of the α-$NaMnO_2$

structure, depending on which twin variant hosts it. The staggered lines observed in slices through the *ac* plane are therefore assumed to be the result of Mn_3O_4 intergrowths that preferentially form along major twin boundaries, decorated with stacking faults.

4.4 Far-Field HEDM Results

Far-field HEDM provides valuable information on various crystallographic domains, including their centers of mass and relative volumetric proportions by comparing total intensities. The initial results can be qualitatively analyzed by looking at the collected diffraction patterns, summed over the 360° rotation of the sample (see Figure 4.3). The brightest peaks reveal clear lattice lines, that form at specific intervals along the b-direction (vertical), corresponding to the α-phase of the material, as expected. The peak splitting of the twinned crystals can also be seen in several peak pairs of the α-phase's diffraction pattern. Ring-like artifacts in the diffraction pattern correspond to the polycrystalline beryllium hat used to enclose the sample and can be ignored. Qualitative analysis of the diffraction pattern was aided by calculating the theoretical diffraction peak positions for the monoclinic (C2/m) α-$NaMnO_2$, the orthorhombic (Pnmn) β-$NaMnO_2$, and the tetragonal ($I4_1/amd$) Mn_3O_4 crystal structures using Bragg's Law (equation 2.1). The total number of theoretical peaks was reduced by considering systematic absences, or extinction criteria, for each space group [70].

Many of the bright peaks in the diffraction pattern correspond to theoretical peaks from the α and β phases of $NaMnO_2$, making it difficult to discern volumetric proportionality between the two structures. An example in Figure 4.3 is the β-phase's $(1, 0, \overline{1})$ peak, which occupies the same position as the α-phase's $(1, 1, \overline{1})$ peak. This makes it challenging to distinguish between the two phases, however, the lack of observable intensity at locations unique to β-$NaMnO_2$ (*e.g.*, $(0, \overline{1}, \overline{1})$) provide evidence that supports

a near negligible proportion of β-phase domains within the illuminated volume. Interestingly, several peaks that are overlapped by the α and β phases exhibit an in-plane rotational smearing, which indicates an increased mosaic spread (*i.e.*, α-phase $(1, 1, \overline{1})$, $(1, 1, \overline{3})$ and $(2, 2, \overline{2})$ peaks). Additionally, diffuse scattering lines can be seen along the radial direction of the horizontal (H, 0, L) plane, further indicating crystal heterogeneity driven by α-phase faulting that approaches β-phase formation.

On the other hand, weak-but-observable peaks appear halfway between the $NaMnO_2$ lattice lines that explicitly correspond to Mn_3O_4's tetragonal structure. The appearance of these peaks indicates that Mn_3O_4 intergrowths occupy a significant portion of the sample's volume, in alignment with previous results ($\sim$6%) [2]. The relative uniformity of the diffraction spots is evidence that their domains are evenly distributed across the sample's average structure. This basic analysis further supports the hypothesis that the fine structure observed in the X-ray CT data results from the preferential formation of the Mn_3O_4 intergrowths along planar boundaries. The fine structure in the tomographic images extends continuously along the b-direction, which aligns well with the observation of tetragonal peaks appearing across the scanned HEDM layers. While the intergrowth appears to form locally along twin boundaries and stacking fault regions, the abundance of these defects across the sample volume is a likely explanation for misleading bulk averaged results. Measurements that are focused locally to individual twin domains ($<$ 20 μm) should expect to see an increased heterogeneity, driven by the complex interaction between the primary α-$NaMnO_2$ structure and the surrounding Mn_3O_4 intergrowths.

Connecting back to the results of the DFXM investigations of $NaMnO_2$, this preliminary analysis of X-ray CT and HEDM data illuminates the likely source of local structural changes as the Mn_3O_4 intergrowths. Above the 45 K transition temperature, regions inhabited by the intergrowth exhibit a minor strain on the α-$NaMnO_2$ structure due to differing lattice parameters, but heterogeneities from this effect are obscured by

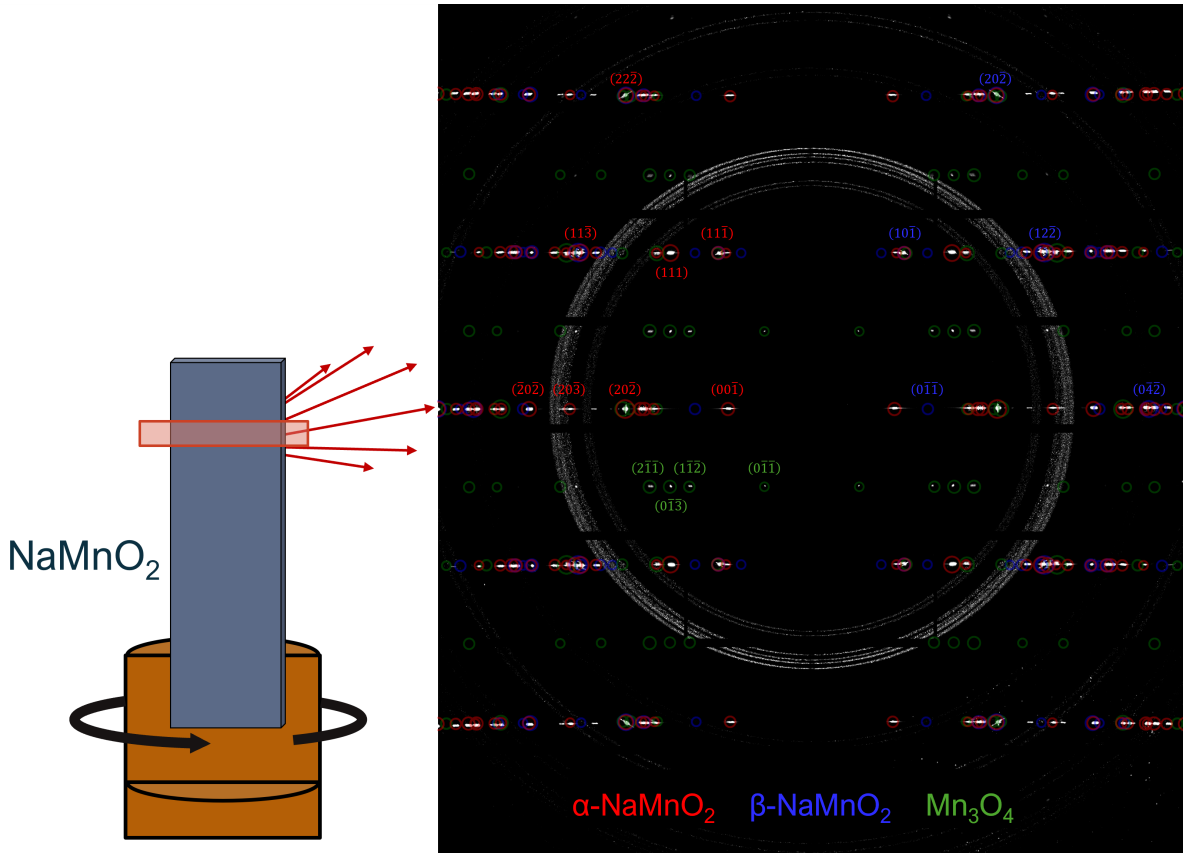

Figure 4.3: Focused schematic of High-Energy Diffraction Microscopy (HEDM) measurements performed on $NaMnO_2$, including a far-field detector image that displays the summed intensities measured through a 360° rotation of the sample. While multiple measurements were performed between vertical translation steps of the sample, scanning the entire 3D volume, the presented representative diffraction pattern originates from a single box beam scan layer. Semi-transparent red, blue and green circles have been overlaid on the diffraction pattern based on the theoretical peak positions of the α-phase, β-phase and Mn_3O_4 intergrowths, respectively. A few select peaks have been labeled with their corresponding (H, K, L) values and the overlaid circle sizes have been scaled proportionally to each peak's estimated structure factor.

other comparable effects, like residual stress build up due to twin formation [17]. Slightly below the antiferromagnetism (AFM) transition temperature of $NaMnO_2$, Mn_3O_4 undergoes a magnetic transition to ferrimagnetic order at 41 K. A ferrimagnetic ground state exhibits magnetic moments that align antiparallel to one another (similar to AFM order), but with nearest neighbor moments differing in magnitude, which results in a

weak ferromagnetism. This weak ferromagnetic interaction likely drives distortion in $NaMnO_2$'s AFM lattice and results in the rotational variance observed in DFXM imaging. The fault-like mosaic domain that appears in the low temperature DFXM images (see Figure 3.8) is assumed to represent a region dominated by the Mn_3O_4 intergrowths, which relaxes the rotational distortion to the principle lattice upon warming past 41 K. The demonstrated combination of rich datasets from DFXM, X-ray CT and HEDM measurements provides an avenue for a multi-modal approach to spatially resolving complex defect structures across multiple length scales.

Chapter 5

Quantum Material Study: CsV_3Sb_5

5.1 DFXM Imaging Beyond the Host Lattice

To investigate the heterogeneity of CsV_3Sb_5's charge order and crystal structure, a low-temperature Dark-Field X-ray Microscopy (DFXM) experiment was performed. Previous demonstration of low-temperature DFXM on $NaMnO_2$ laid the groundwork for a DFXM study of stacking order and phase separation within the charge-density-wave phase of CsV_3Sb_5 below 94 K. This study was primarily motivated to resolve ambiguity between fractional charge-density-wave (CDW) peaks to determine whether the CDW is characterized by a single crystallographic domain that produces two Fourier components or by two physically separate domains that result in two respective Fourier components. The DFXM work on CsV_3Sb_5 presented here represents the first example of employing hard X-rays to collect dark-field images of charge order Bragg peaks in a quantum material.

The experiment detailed in this thesis was conducted on a high-quality, single-crystal sample of CsV_3Sb_5. The plate-like sample was grown using the flux method detailed in Ortiz *et al.* [18]. The sample was mechanically exfoliated with tape to remove surface

impurities and achieve a desired thickness of ≈100 μm, enabling a transmission scattering geometry. The sample's crystal and magnetic properties were confirmed after growth using a combination of X-ray Diffraction (XRD), Energy Dispersive X-ray Spectroscopy (EDS), and Superconducting Quantum Interference Device (SQUID) magnetometry. The layered hexagonal nature of the material lends itself well to macroscopic alignment, as facets form naturally along the $[1, 0, 0]$ and $[0, 1, 0]$ directions. Here, the sample was initially oriented such that the $[0, 0, 1]$ direction and the reciprocal lattice vector $(1, 1, 0)$ were parallel and perpendicular to the incident beam respectively (Figure 1.3).

5.2 DFXM Setup at 6 ID-C

DFXM measurements were performed at the 6-ID-C beam line of the Advanced Photon Source (APS) at Argonne National Laboratory as described in section 3.1.1 and 3.2.1. The experimental configuration followed the low-temperature setup used to study $NaMnO_2$, but with the following key differences. The Si monochromator tuned the incident X-ray beam between 20 and 22 keV. A 50 μm pinhole was placed just in front of the objective lens to reduce noise from the divergence of the diffracted signal. A similar polymeric compound refractive lens (CRL), designed for 20 keV X-rays, was used as the objective with a focal length of 131 mm and working distance of 140 mm [50, 63]. In addition to the Zyla detector, a second direct-detecting X-ray area detector was mounted to the translation/rotation stage to capture the magnified diffraction signal at the image plane. The diffracted illumination was ultimately limited to 20 μm in width by the incident slit screen and 50 μm in height by the exit pinhole.

The inherent X-ray absorption of the DFXM technique, presents a significant challenge to imaging weak diffraction peaks, such as those formed by charge-density waves. To overcome this challenge, a large-area Medipix3-based-detector array (LAMBDA) from

X-Spectrum was used to image the CDW signal at $\mathbf{q_1} = \left(\frac{1}{2}, \frac{1}{2}, \frac{1}{2}\right)$ and $\mathbf{q_2} = \left(\frac{1}{2}, \frac{1}{2}, \frac{1}{4}\right)$. This X-ray area detector is direct X-ray detecting with single photon counting sensitivity. While the LAMBDA detector results in a reduction of spatial resolution due to the removal of an optical objective and a native pixel size of 55 μm, its direct detection improves temporal resolution and signal-to-noise ratio when compared to the Zyla detector. The use of direct detection in tandem with DFXM is an exciting new methodology for imaging weakly diffracting systems [52]. CDW images collected using this detector, paired with the X-ray magnification of the CRL, yield an effective pixel size of 2.1 μm. A second, higher resolution area detector, was employed to capture images of CsV_3Sb_5's brighter, primary structural peaks. This detector is composed of a 20 μm LuAG:Ce X-ray scintillator, reflective mirror, 5× optical objective lens, and a 5.5-megapixel sCMOS Zyla camera made by Andor. With a native pixel size of 6.5 μm, the effective pixel size of images collected using the Zyla detector is 0.05 μm. The resulting experimental feature resolution, or the smallest resolved line-pair, of the LAMBDA and Zyla detectors are ≈ 2 μm and ≈ 400 nm, respectively. In DXFM measurements, the crystal was initially oriented such that the $[0, 0, 1]$ direction and the reciprocal lattice vector $[1, 1, 0]$ were parallel and perpendicular to the incident beam respectively.

Due to a small numerical aperture, axial (depth) resolution along the diffracted beam direction (*i.e.* k') is poor. In this DFXM setup, a transmission horizontal scattering geometry was used. So, the depth resolution is given to be an effective width of the incident beam along an intersection of a line parallel to k'. As a consequence, it is not possible to isolate CDW or twin domains lying along k'. While tomographic approaches may be used to obtain depth sensitivity, it requires a complete azimuthal rotation around the scattering vector, which was not possible given the mechanical restrictions of the cryostat and sample morphology. Nevertheless, a vertical 50 μm tall, 20 μm wide beam was used to illuminate a thin slice of the crystal to reduce the number of domains contributing to

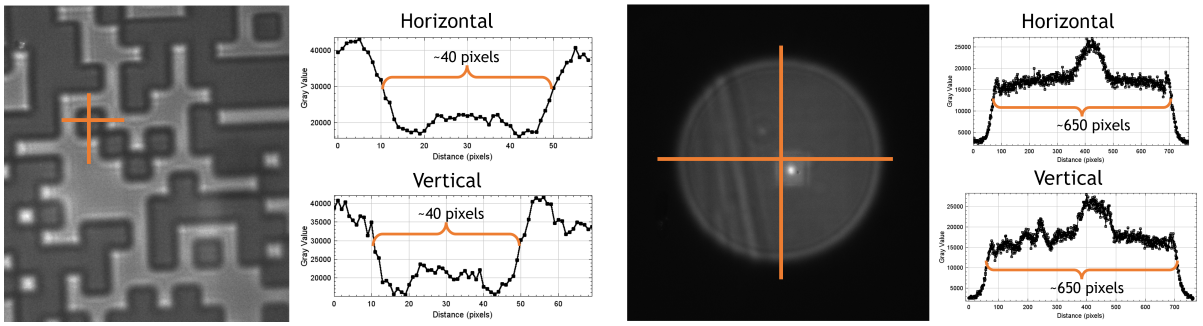

Figure 5.1: (left) X-ray absorption image taken of the coded mask using the polymeric compound refractive lens (CRL) as an objective. (right) X-ray absorption image of the pinhole, placed just before the objective lens. Orange lines have been overlaid on the images to indicate the location of the horizontal and vertical line profiles analyzed. Plots of the profiles are shown next to each image with the distance between peaks displayed (in pixels).

a given pixel in each image, which was obtained by translating the sample through the incident beam. As a result, clean domain boundaries were identified in DFXM images. In the future, the use of coded aperture to generate structured illumination can be used for a complete 3D reconstruction of CDW domain networks, as was demonstrated in a recent study of nematic order in a pnictide superconductor [71].

The X-ray magnification factor of the objective lens was determined *in situ*, using a patterned calibration mask with $2 \times 2\ \mu m^2$ structures. X-ray absorption-contrast images were taken of the mask with the polymeric CRL employed, using the Zyla area detector described in section 3.1.1. Images of the pinhole were also collected in this way and both can be seen in Figure 5.1. The resulting images were then used to calculate an effective X-ray magnification factor and an effective pinhole size. Evaluating the distance between inflection points of the line profile taken across the mask resulted in a 40 pixel width and height of each structure. Dividing the known structure size by the pixel size gives an effective pixel size of 0.05 μm, or 50 nm. The native pixel size of the Zyla detector is 6.5 μm, which results in a total magnification factor of 130$\times$ when divided by the calculated effective pixel size. The Zyla detector configuration hosts a 5$\times$ optical objective, leaving

a factor of 26× as the calculated X-ray magnification factor. Similarly, the inflection points of the line profile taken across the pinhole established an effective pinhole size of 650 pixels. Multiplying the pinhole diameter measured in pixels by the effective pixel size converts the value to a calculated 32.5 μm effective pinhole diameter.

5.3 Microstructural Length Scales and Twin Formation

To investigate the CDW phase's effect on the local microstructure of the *ab* plane, a high-resolution Rocking Curve Imaging (RCI) scan using the $(2, 2, 0)$ Bragg peak ($2\theta = 23.61°$), was collected at a base temperature of 3.2 K. A sample temperature of 3.2 K is above the superconducting transition at 2.5 K and ensures a complete formation of the CDW phases. The Zyla detector was employed to image the structural peak across θ positions in fine 0.001° steps, with 5 seconds of exposure. By evaluating the total intensity of each image with respect to the sample's θ position, an intensity curve akin to the results of single crystal diffraction can be obtained. For the $(2, 2, 0)$ peak, an average full width at half maximum (FWHM) of 0.024° is observed, which aligns with expectations for a highly crystalline sample. The intensity of each pixel, across a stack of images in a given RCI scan, exhibits contrast due to a combination of reciprocal space and real-space sources. The maximum intensity image of the $(2, 2, 0)$ peak reveals an array of highly linear boundaries (see Figure 5.2). The scattering geometry of the $(2, 2, 0)$ Bragg peak implies that the resulting DFXM images are projections taken at a shallow angle (13°) from the c-axis. The contrast boundaries observed in Figure 5.2, are therefore assumed to be an average representation of the structure along the stacking direction.

Two distinct features can be observed across the 32.5 μm field-of-view: (i) triple-point

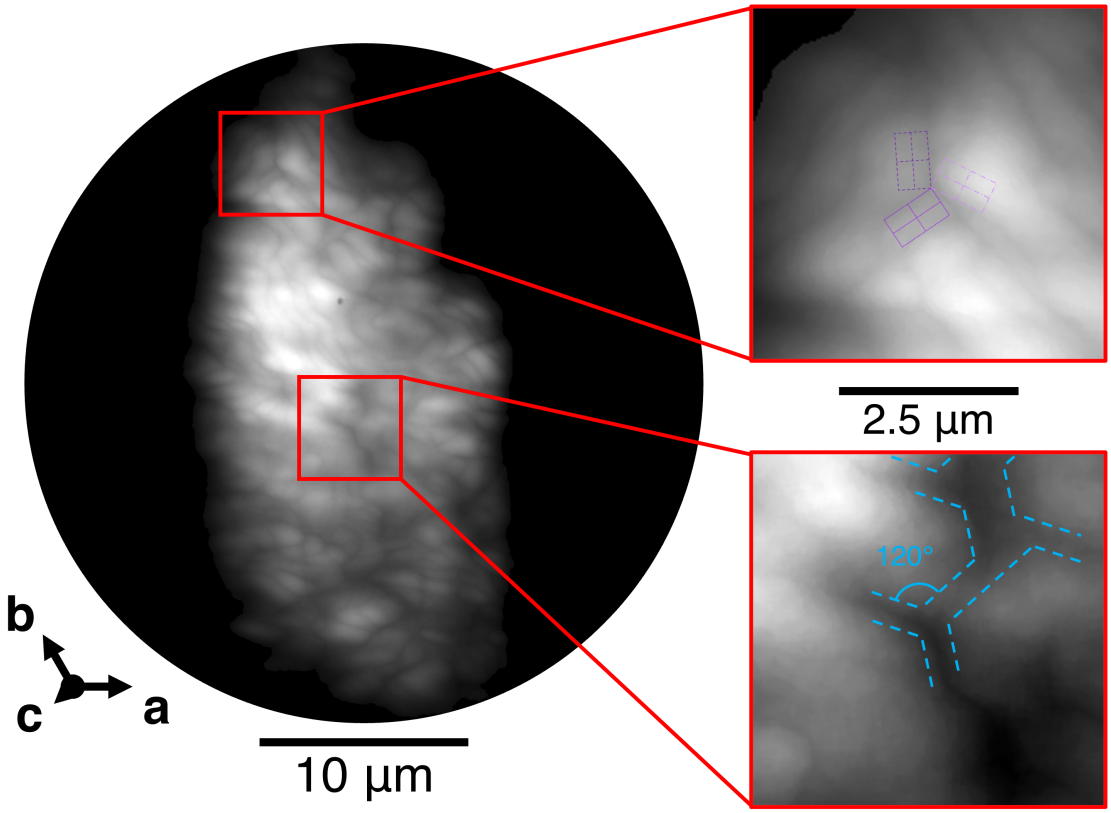

Figure 5.2: High-resolution image of the $(2, 2, 0)$ peak of CsV_3Sb_5 at low temperature (3.2 K), which illustrates a network of crystal domains across the 32.5 μm span of the image. Real-space crystal axes and a scale bar are included at the bottom of the image. Two cutouts of triple-point boundaries, outlined in red, have been magnified and presented to the right of the primary image. The top cutout is overlaid with the twinning diagram from Figure 1.4 to highlight the experimental validation of the theoretical twinning model. The lower cutout is overlaid with cyan dashed lines that emphasize a network of triple-point boundaries that form larger hexagonal domains.

boundaries that are 120° separated; (ii) two-dimensional domain modulations in groups of three or more. Two such regions, centered on boundaries with three-fold symmetry, have been highlighted and digitally magnified for presentation in Figure 5.2. The triple-point boundaries are coordination centers for rotational twinning and are artifacts of the original hexagonal geometry. These boundaries extend an average of 3.7 μm from their centers, from which it is estimated the original hexagonal domains spanned 5.55 μm and

above. The two-dimensional modulations can be seen extending from these junctions, exhibiting boundaries that are perpendicular to its opposing triple-point boundary. These modulations appear with an average wavelength of 1.2 μm and are likely indicative of domain terracing along the stacking direction. The existence of these boundary types serve as visual evidence of rotational orthorhombic twinning. Qualitative observations can be made of a slight preference for boundaries that are rotated 150° counter-clockwise from the a-direction (30° from the horizontal). Boundaries with this orientation are related to the b-axis of the third twin variant (rotated by 240°). This preference is further evidenced by the FWHM image of the $(2, 2, 0)$ peak shown in Figure 5.3, which reveals 30° boundaries that extend over 10 μm. These boundaries are indicative of a longer-range correlation of the local boundaries seen in figure 5.2, that depend on the preferred twin variant within the illuminated volume. This data supports a model of CsV_3Sb_5, where the structural distortions below T_{CDW} result in local structural symmetry breaking that maintains a pseudo-six-fold symmetry within individual planes and at larger length scales.

The full extent of crystal heterogeneity across hundreds of μm will require more measurements, however, the results presented here offer evidence for planar twin domains correlating across layers through shared planar boundaries. Upon cooling to 3.2 K the crystal structure is broken up into stacked two-dimensional twin domains that extend several μm across the ab plane. The mosaic image of the $(2, 2, 0)$ peak shows a near-planar orientation gradient which reveals mosaic regions that span the field-of-view. Notably, the central mosaic boundary follows a fault line that passes through multiple of the observed triple-point boundaries. This pattern enforces the idea of twin boundaries nucleating along larger (likely pre-existing) hexagonal boundaries, with twin variants locally competing for formation. The exact nature of this competition is an interesting avenue for future studies.

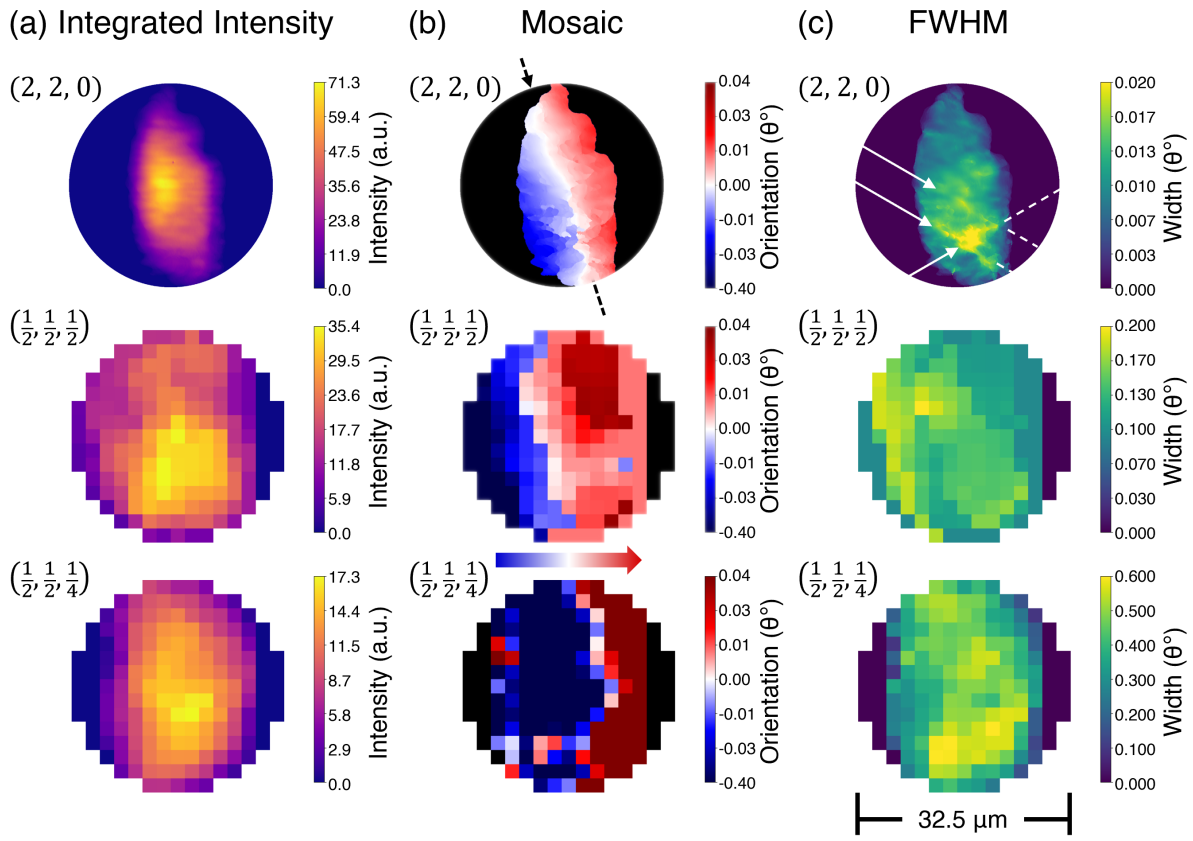

Figure 5.3: Overview and comparison of the Dark-Field X-ray Microscopy (DFXM) data collected on CsV_3Sb_5, at a single position, from the (H, K, L) indicated in the top left corners. For each peak (H, K, L), the following is displayed from left to right: Images of the integrated intensity of each pixel across θ positions are shown, characterizing the illuminated volumes of each peak's crystallographic domain of origin, projected to a 2D image. The angles of incidence for all three Bragg peaks are similar enough that the illuminated volumes are equivalent. The absolute intensity values for the $(2, 2, 0)$ peak should not be directly compared to the charge-density-wave (CDW) peak intensities due to the different detectors employed to capture them. Images of the relative misorientation (mosaic) of each pixel's fit center-of-mass compared to the image averaged center-of-mass are also presented. Mosaic images highlight contrasts due to changes in crystal orientation and display mosaic boundaries. Lastly, images of the full-width-at-half-maximum (FWHM) fit to each pixel are shown. A black arrow and dashed line has been added to the mosaic image of the $(2, 2, 0)$ peak to guide the eye to the linear mosaic boundary therein. White arrows and dotted lines have been added to the $(2, 2, 0)$ peak's FWHM image to highlight 30° boundaries that can be identified by their increased width values.

5.4 Charge-Density Wave Phase Separation

At the same sample location, DFXM images were also collected using the two charge-density wave Bragg peaks previously discussed. The LAMBDA detector, described in section 5.2, was employed to image the weaker CDW peaks using a 10 second exposure time, and 0.1° θ steps. One-dimensional intensity curves for both signals can be generated in a similar fashion to the $(2, 2, 0)$ peak for comparison. A maximum intensity of ≈21,000 a.u. was observed for the $\left(\frac{1}{2}, \frac{1}{2}, \frac{1}{2}\right)$ peak, while a maximum intensity of ≈3,600 a.u. was observed for the $\left(\frac{1}{2}, \frac{1}{2}, \frac{1}{4}\right)$ peak. The $\left(\frac{1}{2}, \frac{1}{2}, \frac{1}{4}\right)$ peak's factor of 6 reduction in intensity coincides with a factor of 3 increase in the FWHM (0.472°), resulting in a factor of 2 reduction of the θ integrated intensity. The theoretical structure factors for the diffraction of the CDW peaks is comparable when normalized by their respective supercell volumes, suggesting that the difference in integrated intensity is primarily dependent on the illuminated volume. The angular difference between CDW peaks is relatively minor ($\Delta 2\theta \approx 0.2°$), so differences due to projection effects are assumed to be negligible. The significant difference between each signal's total contributed intensity is therefore assumed to be indicative of independent volume contributions that are separated along the stacking direction.

To evaluate possible in-plane CDW separation the resulting integrated intensity, mosaic and FWHM images are similarly displayed in figure 5.3. Mosaic plots of the CDW peaks show a left-to-right orientation gradient for the $\left(\frac{1}{2}, \frac{1}{2}, \frac{1}{2}\right)$ and $\left(\frac{1}{2}, \frac{1}{2}, \frac{1}{4}\right)$ peaks, qualitatively similar to the mosaic boundary seen in the primary $(2, 2, 0)$ peak. Notably, the $\left(\frac{1}{2}, \frac{1}{2}, \frac{1}{4}\right)$ peak mosaic demonstrates a much sharper orientation gradient extending from the central boundary than the $\left(\frac{1}{2}, \frac{1}{2}, \frac{1}{2}\right)$ peak, consistent with their varied FWHMs. The intensity distribution for each CDW peak is also qualitatively similar across the illuminated area, while the FWHM distributions of each peak show some subtle variance;

however these maps suffer from the poorer resolution of the detector setup needed to resolve the CDW order. The general broadening of the $\left(\frac{1}{2}, \frac{1}{2}, \frac{1}{4}\right)$ peak does suggest that the signal originates from areas within the sample with higher concentrations of local defects (*i.e.*, dislocations, twin boundaries, *etc.*). These differences in character, paired with peak coexistence (non-zero signal) across the 32.5 μm field-of-view, support theories of two spatially distinct CDW phases forming through the transition, which preferentially separate along the the stacking direction based on the local ($\sim \mu m$) environment. To explore further and at length scales outside of the 32.5 μm field-of-view, the incident X-ray illumination was rastered across the sample.

To acquire images of the CDWs across a larger length scale, a series of RCI scans were collected for each peak at various sample locations. Images were taken at positions spanning 500 μm in the vertical direction and 10 μm in the horizontal direction. Images from a given peak were subsequently stitched together according to each scan's relative position. The sample was moved between scans such that there was no overlap in the vertical-direction (50 μm steps) and an 66% overlap in the horizontal-direction (10 μm steps). During the stitching process, overlapping pixels were assigned to the maximum value from the contributing scans for a given θ position. Figure 5.4 shows the stitched DFXM images for the $\left(\frac{1}{2}, \frac{1}{2}, \frac{1}{2}\right)$ and $\left(\frac{1}{2}, \frac{1}{2}, \frac{1}{4}\right)$ peaks. The reduction in total intensity and increase in FWHM observed at the first position of the $\left(\frac{1}{2}, \frac{1}{2}, \frac{1}{4}\right)$ peak, are demonstrated again at this length scale and evaluating this larger surveyed area gives a more complete picture of the CDW texture in the crystal.

The resulting stitched maps reveal that both CDW orders exist across hundreds of μm in the *ab* plane, in agreement with previous observations. Looking first at the mosaic shift maps, three distinct regions appear, colored to represent their relative negative and positive shifts from center respectively. The predominant mosaic boundary separates the scanned region into upper and lower halves of the stitched plots. An additional,

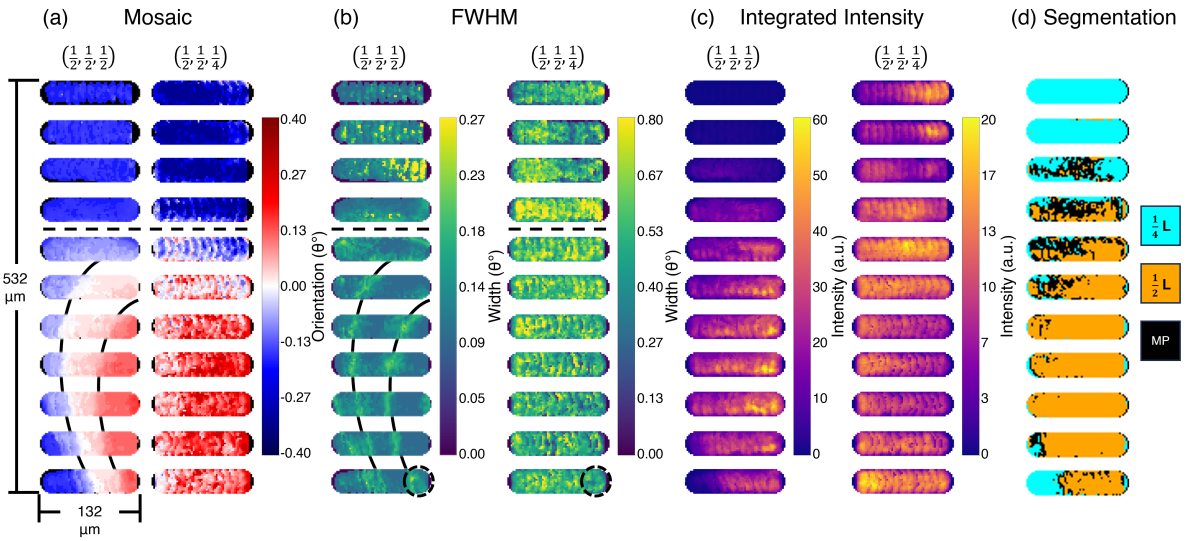

Figure 5.4: Large-area Dark-Field X-ray Microscopy (DFXM) maps created by stitching individual images based on sample position during area rastering. Parameters calculated from two charge-density-wave signals ($\mathbf{q_1}$ and $\mathbf{q_2}$) are presented side-by–side for visual comparison. Displayed from left to right, are maps of the pixel-based mosaic spread, full width at half maximum (FWHM), and integrated intensity, shown with their respective color bars. Additionally, a corresponding segmentation map is displayed, with each pixel denoting the dominate charge-density-wave (CDW) signal (by integrated area) of its related material position. Black pixels in the segmentation map denote areas in which there is a mixed peak "MP" signal, meaning that both the integrated intensity from each CDW signal is within 30% of the other. Scale bars displayed on the leftmost image indicate the total area spanned by the DFXM measurements. Black dashed circles in the bottom right of each FWHM map denote the singular location of the images presented in figure 5.3. Black solid and dashed lines are also included in the mosaic and FWHM maps to guide the reader's eye to horizontal gradients in the $(\frac{1}{2},\frac{1}{2},\frac{1}{2})$ signal and vertical gradients present in both signals, respectively.

horizontal gradient appears in the $(\frac{1}{2},\frac{1}{2},\frac{1}{2})$ peak that coincides with an increase in integrated intensity, indicating added depth-integrated or terraced subdomains. In contrast, the $(\frac{1}{2},\frac{1}{2},\frac{1}{4})$ peak does not exhibit a comparable horizontal subdomain structure. The FWHM maps of each peak further confirm a two-domain solution, showing an expected broadening near this boundary.

The FWHM plots of each peak further highlight the domain structure, showing an expected broadening near the domain boundaries. Both the FWHM of the $(\frac{1}{2},\frac{1}{2},\frac{1}{2})$ and

$\left(\frac{1}{2}, \frac{1}{2}, \frac{1}{4}\right)$ peaks show a slight broadening at the vertical domain boundary identified in the mosaic maps. Furthermore, elliptical domain boundaries appear in the FWHM plots of the $\left(\frac{1}{2}, \frac{1}{2}, \frac{1}{2}\right)$ peak in the region where a horizontal gradient in the mosaic offset was identified. This indicates the presence of two to three additional domains contained within the lower half of the scan. The FWHM map for the $\left(\frac{1}{2}, \frac{1}{2}, \frac{1}{4}\right)$ peak remains relatively uniform in this same region (aside from the slight broadening at the vertical domain boundary).

Turning now to the integrated intensity maps of Fig. 5.4, a clear anticorrelation between the $\left(\frac{1}{2}, \frac{1}{2}, \frac{1}{2}\right)$ and $\left(\frac{1}{2}, \frac{1}{2}, \frac{1}{4}\right)$ maps appears. In regions where the $\left(\frac{1}{2}, \frac{1}{2}, \frac{1}{2}\right)$ peak is maximal, the $\left(\frac{1}{2}, \frac{1}{2}, \frac{1}{4}\right)$peak is reduced and visa versa. This is additional evidence that the $\left(\frac{1}{2}, \frac{1}{2}, \frac{1}{4}\right)$ peak directly competes with the $\left(\frac{1}{2}, \frac{1}{2}, \frac{1}{2}\right)$ peak regions for domain formation. It is stressed here, however, that throughout the majority of these maps both peaks appear with varying intensities. This implies a mixed signal via depth averaging of spatially separated domains through the crystal volume.

To add quantitative rigor to the observation of CDW competition, a segmentation map of the scanned area is presented in Figure 5.4. Segmentation was carried out by evaluating the θ integrated intensity from each CDW signal for a given pixel. The signal that produced a higher integrated intensity is assumed to come from the dominant volume and is assigned a peak label. Regions colored with cyan represent regions where the integrated intensity of the $\left(\frac{1}{2}, \frac{1}{2}, \frac{1}{4}\right)$ peak exceed the integrated intensity of the $\left(\frac{1}{2}, \frac{1}{2}, \frac{1}{2}\right)$ peak by 30%, while orange regions correspond to the inverse condition. Black pixels are designated in regions where integrated intensities are within 30% of one another. The relative scarcity of black pixels observed in the segmentation map illustrates that, even when summed along the diffracted beam, material regions of CsV_3Sb_5 prefer to be dominated by one CDW peak or the other. These results further support the competition and existence of two distinct CDW phases that form independently in separate crystal

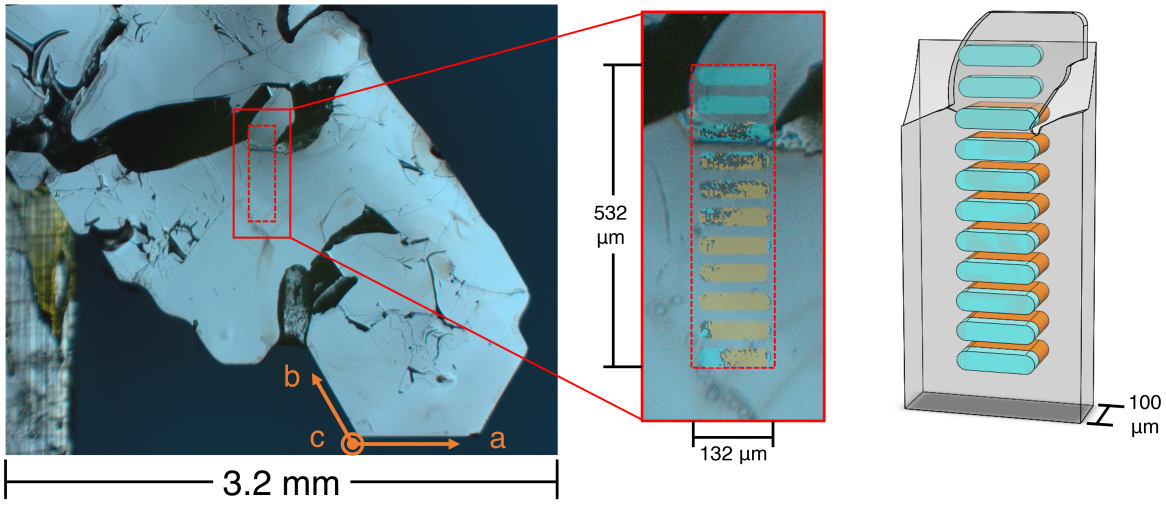

Figure 5.5: Optical microscope image of CsV_3Sb_5 sample, as it was measured in the Dark-Field X-ray Microscopy (DFXM) experiment. Orange arrows indicate the real-space crystallographic orientation of the sample. Rectangles drawn on the image using solid and dashed red lines indicate the area of the magnified image cutout presented to the right and the relative area covered in the DFXM scans of the charge-density-wave (CDW) peaks, respectively. The magnified cutout is displayed with an overlay of a semi-transparent version of the segmentation map shown in figure 5.4. This overlay highlights the relationship between the macroscale characteristics observed in the optical images with the mesoscale characteristics observed in the stitched DFXM images. On the right, a perspective view of a 3D model is also shown to illustrate the hypothesized separation of the CDW domains along the stacking direction. Scale bars are denoted in black to indicate the relative size of images and depth of the model.

domains.

The mesoscale (μm) DFXM results can be connected to macroscale (mm) optical images of the sample to obtain a better understanding of the possible sources for the previously described differences in CDW character. Figure 5.5 displays the scanned area relative to the real-space sample along the ab plane. A relatively undisturbed metallic surface can be observed over much of the sample area, however the top of the scanned area corresponds to a physically deformed region that extends over a large void. The deformation manifests as a small tab of material (10-50 μm) that has been bent or twisted out-of-plane while still connecting to the top most layers of the nominal sample volume.

This visible deformation helps elucidate the large tilt in orientation ($\sim 1°$) observed in the stitched mosaic maps.

Surveying across this region, where the thickness of the crystal becomes narrower, suggests that changes in the CDW domain structure correspond to defect boundaries in the crystal. The segmented region with a dominant $\left(\frac{1}{2}, \frac{1}{2}, \frac{1}{4}\right)$ peak appears across the boundary with the upper tab of crystal and seemingly also begins to appear near a lower boundary line at the bottom of the scan. The volumetric contribution to intensity from the $\left(\frac{1}{2}, \frac{1}{2}, \frac{1}{2}\right)$ peak is nearly eliminated in the top third of the scanned area. This effect is attributed to the large void present behind the deformed material tab. A three-dimensional representation of this domain configuration is presented in Figure 5.5.To further elucidate how these surface features correlate with the depth dependence of the CDW states using DFXM, requires overcoming the loss of depth sensitivity along the projection vector of the Bragg peak, which is an active area of research [71]. Despite this region being thinner than the neighboring domain, the crystallinity of the CDW order, as assessed via the FWHM, is identical on either side of the boundary. This suggests a picture of spontaneous nucleation of nearly degenerate CDW states about a local defect rather than a deformation-driven change in the local energy landscape. Regardless of the impetus for the spatial transition between $2 \times 2 \times 2$ to $2 \times 2 \times 4$ CDW states, the DXFM data demonstrate a clear competition between the two states in spatially segregated regions at the 100 μm length scale.

5.5 Crystal Evolution Through CDW Transition

In addition to the investigation of the structural $(2, 2, 0)$ Bragg peak at low temperatures, a series of RCI scans were also conducted while heating the sample through the charge-density-wave (CDW) transition temperature of 94 K. Temperature evolution

measurements were performed on the $(2, 2, 0)$ peak to look for structural mechanisms that possibly drive the CDW transition and establish a connection to the crystal's room temperature ground state. The data from these scans, presented in Figure 5.6, shows that the peak undergoes a significant change in orientation between 93 K and 94.1 K, coinciding with a drop in the integrated intensity. A horizontal shift in the integrated intensity maps is also observed through this change, with intensity diminishing by approximately 25% after the transition. The mosaic images reveal a drastic shift from positive to negative tilt in the illuminated domain, followed by a mixing of tilts and the formation of red and blue regions as the temperature continues to increase. The FWHM images show a sudden increase in the total width of the peak after the initial domain rotation, suggesting increased disorder. Shifting boundary lines occur throughout the subsequent temperature-dependent images up to 94.4 K.

These preliminary observations show a structural volatility near the CDW transition temperature as disorder is increased, resulting in peak broadening, as the transition is approached. Once the transition is completed below 94 K the peak width decreases significantly, suggesting a structural reordering due to the sudden completion of the thermodynamic phase transition. While there is an overall mosaic tilting that coincides with the transition, the local mosaic distribution is relatively well preserved. This result provides some indication of a preservation of domain boundaries and defects through the transition temperature, suggesting a direct relationship to defects formed during formation to the heterogeneities observed within the CDW phase. The structural texture across the mesoscale of CsV_3Sb_5 that informs the formation and competition between distinct CDW domains is likely connected to local structural heterogeneities at room temperature, but resolving this connection concretely would require additional measurements.

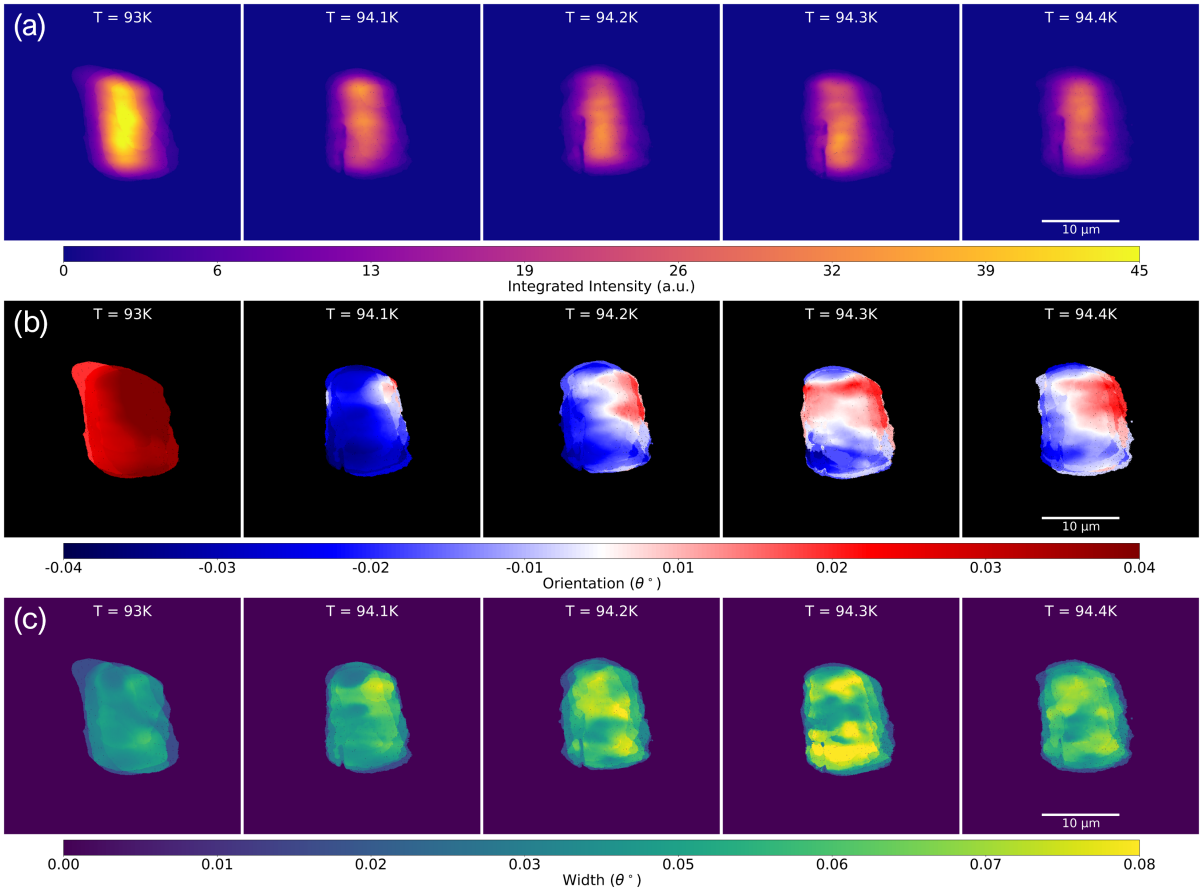

Figure 5.6: Series of Dark-Field X-ray Microscopy (DFXM) images of CsV_3Sb_5's $(2, 2, 0)$ peak, taken at increasing temperatures through the charge-desnity-wave (CDW) transition at 94 K. The temperature evolution is characterized with images of integrated intensity (a), mosaic (b) and full width at half maximum (FWHM) (c), presented side-by-side for qualitative comparison. Peak positions were spatially centered in post-processing to enhance visual comparison and mosaic values were centered relative to the average orientation center of the displayed scans.

Chapter 6

Conclusions and Future Work

6.1 Summary of $NaMnO_2$ Work

Spatially resolved Dark-Field X-ray Microscopy (DFXM) images were collected across the mesoscale of $NaMnO_2$. The initial investigation focused on a room-temperature survey of an *alpha*-$NaMnO_2$ single crystal that spanned several millimeters. Dark-field imaging revealed a complex crystal landscape, characterized by large linear domain features that span hundreds of μm longitudinally and averaged about 20 μm in the transverse direction. Analysis of rocking curve image scans collected across the sample surface, confirmed that the $NaMnO_2$ sample is characterized by these linear domains that extend along the growth direction, which are further divided into subdomains on the order of μm along the long-axis.

Once the general structural features of $NaMnO_2$ were established and the characteristic length scale of heterogeneity was understood, a first-of-its-kind, low-temperature DFXM experiment to investigate possible nanoscale-magnetostructural transitions below 45 K was performed. Spatially-resolved DFXM images indicated that local changes occurred through the transition temperature, including negative tilting of globular domains

and subtle shifts in boundaries, as identified by full width at half maximum (FWHM) values. However, the results did not provide enough evidence to clearly distinguish between triclinic domain formation, or magnetostriction effects associated with the ferromagnetic transition of Mn_3O_4 intergrowths, as the origin of the observed changes. The experiment detailed here is the first low-temperature DFXM study reaching liquid-helium temperature on a highly heterogeneous single-crystal sample at a third-generation light source, which enables spatially resolved studies of twins, dislocations, charge-order or magnetic domains through a wide array of thermal phase transitions. The experimental procedure outlined in this thesis lays the foundation for the characterization and evaluation of other functional and structural materials at low temperatures. For example, recent DFXM measurements were performed on $La_{0.7}Sr_{0.3}MnO_3$ (LSMO) at 115 K to explore the mechanisms behind the metal-to-insulator transition that enables its use as a neuromorphic device [72].

To further investigate these findings, a follow-up defect study was conducted on the same $NaMnO_2$ single crystal using X-ray Computed Tomography (CT) combined with far-field High-Energy Diffraction Microscopy (HEDM). Preliminary analysis and tomographic reconstructions revealed fine faulting structures throughout the 3D volume of material. The diffraction patterns suggest that these fine structures are most likely associated with the β-phase of $NaMnO_2$. This evidence suggests that local distortions take place in privileged regions close to defect boundaries within an intertwined hierarchy of three-dimensional structural and phase heterogeneities, which span a wide range of length scales. This is consistent with significant local changes observed in the low-temperature DFXM study. More comprehensive DFXM studies of spatially resolved strain as a function of temperature may indicate a mechanism for the local intensity increase through the transition. Together, these results highlight the critical role of local heterogeneities in the low-temperature magnetic transition of this material and demonstrate the potential

of DFXM for studying complex quantum materials.

6.2 Summary of CsV_3Sb_5 Work

The author's also completed a low-temperature investigation of phase separation of charge-density-wave (CDW) states in CsV_3Sb_5, across multiple length scales using DFXM. DXFM data directly observe the spatial separation between CDW domains with dominant $2\times2\times4$ CDW and $2\times2\times2$ CDW characters. These domains seemingly switch along defect boundaries apparent at the crystal surface, suggesting a complex interplay between the nucleation of CDW order and texture (*e.g.* defects, twin domain boundaries) within the crystal lattice. Evaluation of the functional differences and regional intensities for both CDW signals show that the electronic super-structures spatially compete with one another during formation. These data are consistent with a number of nearly degenerate CDW states with wave vectors along the M-L line [41] that, across a first-order phase boundary, are pinned locally by defects in the crystal.

High-resolution images of the $(2, 2, 0)$ structural peak reveal a complex microstructure that is composed of a network of crystal domains that average a few μm in size. Signatures of orthorhombic twinning, including triple-point boundaries and stripe-like domains, are also present in the structural images. Notably, the observed angular boundaries don't display an obvious preference for orientation, evidence for roughly equal proportions of the three twin variants. Triple-point boundaries serve as demonstrations an average pseudo-six-fold symmetry as the projection vector of the $(2, 2, 0)$ Bragg peak lies near the interlayer direction, producing contrast boundaries from multiple twinned domains ordered along the stacking direction.

6.3 Looking Forward with DFXM

As described in Chapter 4, far-field High-Energy Diffraction Microscopy (HEDM) and X-ray Computed Tomography (CT) data were collected over the entire single-crystal sample of $NaMnO_2$ that was measured with DFXM. Combining the data from these two complementary experimental methodologies represents a promising avenue for spatially resolving and defining defects within highly complex materials. By providing spatial information about defect states and complex phases, DFXM data can be combined with other techniques to generate rich multi-modal datasets. Once a location of interest is established with DFXM, an additional probe, such as angle-resolved photoemission spectroscopy (ARPES), can be employed to study the same region. ARPES measurements evaluate the kinetic energy and emission angle of electrons as they are ejected from an illuminated sample, providing insights into the band structure and Fermi surface of the given compound. Utilizing a combination of DFXM and ARPES datasets presents a methodology for understanding complex electronic states and their connection to structural heterogeneities.

Future DFXM experiments could also be performed to map the temperature evolution of charge-density-wave (CDW) phases within kagome materials, like CsV_3Sb_5 or its K and Rb cousin compounds, which could provide deeper insights into the nature of CDW transitions and the mechanisms that drive them. While the DFXM experiment on CsV_3Sb_5 partially focused on the temperature evolution of the $(2, 2, 0)$ Bragg peak, it would be valuable to extend this analysis to image the two CDW peaks through their respective transition temperatures. One could also think of capturing DFXM images through the heating and cooling processes to identify local hysteretic behavior.

In terms of technique development, there are several directions for improving DFXM. One challenge concerns the limited depth resolution of the projected images. DFXM's

scattering geometry collects illumination on a 2D area detector, summing intensities from diffraction sources along the projection vector and thus losing depth information. One approach to overcome this limitation is to rotate the sample around the momentum vector Q and capture images at various projection angles. A series of images captured this way could potentially be reconstructed into a 3D volume using modified tomography algorithms. However, this method presents challenges related to the precise alignment of rotational centers, which is constrained by the mechanical limits of the experimental setup. Another approach to restore depth resolution involves the use of a semi-transparent coded mask placed before the sample [71]. By scanning the coded mask back and forth while collecting images, phase information could possibly be retrieved from the resulting images. This would further enable more accurate path-length calculations for the diffracted X-rays, producing higher-resolution images.

The recent upgrade of the Advanced Photon Source (APS-U) projects a 500× increase in brightness to the synchrotron source, providing an exciting potential for future coherence-enhanced DFXM measurements. The use of a multi-bend achromat lattice of magnets and superconducting undulators will produce a higher flux of photons and extend coherence-based techniques to higher energy methods, like DFXM. The use of highly coherent X-rays combined with imaging through the defocused region of the diffracted light offers a methodology for capturing DFXM images with increased phase contrast. The use of highly coherent light is vital to this endeavour to maintain spatial resolution as the wave front propagates. Data collected at the back focal plane measures the conventional diffraction peak while data collected at the image plane measures the diffracted wave front just after it leaves the sample, where it still contains spatially resolved information. Data collected in between these two extremes, or in the defocused region, may be leveraged to observe the evolution of the diffracted wave front as it goes from Fourier space to Real space. Preliminary DFXM images collected on $NaMnO_2$ in the defocused

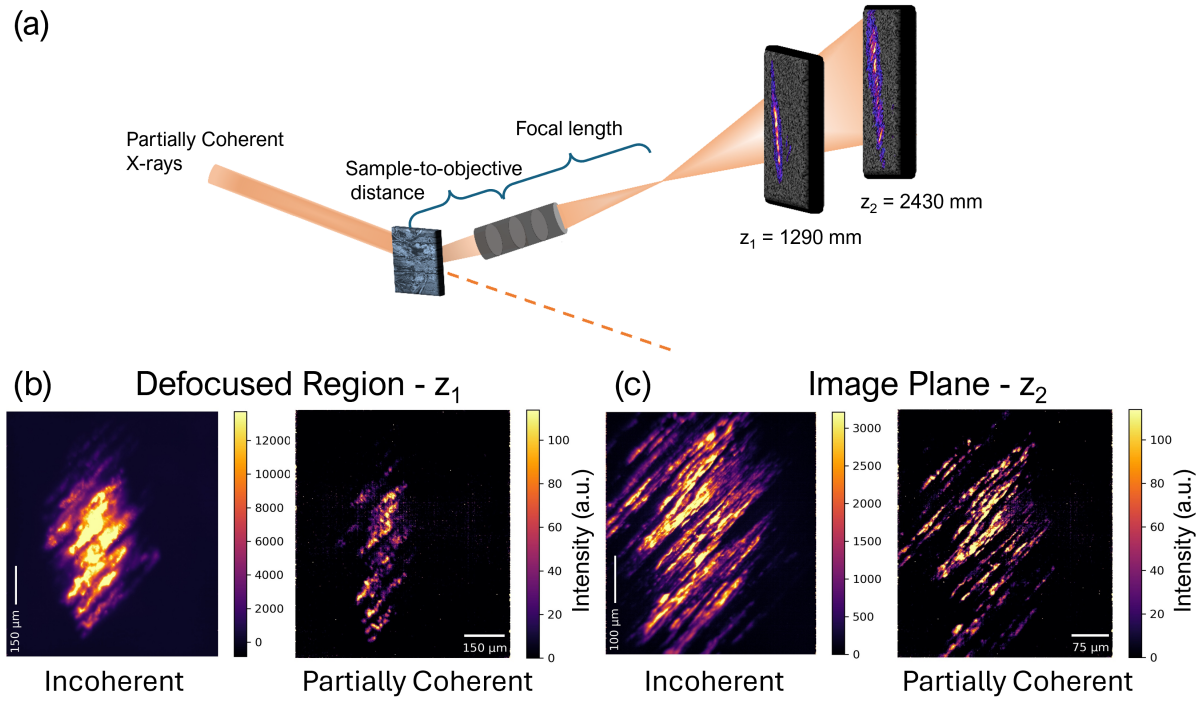

Figure 6.1: (a) Schematic of Dark-Field X-ray Microscopy (DFXM) imaging through the defocused region between the back-focal and image planes, with the relative sample-to-detector distances of the two regions denoted as z. DFXM images of $NaMnO_2$ collected in the defocused region (b) and at the image plane (c) using incoherent (left) and partially coherent (right) X-rays are also presented for comparison. The use of partially coherent light increases feature contrast in both the focused and defocused images.

region with partially coherent X-rays are displayed in Figure 6.1. The increased coherence of the incident light demonstrates a general contrast enhancement of $NaMnO_2$'s linear domain structures, while positioning the detector in the defocused region further enhances the contrast of phase-dependent domain features, which lie along the transverse direction. Furthermore, the use of a highly coherent light source could theoretically be used to retrieve phase information from the collected images, enabling increased resolution and restoration of depth resolution to the technique, but many challenges still remain for this active field of research.

As a full-field imaging technique, DFXM generates high-dimensional datasets, espe-

cially when performed in-situ, that quickly become large and computational expensive to store and process. Employing machine learning techniques and algorithms to optimize both data collection and post-processing will be crucial for achieving high-throughput DFXM measurements. Computer vision techniques, such as feature identification, object tracking [73], and image registration [50], are increasingly being applied to these datasets. However, because DFXM images reveal contrast from both real-space and reciprocal-space variations, traditional computer vision networks trained on real-space objects may not sufficiently analyze DFXM images. Therefore, complementary techniques like X-ray CT and far-field HEDM are essential for improving defect identification and material characterization. By tagging the vast amounts of image data generated, these datasets can be better utilized as training datasets for machine learning algorithms and analysis.

Looking forward, the continued development of DFXM holds great potential for advancing the understanding of complex materials and their structural dynamics. The integration of complementary techniques, such as HEDM, ARPES and machine learning algorithms, will enable deeper insights into electronic states and defect structures. Enhancements to depth resolution through advanced imaging methods and the utilization of coherent X-rays, as made possible by recent synchrotron upgrades, will further push the boundaries of what DFXM can resolve. As these innovations unfold, DFXM stands poised to play a critical role in future research, driving both technical advancements and new discoveries across a range of materials science challenges.

Bibliography

[1] Artem M. Abakumov, Alexander A. Tsirlin, Ioanna Bakaimi, Gustaaf Van Tendeloo, and Alexandros Lappas. Multiple twinning as a structure directing mechanism in layered rock-salt-type oxides: $NaMnO_2$ polymorphism, redox potentials, and magnetism. *Chemistry of Materials*, 26(10):3306–3315, 2014. URL `https://pubs.acs.org/doi/full/10.1021/cm5011696`.

[2] Rebecca L. Dally, Robin Chisnell, Leland Harriger, Yaohua Liu, Jeffrey W. Lynn, and Stephen D. Wilson. Thermal evolution of quasi-one-dimensional spin correlations within the anisotropic triangular lattice of $\alpha - \mathrm{namno}_2$. *Physical Review B*, 98(14):144444, 2018. doi: 10.1103/PhysRevB.98.144444. URL `https://link.aps.org/doi/10.1103/PhysRevB.98.144444`.

[3] Leon Balents. Spin liquids in frustrated magnets. *nature*, 464(7286):199–208, 2010. URL `https://www.nature.com/articles/nature08917`.

[4] O. Prokhnenko, R. Feyerherm, M. Mostovoy, N. Aliouane, E. Dudzik, A. U. B. Wolter, A. Maljuk, and D. N. Argyriou. Coupling of frustrated ising spins to the magnetic cycloid in multiferroic tbmno_3. *Phys. Rev. Lett.*, 99:177206, Oct 2007. doi: 10.1103/PhysRevLett.99.177206. URL `https://link.aps.org/doi/10.1103/PhysRevLett.99.177206`.

[5] J. T. Haraldsen, M. Swanson, G. Alvarez, and R. S. Fishman. Spin-wave instabilities and noncollinear magnetic phases of a geometrically frustrated triangular-lattice antiferromagnet. *Phys. Rev. Lett.*, 102:237204, June 2009. doi: 10.1103/PhysRevLett.102.237204. URL `https://link.aps.org/doi/10.1103/PhysRevLett.102.237204`.

[6] Raphaële J Clément, Derek S Middlemiss, Ieuan D Seymour, Andrew J Ilott, and Clare P Grey. Insights into the nature and evolution upon electrochemical cycling of planar defects in the β-$NaMnO_2$ Na-ion battery cathode: An NMR and first-principles density functional theory approach. *Chemistry of Materials*, 28(22):8228–8239, 2016.

[7] Andrej Zorko, Samir El Shawish, Denis Arčon, Zvonko Jagličić, Alexandros Lappas, Hans van Tol, and Louis Claude Brunel. Magnetic interactions in α-$NaMnO_2$:

Quantum spin-2 system on a spatially anisotropic two-dimensional triangular lattice. *Physical Review B—Condensed Matter and Materials Physics*, 77(2):024412, 2008.

[8] Christopher Stock, Laurent C. Chapon, O. Adamopoulos, A. Lappas, M. Giot, J. W. Taylor, M. A. Green, F. C. Brown, and P. G. Radaelli. One-dimensional magnetic fluctuations in the spin-2 triangular lattice α-$NaMnO_2$. *Physical review letters*, 103 (7):077202, 2009.

[9] Maud Giot, Laurent C. Chapon, John Androulakis, Mark A. Green, Paolo G. Radaelli, and Alexandros Lappas. Magnetoelastic coupling and symmetry breaking in the frustrated antiferromagnet $\alpha - \mathrm{namno}_2$. *Physical review letters*, 99(24): 247211, 2007.

[10] Ting Jia, Guoren Zhang, Xiaoli Zhang, Ying Guo, Zhi Zeng, and H. Q. Lin. Magnetic frustration in $\alpha - \mathrm{namno}_2$ and $CuMnO_2$. *Journal of Applied Physics*, 109(7), 2011.

[11] Rebecca Dally, Raphaële J Clément, Robin Chisnell, Stephanie Taylor, Megan Butala, Vicky Doan-Nguyen, Mahalingam Balasubramanian, Jeffrey W. Lynn, Clare P. Grey, and Stephen D. Wilson. Floating zone growth of α-na0. 90mno2 single crystals. *Journal of Crystal Growth*, 459:203–208, 2017.

[12] Rebecca L. Dally, Alvin J. R. Heng, Anna Keselman, Mitchell M. Bordelon, Matthew B. Stone, Leon Balents, and Stephen D. Wilson. Three-magnon bound state in the quasi-one-dimensional antiferromagnet α-namno_2. *Physical Review Letters*, 124(19):197203, 2020.

[13] Andrej Zorko, Othon Adamopoulos, Matej Komelj, D. Arčon, and Alexandros Lappas. Frustration-induced nanometre-scale inhomogeneity in a triangular antiferromagnet. *Nature Communications*, 5(1):3222, 2014.

[14] Xiaohua Ma, Hailong Chen, and Gerbrand Ceder. Electrochemical properties of monoclinic $NaMnO_2$. *Journal of The Electrochemical Society*, 158(12):A1307, 2011.

[15] Juliette Billaud, Raphaële J Clément, A Robert Armstrong, Jesús Canales-Vázquez, Patrick Rozier, Clare P Grey, and Peter G Bruce. β-$NaMnO_2$: a high-performance cathode for sodium-ion batteries. *Journal of the American Chemical Society*, 136 (49):17243–17248, 2014.

[16] Cheng Chen, Zhen Han, Chaoping Liang, Yiming Feng, Peng Wang, and Weifeng Wei. Electrochemically induced cleavage cracking at twin boundary of sodium layered oxide cathodes. *Acta Materialia*, 238:118212, 2022.

[17] Gui-Liang Xu, Xiang Liu, Xinwei Zhou, Chen Zhao, Inhui Hwang, Amine Daali, Zhenzhen Yang, Yang Ren, Cheng-Jun Sun, Zonghai Chen, Yuzi Lio, and Khalil

Amine. Native lattice strain induced structural earthquake in sodium layered oxide cathodes. *Nature Communications*, 13(1):436, 2022. URL https://doi.org/10.1038/s41467-022-28052-x.

[18] Brenden R. Ortiz, Lídia C. Gomes, Jennifer R. Morey, Michal Winiarski, Mitchell Bordelon, John S. Mangum, Iain W. H. Oswald, Jose A. Rodriguez-Rivera, James R. Neilson, Stephen D. Wilson, Elif Ertekin, Tyrel M. McQueen, and Eric S. Toberer. New kagome prototype materials: discovery of kv_3sb_5, rbv_3sb_5, and csv_3sb_5. *Phys. Rev. Mater.*, 3:094407, Sep 2019. doi: 10.1103/PhysRevMaterials.3.094407. URL https://link.aps.org/doi/10.1103/PhysRevMaterials.3.094407.

[19] Shuo-Ying Yang, Yaojia Wang, Brenden R. Ortiz, Defa Liu, Jacob Gayles, Elena Derunova, Rafael Gonzalez-Hernandez, Libor Šmejkal, Yulin Chen, Stuart S. P. Parkin, Stephen D. Wilson, Eric S. Toberer, Tyrel McQueen, and Mazhar N. Ali. Giant, unconventional anomalous hall effect in the metallic frustrated magnet candidate, KV_3Sb_5. *Science advances*, 6(31):eabb6003, 2020. URL https://www.science.org/doi/abs/10.1126/sciadv.abb6003.

[20] F. H. Yu, T. Wu, Z. Y. Wang, B. Lei, W. Z. Zhuo, J. J. Ying, and X. H. Chen. Concurrence of anomalous hall effect and charge density wave in a superconducting topological kagome metal. *Physical Review B*, 104(4):L041103, 2021.

[21] He Zhao, Hong Li, Brenden R. Ortiz, Samuel M. L. Teicher, Takamori Park, Mengxing Ye, Ziqiang Wang, Leon Balents, Stephen D. Wilson, and Ilija Zeljkovic. Cascade of correlated electron states in the kagome superconductor CsV_3Sb_5. *Nature*, 599(7884):216–221, 2021. doi: 10.1038/s41586-021-03946-w. URL https://www.nature.com/articles/s41586-021-03946-w.

[22] Hong Li, He Zhao, Brenden R Ortiz, Yuzki Oey, Ziqiang Wang, Stephen D Wilson, and Ilija Zeljkovic. Unidirectional coherent quasiparticles in the high-temperature rotational symmetry broken phase of AV_3Sb_5 kagome superconductors. *Nature Physics*, 19(5):637–643, 2023. doi: 10.1038/s41567-022-01932-1. URL https://www.nature.com/articles/s41567-022-01932-1.

[23] J. Luo, Z. Zhao, Y. Z. Zhou, J. Yang, A. F. Fang, H. T. Yang, H. J. Gao, R. Zhou, and Guo-qing Zheng. Possible star-of-david pattern charge density wave with additional modulation in the kagome superconductor CsV_3Sb_5. *npj Quantum Materials*, 7 (1):30, 2022. doi: 10.1038/s41535-022-00437-7. URL https://www.nature.com/articles/s41535-022-00437-7.

[24] Stephen D. Wilson and Brenden R. Ortiz. AV_3Sb_5 kagome superconductors. *Nature Reviews Materials*, 9(6):420–432, Jun 2024. ISSN 2058-8437. doi: 10.1038/s41578-024-00677-y. URL https://doi.org/10.1038/s41578-024-00677-y.

[25] Yu-Xiao Jiang, Jia-Xin Yin, M. Michael Denner, Nana Shumiya, Brenden R. Ortiz, Gang Xu, Zurab Guguchia, Junyi He, Md Shafayat Hossain, Xiaoxiong Liu, Jacob Ruff, Linus Kautzsch, Songtian S. Zhang, Guoqing Chang, Ilya Belopolski, Qi Zhang, Tyler A. Cochran, Daniel Multer, Maksim Litskevich, Zi-Jia Cheng, Xian P. Yang, Ziqiang Wang, Ronny Thomale, Titus Neupert, Stephen D. Wilson, and M. Zahid Hasan. Unconventional chiral charge order in kagome superconductor KV_3Sb_5. *Nature materials*, 20(10):1353–1357, 2021. doi: 10.1038/s41563-021-01034-y. URL https://www.nature.com/articles/s41563-021-01034-y.

[26] C. Mielke, D. Das, J.-X. Yin, H. Liu, R. Gupta, Y.-X. Jiang, M. Medarde, X. Wu, H. C. Lei, J. Chang, Pengcheng Dai, Q. Si, H. Miao, R. Thomale, T. Neupert, Y. Shi, R. Khasanov, M. Z. Hasan, H. Luetkens, and Z. Guguchia. Time-reversal symmetry-breaking charge order in a kagome superconductor. *Nature*, 602(7896): 245–250, 2022. doi: 10.1038/s41586-021-04327-z. URL https://www.nature.com/articles/s41586-021-04327-z.

[27] Yuqing Xing, Seokjin Bae, Ethan Ritz, Fan Yang, Turan Birol, Andrea N. Capa Salinas, Brenden R. Ortiz, Stephen D. Wilson, Ziqiang Wang, Rafael M. Fernandes, and Vidya Madhavan. Optical manipulation of the charge-density-wave state in RbV_3Sb_5. *Nature*, pages 1–7, 2024. doi: 10.1038/s41586-024-07519-5. URL https://www.nature.com/articles/s41586-024-07519-5.

[28] Tian Le, Zhiming Pan, Zhuokai Xu, Jinjin Liu, Jialu Wang, Zhefeng Lou, Xiaohui Yang, Zhiwei Wang, Yugui Yao, Congjun Wu, and Xiao Lin. Superconducting diode effect and interference patterns in kagome CsV_3Sb_5. *Nature*, pages 1–6, 2024. doi: 10.1038/s41586-024-07431-y. URL https://www.nature.com/articles/s41586-024-07431-y.

[29] Yishuai Xu, Zhuoliang Ni, Yizhou Liu, Brenden R. Ortiz, Qinwen Deng, Stephen D. Wilson, Binghai Yan, Leon Balents, and Liang Wu. Three-state nematicity and magneto-optical kerr effect in the charge density waves in kagome superconductors. *Nature physics*, 18(12):1470–1475, 2022.

[30] Brenden R. Ortiz, Samuel M. L. Teicher, Yong Hu, Julia L. Zuo, Paul M. Sarte, Emily C. Schueller, A. M. Milinda Abeykoon, Matthew J. Krogstad, Stephan Rosenkranz, Raymond Osborn, Ram Seshadri, Leon Balents, Junfeng He, and Stephen D. Wilson. CsV_3Sb_5: A Z_2 topological kagome metal with a superconducting ground state. *Phys. Rev. Lett.*, 125:247002, Dec 2020. doi: 10.1103/PhysRevLett.125.247002. URL https://link.aps.org/doi/10.1103/PhysRevLett.125.247002.

[31] Brenden R. Ortiz, Paul M. Sarte, Eric M. Kenney, Michael J. Graf, Samuel M. L. Teicher, Ram Seshadri, and Stephen D. Wilson. Superconductivity in the Z_2 kagome metal KV_3Sb_5. *Physical Review Materials*, 5(3):034801, 2021. doi: 10.1103/

PhysRevMaterials.5.034801. URL https://doi/10.1103/PhysRevMaterials.5.034801.

[32] Qiangwei Yin, Zhijun Tu, Chunsheng Gong, Yang Fu, Shaohua Yan, and Hechang Lei. Superconductivity and normal-state properties of kagome metal RbV_3Sb_5 single crystals. *Chinese Physics Letters*, 38(3):037403, 2021. doi: 10.1088/0256-307X/38/3/037403. URL https://doi.org/10.1088/0256-307X/38/3/037403.

[33] Jonathan Frassineti, Pietro Bonfà, Giuseppe Allodi, Erick Garcia, Rong Cong, Brenden R. Ortiz, Stephen D. Wilson, Roberto De Renzi, Vesna F. Mitrović, and Samuele Sanna. Microscopic nature of the charge-density wave in the kagome superconductor RbV_3Sb_5. *Physical Review Research*, 5(1):L012017, 2023.

[34] Linus Kautzsch, Brenden R. Ortiz, Krishnanand Mallayya, Jayden Plumb, Ganesh Pokharel, Jacob P. C. Ruff, Zahirul Islam, Eun-Ah Kim, Ram Seshadri, and Stephen D. Wilson. Structural evolution of the kagome superconductors AV_3Sb_5 (A = K, Rb, and Cs) through charge density wave order. *Phys. Rev. Mater.*, 7:024806, Feb 2023. doi: 10.1103/PhysRevMaterials.7.024806. URL https://link.aps.org/doi/10.1103/PhysRevMaterials.7.024806.

[35] Mingu Kang, Shiang Fang, Jonggyu Yoo, Brenden R. Ortiz, Yuzki M. Oey, Jonghyeok Choi, Sae Hee Ryu, Jimin Kim, Chris Jozwiak, Aaron Bostwick, Eli Rotenberg, Efthimios Kaxiras, Joseph G. Checkelsky, Stephen D. Wilson, Jae-Hoon Park, and Riccardo Comin. Charge order landscape and competition with superconductivity in kagome metals. *Nature Materials*, 22(2):186–193, 2023. doi: 10.1038/s41563-022-01375-2. URL https://www.nature.com/articles/s41563-022-01375-2.

[36] Yong Hu, Xianxin Wu, Brenden R Ortiz, Xinloong Han, Nicholas C Plumb, Stephen D Wilson, Andreas P Schnyder, and Ming Shi. Coexistence of trihexagonal and star-of-david pattern in the charge density wave of the kagome superconductor AV_3Sb_5. *Physical Review B*, 106(24):L241106, 2022. doi: 10.1103/PhysRevB.106.L241106. URL https://doi/10.1103/PhysRevB.106.L241106.

[37] Haoxiang Li, T. T. Zhang, T. Yilmaz, Y. Y. Pai, C. E. Marvinney, A. Said, Q. W. Yin, C. S. Gong, Z. J. Tu, E. Vescovo, C. S. Nelson, R. G. Moore, S. Murakami, H. C. Lei, H. N. Lee, B. J. Lawrie, and H. Miao. Observation of unconventional charge density wave without acoustic phonon anomaly in kagome superconductors AV_3Sb_5 (A=Rb, Cs). *Phys. Rev. X*, 11:031050, Sep 2021. doi: 10.1103/PhysRevX.11.031050. URL https://link.aps.org/doi/10.1103/PhysRevX.11.031050.

[38] Brenden R. Ortiz, Samuel M. L. Teicher, Linus Kautzsch, Paul M. Sarte, Noah Ratcliff, John Harter, Jacob P. C. Ruff, Ram Seshadri, and Stephen D. Wilson. Fermi surface mapping and the nature of charge-density-wave order in the kagome superconductor CsV_3Sb_5. *Physical Review X*, 11(4):041030, 2021.

[39] Q. Stahl, D. Chen, T. Ritschel, C. Shekhar, E. Sadrollahi, M. C. Rahn, O. Ivashko, M. V. Zimmermann, C. Felser, and J. Geck. Temperature-driven reorganization of electronic order in CsV_3Sb_5. *Physical Review B*, 105(19):195136, 2022.

[40] Qian Xiao, Yihao Lin, Qizhi Li, Xiquan Zheng, Sonia Francoual, Christian Plueckthun, Wei Xia, Qingzheng Qiu, Shilong Zhang, and Yanfeng Guo. Coexistence of multiple stacking charge density waves in kagome superconductor CsV_3Sb_5. *Physical Review Research*, 5(1):L012032, 2023.

[41] Shangfei Wu, Brenden R Ortiz, Hengxin Tan, Stephen D Wilson, Binghai Yan, Turan Birol, and Girsh Blumberg. Charge density wave order in the kagome metal AV_3Sb_5 ($A = Cs, Rb, K$). *Physical Review B*, 105(15):155106, 2022. doi: 10.1103/PhysRevB.105.155106. URL `https://doi/10.1103/PhysRevB.105.155106`.

[42] Hong Li, He Zhao, Brenden R Ortiz, Takamori Park, Mengxing Ye, Leon Balents, Ziqiang Wang, Stephen D Wilson, and Ilija Zeljkovic. Rotation symmetry breaking in the normal state of a kagome superconductor KV_3Sb_5. *Nature Physics*, 18(3): 265–270, 2022.

[43] Jayden Plumb, Ishwor Poudyal, Rebecca L. Dally, Samantha Daly, Stephen D. Wilson, and Zahir Islam. Dark field x-ray microscopy below liquid-helium temperature: The case of $NaMnO_2$. *Materials Characterization*, 204:113174, 2023. URL `https://www.sciencedirect.com/science/article/pii/S1044580323005338`.

[44] Jayden Plumb, Andrea Capa Salinas, Krishnanand Mallayya, Elliot Kisiel, Fellipe B. Carneiro, Reina Gomez, Ganesh Pokharel, Eun-Ah Kim, Suchismita Sarker, Zahirul Islam, Sam Daly, and Stephen D. Wilson. Phase-separated charge order and twinning across length scales in CsV_3Sb_5. *Phys. Rev. Mater.*, 8:093601, Sep 2024. doi: 10.1103/PhysRevMaterials.8.093601. URL `https://link.aps.org/doi/10.1103/PhysRevMaterials.8.093601`.

[45] Hugh Simons, A. King, Wolfgang Ludwig, C. Detlefs, Wolfgang Pantleon, Søren Schmidt, F. Stöhr, I. Snigireva, A. Snigirev, and Henning Friis Poulsen. Dark-field x-ray microscopy for multiscale structural characterization. *Nature communications*, 6(1):6098, 2015.

[46] Deming Shu, Zahirul Islam, Jayson Anton, Steven Kearney, Xianbo Shi, Walan Grizolli, Peter Kenesei, Sarvjit Shastri, and Lahsen Assoufid. Mechanical design of a new precision alignment apparatus for compact x-ray compound refractive lens manipulator. In *Proceedings of the MEDSI 2018 Conference*, pages 168–172, 2018.

[47] Hugh Simons, Anders Clemen Jakobsen, Sonja Rosenlund Ahl, Carsten Detlefs, and Henning Friis Poulsen. Multiscale 3D characterization with dark-field x-ray microscopy. *Mrs Bulletin*, 41(6):454–459, 2016.

[48] Can Yildirim, Phil Cook, Carsten Detlefs, Hugh Simons, and Henning Friis Poulsen. Probing nanoscale structure and strain by dark-field x-ray microscopy. *MRS Bulletin*, 45(4):277–282, 2020.

[49] Lord Rayleigh. Xxv. on copying diffraction-gratings, and on some phenomena connected therewith. *The London, Edinburgh, and Dublin Philosophical Magazine and Journal of Science*, 11(67):196–205, 1881. doi: 10.1080/14786448108626995. URL `https://doi.org/10.1080/14786448108626995`.

[50] Zhi Qiao, Xianbo Shi, Peter Kenesei, Arndt Last, Lahsen Assoufid, and Zahir Islam. A large field-of-view high-resolution hard x-ray microscope using polymer optics. *Review of Scientific Instruments*, 91(11), 2020.

[51] Xianbo Shi, Walan Grizolli, Deming Shu, Luca Rebuffi, Zahirul Islam, and Lahsen Assoufid. High-speed characterization of refractive lenses with single-grating interferometry. In *Advances in Metrology for X-Ray and EUV Optics VIII*, volume 11109, pages 128–135. SPIE, 2019.

[52] Elliot Kisiel, Ishwor Poudyal, Peter Kenesei, Mark Engbretson, Arndt Last, Rourav Basak, Ivan Zaluzhnyy, Uday Goteti, Robert Dynes, Antonino Miceli, Alex Frano, and Zahir Islam. Direct detection system for full-field nanoscale x-ray diffraction-contrast imaging. *Opt. Express*, 32(16):27682–27689, Jul 2024. doi: 10.1364/OE.518974. URL `https://opg.optica.org/oe/abstract.cfm?URI=oe-32-16-27682`.

[53] Ishwor Poudyal, Zhi Qiao, Arndt Last, Michael R. Armstrong, and Zahir Islam. Pump-probe dark-field x-ray microscopy, 2022. URL `https://arxiv.org/abs/2210.06243`.

[54] Júlia Garriga Ferrer, Raquel Rodríguez-Lamas, Henri Payno, Wout De Nolf, Phil Cook, Vicente Armando Solé Jover, Can Yildirim, and Carsten Detlefs. darfix–data analysis for dark-field x-ray microscopy. *Journal of Synchrotron Radiation*, 30(3), 2023.

[55] Sonja Rosenlund Ahl. *Elements of a Method for Multiscale Characterization of Recrystallization in Deformed Metals*. PhD thesis, Department of Physics, Technical University of Denmark, 2018.

[56] A. C. Jakobsen, H. Simons, W. Ludwig, C. Yildirim, H. Leemreize, L. Porz, C. Detlefs, and H. F. Poulsen. Mapping of individual dislocations with dark-field x-ray microscopy. *Journal of Applied Crystallography*, 52(1):122–132, 2019.

[57] Leora E. Dresselhaus-Marais, Grethe Winther, Marylesa Howard, Arnulfo Gonzalez, Sean R. Breckling, Can Yildirim, Philip K. Cook, Mustafacan Kutsal, Hugh Simons, Carsten Detlefs, Jon H. Eggert, and Henning Friis Poulsen. In situ visualization of long-range defect interactions at the edge of melting. *Science Advances*, 7

(29):eabe8311, 2021. URL https://www.science.org/doi/abs/10.1126/sciadv.abe8311.

[58] Hugh Simons, Anders Clemen Jakobsen, Sonja Rosenlund Ahl, Henning Friis Poulsen, Wolfgang Pantleon, Ying-Hao Chu, Carsten Detlefs, and Nagarajan Valanoor. Nondestructive mapping of long-range dislocation strain fields in an epitaxial complex metal oxide. *Nano letters*, 19(3):1445–1450, 2019.

[59] Ashley Bucsek, Hanuš Seiner, Hugh Simons, Can Yildirim, Phil Cook, Yuriy Chumlyakov, Carsten Detlefs, and Aaron P. Stebner. Sub-surface measurements of the austenite microstructure in response to martensitic phase transformation. *Acta Materialia*, 179:273–286, 2019.

[60] J. van Landuyt, G. van Tendeloo, and S. Amelinckx. The direct imaging of two-dimensional charge density waves and of commensurate superlattices in $NbTe_2$ and $TaTe_2$. *physica status solidi (a)*, 29(1):K11–K13, 1975. doi: https://doi.org/10.1002/pssa.2210290143. URL https://onlinelibrary.wiley.com/doi/abs/10.1002/pssa.2210290143.

[61] Stephan Preibisch, Stephan Saalfeld, and Pavel Tomancak. Globally optimal stitching of tiled 3D microscopic image acquisitions. *Bioinformatics*, 25(11):1463–1465, 2009.

[62] Johannes Schindelin, Ignacio Arganda-Carreras, Erwin Frise, Verena Kaynig, Mark Longair, Tobias Pietzsch, Stephan Preibisch, Curtis Rueden, Stephan Saalfeld, Benjamin Schmid, Jean-Yves Tinevez, Daniel James White, Volker Hartenstein, Kevin Eliceiri, Pavel Tomancak, and Albert Cardona. Fiji: an open-source platform for biological-image analysis. *Nature methods*, 9(7):676–682, 2012. URL https://www.nature.com/articles/nmeth.2019.

[63] Alexander Opolka, Dominik Müller, Christian Fella, Andreas Balles, Jürgen Mohr, and Arndt Last. Multi-lens array full-field x-ray microscopy. *Applied Sciences*, 11 (16):7234, 2021.

[64] B. Boucher, R. Buhl, and M. Perrin. Magnetic structure of Mn_3O_4 by neutron diffraction. *Journal of Applied Physics*, 42(4):1615–1617, 1971.

[65] Taeyang Choi, Zhan Zhang, Hoon Kim, Sunwook Park, Jong-Woo Kim, Kyeong Jun Lee, Zahir Islam, Ulrich Welp, Seo Hyoung Chang, and B. J. Kim. Nanoscale antiferromagnetic domain imaging using full-field resonant x-ray magnetic diffraction microscopy. *Advanced Materials*, 34(29):2200639, 2022. doi: https://doi.org/10.1002/adma.202200639. URL https://onlinelibrary.wiley.com/doi/abs/10.1002/adma.202200639.

[66] S. D. Shastri, K. Fezzaa, A. Mashayekhi, W.-K. Lee, P. B. Fernandez, and P. L. Lee. Cryogenically cooled bent double-laue monochromator for high-energy undulator x-rays (50–200 keV). *Journal of synchrotron radiation*, 9(5):317–322, 2002.

[67] A. Khounsary, P. Kenesei, J. Collins, G. Navrotski, and J. Nudell. High energy x-ray micro-tomography for the characterization of thermally fatigued glidcop specimen. *Journal of Physics: Conference Series*, 425(21):212015, mar 2013. doi: 10.1088/1742-6596/425/21/212015. URL https://dx.doi.org/10.1088/1742-6596/425/21/212015.

[68] Betsy A. Dowd, Graham H. Campbell, Robert B. Marr, Vivek V. Nagarkar, Sameer V. Tipnis, Lisa Axe, and D. Peter Siddons. Developments in synchrotron x-ray computed microtomography at the National Synchrotron Light Source. In Ulrich Bonse, editor, *Developments in X-Ray Tomography II*, volume 3772, pages 224 – 236. International Society for Optics and Photonics, SPIE, 1999. doi: 10.1117/12.363725. URL https://doi.org/10.1117/12.363725.

[69] National Institute of Standards and Technology. Nist standard reference database 126: X-ray mass attenuation coefficients. https://www.nist.gov/pml/x-ray-mass-attenuation-coefficients, 2004. Accessed: 2024-08-16.

[70] H. D. Flack. *International Tables for Crystallography*, volume A. International Union of Crystallography, 2016.

[71] Doğa Gürsoy, Kaan Alp Yay, Elliot Kisiel, Michael Wojcik, Dina Sheyfer, Matthew Highland, Ian Randal Fisher, Stephan Hruszkewycz, and Zahir Islam. Dark-field x-ray microscopy with structured illumination for three-dimensional imaging, 2024. URL https://arxiv.org/abs/2405.12799.

[72] Pavel Salev, Elliot Kisiel, Dayne Sasaki, Brandon Gunn, Wei He, Mingzhen Feng, Junjie Li, Nobumichi Tamura, Ishwor Poudyal, Zahirul Islam, Yayoi Takamura, Alex Frano, and Ivan K. Schuller. Local strain inhomogeneities during electrical triggering of a metal–insulator transition revealed by x-ray microscopy. *Proceedings of the National Academy of Sciences*, 121(34):e2317944121, 2024. doi: 10.1073/pnas.2317944121. URL https://www.pnas.org/doi/abs/10.1073/pnas.2317944121.

[73] Omar Abulshohoud, Ishwor Poudyal, Jessica McChesney, Zhan Zhang, Zhi Qiao, Ulrich Welp, and Zahir Islam. A general method for multiresolutional analysis of mesoscale features in dark-field x-ray microscopy images, 2022. URL https://arxiv.org/abs/2210.15757.